Imperial College London

Department of Electrical and Electronic Engineering

Light trapping structures for photovoltaics using silicon nanowires and silicon micro-pyramids

Tasmiat Rahman

July 2015

Supervised by Dr Kristel Fobelets

Submitted in part fulfilment of the requirements for the degree of

Doctor of Philosophy in Electrical and Electronic Engineering of Imperial College London

and the Diploma of Imperial College London

Declaration

I herewith certify that all material in this dissertation which is not my own work has been properly acknowledged.

Tasmiat Rahman

Copyright Declaration

The copyright of this thesis rests with the author and is made available under a Creative Commons Attribution Non-Commercial No Derivatives licence. Researchers are free to copy, distribute or transmit the thesis on the condition that they attribute it, that they do not use it for commercial purposes and that they do not alter, transform or build upon it. For any reuse or redistribution, researchers must make clear to others the licence terms of this work

Publications

Journal

1. Rahman T., Navarro-Cía M., Fobelets K. (2014). "High density micro-pyramids with silicon nanowire array for photovoltaic applications". Nanotechnology, 25(48), 485202.

2. Rahman T., Fobelets K. (2015). "Efficient tool flow for 3D Photovoltaic modelling". Computer Physics Communications, Volume 193, August 2015, Pages 124-130, ISSN 0010-4655

Conference

1. Rahman T., Navarro-Cía M., Fobelets K. "Fabrication of micro-nano hybrid surfaces for anti-reflective layer in photovoltaic applications", 40th Int. Conf. on Micro and Nano Engineering, 22-26 Sept. Lausanne, Switzerland (2014).

2. Khouri W., Xu B., Ahmad M.M., Rahman T., Fobelets K. "Thermoelectric properties of stooks of Si nanowire arrays", 40th Int. Conf. on Micro and Nano Engineering, 22-26 Sept. Lausanne, Switzerland (2014)

3. Rahman T., Fobelets K. "Simulation of rough silicon nanowire array for use in spin-on-doped PN core shell solar cells", 7th Eur. Modelling Symp., EMS2013, Manchester, 20 - 22 November (2013)

4. Khas M., Rahman T., Xu B., Fobelets K. "Impedance spectroscopy of Si nanowire/-conjugated polymer compounds", 39th Int. Conf. on Micro and Nano Engineering, 16-19 Sept. London, UK (2013).

5. Rahman T., Fobelets K. “3D TCAD Optimization of Spin-On-Doped PN Core-Shell Silicon Nanowire Arrays for use in Solar cells”, 39th Int. Conf. on Micro and Nano Engineering, 16-19 Sept. London, UK (2013).

6. Shougee A., Rahman T., Xu B., Fobelets K. “Optimization strategies for thermoelectric power from Si nanowire arrays”, 39th Int. Conf. on Micro and Nano Engineering, 16-19 Sept. London, UK (2013).

7. Rahman T., Fobelets K., Meziani Y., Velazquez-Perez J.E. “Highly doped nanowire array for use in hybrid silicon/polymer junction solar cell”, 223rd ECS Meet., Toronto, Canada, May 12-16 (2013)

Abstract

The current photovoltaic industry is dominated by crystalline or poly-crystalline Si in a planar pn-junction configuration. The use of silicon nanowire arrays (SiNWA) within this industry has shown great promise due to its application as an anti-reflective layer, as well as benefits in charge carrier extraction. In this work, we use a metal assisted chemical etch process to fabricate SiNWAs onto a dense periodic array of pyramids that are formed using an alkaline etch masked with an oxide layer. The hybrid micro-nano structure acts as an anti-reflective coating with experimental reflectivity below 1% over the visible and near-infrared spectral regions. This represents an improvement of up to 11 and 14 times compared to the pyramid array and SiNWAs on bulk, respectively. In addition to the experimental work, we optically simulate the hybrid structure using the commercial Lumerical FDTD package. The results of the optical simulations support our experimental work, illustrating a reduced reflectivity in the hybrid structure. The nanowire array increases the absorbed carrier density within the pyramid by providing a guided transition of the refractive index along the light path from air into the silicon. Furthermore, electrical simulations which take into account surface and Auger recombination show an efficiency increase for the hybrid structure of 56% over bulk, 11% over pyramid array and 8.5% over SiNWAs. Opto-electronic modelling was performed by establishing a tool flow to integrate the effective optical simulator Lumerical FDTD with the excellent fabrication and electrical simulation capability of Sentaurus TCAD. Interfacing between the two packages is achieved through tool command language and Matlab, offering fast and accurate electro-optical characteristics of nano-structured PV devices.

Acknowledgements

I would like to thank my supervisor Dr Kristel Fobelets for her continued guidance and support throughout my PhD. Her encouragement to experiment new ideas and confidence in my ability, helped me remain motivated throughout. Her supervision made my PhD a thoroughly enjoyable experience for which I am forever grateful. I would like to thank Dr. Munir Ahmad, Dr Chuanbo Li, and Dr Miguel Navarro-Cia. They have all played an invaluable part in guiding various aspects of the research project, and were extremely patient teachers from whom I have learned a lot. I would also like to thank Professor Enrique Velazquez-Perez for the opportunity to visit his labs at the University of Salamanca several times during my PhD - an experience I enjoyed greatly. I would like to thank all my colleagues in OSD for providing me with great memories and much needed coffee breaks. Special thanks goes to Edd, Tzern, Kaushal, Evi, Aifric, Chen, Emi, Mario, Manuel, Pit, Bob, Peter, Alexey, and Fangjing. Thanks to Hadri for all the splinter breaks, karaoke, and fun evenings away from the PhD. Thanks also to John for his friendship, guidance and motivation not only through this PhD but through 8 years of EEE. Thanks to Evan for many great memories in Singapore and Malaysia, and his continued friendship. Thanks also to all the wardens and seniors in both Garden & Weeks and Wilkinson & Weeks. In particular, thanks to Joao for giving me my first opportunity to sub-warden in a halls of residence. The experiences I gained through this role was a pleasant distraction from the stresses of my PhD. I would like to especially thank Krystallo for her support, guidance and motivation throughout my PhD. Her encouragement, patience and belief in me helped complete my PhD successfully. Finally, I would like to thank my family for all their support. I am incredibly grateful for the love, guidance and encouragement from my Dad, Mum and Brother. They are my inspiration and I dedicate this work to them.

Contents

Acknowledgements **7**

List of Figures **11**

List of Tables **23**

1 Introduction **25**

1.1 Motivation for Photovoltaic research 25

1.2 Fundamentals of Solar Cells 28

1.2.1 Sunlight 28

1.2.2 Device 30

1.2.3 Theoretical limit 37

1.3 Key role: Light trapping 37

1.3.1 Anti-reflective coatings 38

1.3.2 Surface Texturing 40

1.3.3 Surpassing the Ray Optics Limit 42

1.4 Nanowire Technologies 48

1.5 Aims and Organisation of Thesis 54

1.5.1 Project Aims 54

1.5.2 Organisation of Thesis 55

2 TCAD **57**

2.1 SProcess 57

2.1.1 Diffuse 58

2.1.2 Deposit 59

2.1.3 Etch 62
2.1.4 Mesh Generation 62
2.2 SDevice 64
2.2.1 Basic Equations 67
2.2.2 Traps 68
2.3 Simulation of SiNWA 69
2.3.1 Process Simulation 69
2.3.2 Electrical Simulation 70
2.3.3 Conclusion 73

3 Opto-Electronic Modelling 76

3.1 Lumerical 77
3.1.1 FDTD 77
3.1.2 Tool 80
3.2 Comparison of Lumerical and Sentaurus 83
3.3 Integration of Lumerical into Sentaurus 86
3.3.1 Tool flow 87
3.3.2 TCAD-Lumerical Interface 92
3.4 Conclusion 97

4 Silicon Nanowire Array 99

4.1 MACE 100
4.2 Fabrication 103
4.2.1 Cleaning 103
4.2.2 Single-step 104
4.2.3 Two-step 105
4.2.4 Single-Side 105
4.3 Results and Discussion 105
4.3.1 Morphology 105
4.3.2 Optical 108
4.4 Conclusion 114

5 **Pyramid structures** **116**
5.1 Background . . . 116
5.1.1 KOH Etching . . . 116
5.1.2 Lithography . . . 120
5.2 Fabrication of Low Density Pyramids . . . 121
5.2.1 Recipe . . . 121
5.2.2 Results . . . 122
5.3 Fabrication using E-Beam Lithography . . . 126
5.3.1 Recipe . . . 126
5.3.2 Results . . . 127
5.4 Fabrication of High Density Pyramids . . . 130
5.4.1 Recipe . . . 130
5.4.2 Results . . . 131
5.5 Conclusion . . . 133
6 **Hybrid structures** **136**
6.1 Simulated Optical results . . . 136
6.2 Morphology . . . 138
6.3 Experimental Optical Measurements . . . 143
6.4 Electrical response . . . 144
6.5 Conclusion . . . 148
7 **Conclusion and Outlook** **150**
7.1 Key Findings . . . 150
7.2 Outlook . . . 152
7.2.1 Working solar cell . . . 152
7.2.2 NWA transfer . . . 155
7.2.3 Metal-Sulphides . . . 157
7.2.4 Tandem PV with perovskites . . . 160
Bibliography **178**

8 Appendix 1 **179**

8.1 Tools . . . 179
8.2 Surface Profiling . . . 180
8.3 Optics . . . 181
8.3.1 Relflection . . . 181
8.3.2 Transmission . . . 182
8.4 Current-Voltage Measurments . . . 182

9 Appendix 2 **184**

9.1 Introduction . . . 184
9.2 TCAD . . . 185
9.2.1 SProcess . . . 185
9.2.2 SDevice Dark . . . 186
9.2.3 SDevice Light . . . 188
9.3 TCL . . . 191
9.3.1 TDR check . . . 191
9.3.2 TDR to Coordinate List . . . 192
9.3.3 Carrier Generation Data to TDR . . . 192
9.4 MATLAB . . . 193
9.4.1 Coordinate List to Binary List . . . 193
9.4.2 Map Carrier Generation Data . . . 195

List of Figures

1.1 An illustration for the global energy potential of both renewable and finite energy sources. Given the world energy consumption stands at approximately $6 \times 10^{20} J$ annually , the ability to rely on fossil fuels is reaching its limits over the coming decade. However, the abundant solar power available annually shows great potential in tackling the long term energy challenge. . 26

1.2 The National Renewable Energy Laboratory (NREL) conversion efficiencies chart for research solar cells. Cell efficiency results illustrates the varying families of PV technology, which include multi-junction cells, single-junction GaAs cells, crystalline Si cells, thin film technologies, emerging photovoltaics. 27

1.3 A bar chart illustrating the current PV capacity in UK. In the last quarter of 2014, a 4 percentage point increase was observed for the renewable energy share in electricity generation (18% to 22%). It can be seen that PV is a crucial factor in this. 28

1.4 This figure illustrates the solar radiance at both the top of the Earth's atmosphere and at sea level. The data is based on the American Society for Testing and Materials (ASTM) Terrestrial Reference Spectra, and is the standard used by the photovoltaic industry for testing solar cells. The regions for ultraviolet, visible and infrared light are indicated. 29

1.5 This figure illustrates the interface between a P-type and N-type material. E_g is the band gap, E_f is the Fermi level, which lies closer to E_c ,the conduction band, in an N-type material and to the valence band, E_v, in a P-type material. At the interface a transition region, with a width , W_t, is formed containing ionised charges depleted of free carriers. This establishes an electric field, ξ_0 () 30

1.6 The graph illustrates the absorption coefficient, α as a function of wavelength, λ, for different materials. In the case of Si a second order relation can be seen, whereby the shorter wavelengths are absorbed within a few hundred nanometers of traversing the material whilst longer wavelengths can traverse up to hundreds of microns. 32

1.7 This figure illustrates the transition of electrons from the valence band to the conduction band in a direct and indirect bandgap. The latter requires an additional step of phonon emission, highlighted by the purple arrow. . . 33

1.8 a)The current-voltage characteristics of an illuminated p-n diode. b) Characteristics of a solar cell - I_{sc} is the short circuit current, V_{oc} is the open circuit voltage, I_m and V_m are the current and voltage at the maximum power point 35

1.9 This figure provides an equivalent circuit for a solar cell, including parasitic series (R_s) and shunt (R_{sh}) resistances. 36

1.10 a) Schematic of an anti-reflective stack, whereby a dielectric material (n_1) is sandwiched in between air (n_0), and a semiconductor (n_2). b) The reflectivity of bare Si, Si coated with SiO_2, and Si coated with Si_3N_4. The application of a single anti reflective layer shows significant reduction of reflectivity, although for a limited range of wavelengths. The plot was achieved by implementing Eq. 1.4 on MATLAB 40

1.11 The light trapping mechanism using pyramid structures for photovoltaic. The incident light has partial refraction into a pyramid and the remainder reflected onto an adjacent pyramid. 41

1.12 a) Scanning electron micrograph of random sized fabricated pyramids using KOH solution. b) Reflectivity of Si wafers with various surfaces - lapped mechanically polished, damage etched and textured with and without SiO_2 and Si_3N_4 anti reflective layers. 42

1.13 a) External quantum efficiency (EQE) comparing vertical and horizontal GaAs p-i-n NW solar cell. b-d) photocurrent generated by the vertical NW device for 488 nm, 676 nm and 800 nm excitation wavelengths. It is observable that a photocurrent from an area much larger than the size of the laser spot appears for all cases. 44

1.14 The sensitivity of absorption efficiency in Ge NWs as a function of radius and incident wavelength. It can be seen that increasing radii leads to resonances with longer wavelengths. 45

1.15 Two-dimensional plot of Q_{abs} of a SiNW as functions of the λ and diameter. The streaks illustrate the presence of leaky mode resonances. 46

1.16 Guided optical ray in a planar-mirror wave-guide. 47

1.17 (a) Condition of self-consistency, whereby a wave reflects twice and duplicates itself. (b) The two waves interfere and create a pattern that remains constant with z. This occurs only for angles for which self-consistency is satisfied. 47

1.18 Field distributions of the modes of a planar-mirror wave-guide. 47

1.19 The junction types within a nanowire PV. The junction can be of radial, axial or a substrate junction. The former constitutes the most benefits as it provides an increase in junction area as well as the light trapping benefits of the other two. 48

1.20 a) SEM image showing InP NWs fabricated via epitaxial growth with an axially defined p-i-n doped structure. The arrays were patterned with nanoimprint lithography of gold seed particles. b) Superimposed schematics showing the SiOx (blue), TCO (red), and the p-i-n doping layers in the NWs. 49

1.21 SEM image of CdTe NWs grown via Au-catalysed VLS growth, in which Mo substrates are initially coated with thin films of of CdTe. 50

1.22 SEM image of an array of Si wires grown via a Vapour-Liquid-Solid method with Au catalyst. The scale bar represents 20 μm 51

1.23 Fabrication process of SiNW. (a) Deposition of SiO_2 (b) Tuning mask by isotropic reactive ion (RIE) etching of SiO_2 . (c) Anisotropic etching of Si by RIE. (d) Removal of the residual SiO_2 by HF etching. 52

1.24 SEM picture of nanometer-scale rods formed via femtosecond laser pulses onto a Si substrate. (a) Low-magnification image (b) Top of spikes (c) In-between spikes. 53
1.25 a) Reflectance measurements of SiNWA, porous Si (PSi), and polished c-Si. b) Cross-sectional SEM image of SiNWA by metal assisted chemical etching. 54

2.1 Doping concentration for different diffusion times at a temperature of $900°C$ and $1000°C$. The substrate has doping concentration of $1 \times 10^{15} cm^{-3}$ It can be seen that the increase in temperature significantly shifts the junction depths (i.e the point at which the dopants matches the substrate doping of 1e15 cm^{-3}). 60
2.2 Example of deposition commands in SProcess whereby a layer of oxide material is deposited on a silicon nanowire represented as a cylinder on top of a cuboid. (a) without oxide, (b) anisotropic deposition, (c) isotropic deposition and (d) fill deposition. 61
2.3 Illustration of the impact of LER on photo-resist deposition and etch. a) Top view of NW without LER b) 3D view of NW without LER c) Top view of NW after using LER d) 3D view of NW after using LER. 62
2.4 Comparison of Delaunay and non-Delaunay triangulation. It can be seen that no points are within any circumcircle for the Delaunay case. 63
2.5 An example of mesh refinement at an interface of two materials. The mesh density is finest at the interface and coarser as it moves away into the bulk. 64
2.6 Surface plot of junction depth, W with varying anneal times, t, and temperature, T. 71
2.7 Thermally annealed N type NWs with B SOD at 900°C for different times, resulting in dopant inversion at t = 30 min. Red is P dopant and Blue is B dopant. 71
2.8 JV characteristics for varying initial B doping concentration, N_A, on an n-type NW with $n_i = 5{\times}10^{15} cm^{-3}$. The SOD process is undertaken at T = 900 and t= 1 min with $N_A = 5{\times}10^{19} cm^{-3}$, $5{\times}10^{20} cm^{-3}$, $5{\times}10^{21} cm^{-3}$. 72

2.9 Efficiencies, η, for varying initial B doping concentration, N_A, on an n-type NW with $n_i = 5 \times 10^{15} cm^{-3}$. The SOD process is undertaken at $T = 900$ and $t = 1$ min with $N_A = 5 \times 10^{19} cm^{-3}$, $5\times10^{20} cm^{-3}$, $5\times10^{21} cm^{-3}$ 72
2.10 JV characteristics for varying anneal temperature, T, on an n-type NW with $n_i = 5 \times 10^{15} cm^{-3}$ and $N_A = 5 \times 10^{21} cm^{-3}$. The SOD process is undertaken for t= 1 min and 800°C<T<1000°C. 73
2.11 Efficiencies, η, for varying anneal temperature, T, on an n-type NW with $n_i = 5 \times 10^{15} cm^{-3}$ and $N_A = 5\times10^{21} cm^{-3}$. The SOD process is undertaken for t= 1 min and 800°C<T<1000°C. 74
2.12 JV characteristics for varying anneal time, t, on an n-type NW with $n_i = 5\times10^{15} cm^{-3}$ and $N_A = 5\times10^{21} cm^{-3}$. The SOD process is undertaken for $T = 900$°C and 1 min $< t <$ 30 min. 75
2.13 Efficiencies, η for varying anneal time, t, on an n-type NW with $n_i = 5\times10^{15} cm^{-3}$ and $N_A = 5 \times 10^{21} cm^{-3}$. The SOD process is undertaken for $T = 800$°C and 800°C with 1 min $< t <$ 30 min. 75

3.1 This figure illustrates the Yee cell used in the FDTD method. It represents the discretisized electric and magnetic fields in a 3D domain. 78
3.2 The sampling in space and time for the FDTD algorithm. The dashed line represents the present point of the injected fields , and its traversing forward in time is shown between A and B. 79
3.3 The simulation domain for a Lumerical optical solve. The nanowire is represented as a cylinder above a cuboid. The injected plane wave is shown by the grey plane, whereby the purple arrow is the direction of propagation and the blue arrow is the polarisation. The yellow planes illustrate the data monitors. A 2D cross section monitor is used to observe carrier generation within the wire. Also, 2D monitors are used above the injected wave and bottom of the substrate to measure reflectivity and transmission respectively. 81
3.4 Missing field components at the edge of Yee Cell 82

3.5 Variation in reflection spectrum as a function of mesh accuracy. The dashed line represents the accuracy level at which reflection measurements become relatively consistent with increasing accuracy thereafter. The inset illustrates the reflectivity under high accuracy. It can be seen that around wavelength at which resonant modes would occur (i.e. very low reflectivity) the influence of mesh accuracy is more significant. 83

3.6 Comparison of simulation times using multi-core and single-core for Lumerical and Sentaurus Packages. The simulation is of a basic periodic SiNWA formed from a cylinder and a cuboid. The NW has a radius of 75 nm and a height of 500 nm, whilst the bulk region has dimension of 300 nm × 300 nm × 1 μ m. A mesh density of 10 nm is set. The boundaries are periodic in x and y, and PML in z. The structure formed in Sentaurus is shown on the top-right (plotted with SVisual), whilst the simulation domain for Lumerical is shown on the bottom-right (plotted with Lumerical Visualiser). 84

3.7 Comparison of reflected power flux density on silicon nanowire using DFT and single-wavelength simulation with the Sentaurus EMW solver. 85

3.8 An overview of the tool flow used in this work. The key input and output files are shown, as well as the main packages which are called upon and its order of use. The dashed line represents the use of TCL language and Matlab script to interface the files between Sentaurus and Lumerical 87

3.9 Top: Comparison of mesh quality between Delaunay mesh in Sentaurus (left) and Cartesian mesh in Lumerical (right). Bottom: Comparison of the optical carrier generation data, after mapping from Lumerical (right) to Sentaurus (left). The images for Sentaurus are plotted in SVisual and for Lumerical in Matlab. 93

4.1 The process of MACE. (a) Formation of Ag nuclei at the substrate surface due to redox reactions between Ag^+ ions and Si (b) Growth of the Ag nuclei and consequent sinking into the substrate due to oxidative dissolution of the Si surface (c) Preferential charge transfer leading to vertical propagation of Ag nuclei, with remaining material producing standing NWs and accumulation of Ag dendrites at the surface. 100

4.2 Charge transfer between Ag^+/Ag system and valence band of Si 101

4.3 This figure illustrates the influence of temperature, etch time, HF conc. and $AgNO_3$ on the etch length of SiNWA for a single etch step process. The graphs illustrate a linear relationship for time and HF conc, whilst a non-linear relationship for temperature. Furthermore, a peak in etch length is found for the case of increasing $AgNO_3$ conc. 103

4.4 SEM showing a SiNWA cross-section fabricated using the two-step etch process at room temperature, with t_{nucl}= 15, t_{etch}= 20, and 0.03 M $AgNO_3$:5.6 M HF solution. 106

4.5 Silver nanoparticle size formed from MACE process. 106

4.6 SEM images showing SiNWA fabricated using a single step etch process with temperature = 50°C, t_{etch} = 5 min , and 0.06 M $AgNO_3$:2 M HF solution. a) Cross-section view b) Top view c) Image of Ag dendrites during SiNWA formation. The scale bar for images a, b and c is 1 μm, 2 μm, and 3 μm respectively. 107

4.7 Etch length of SiNWA under various etch time, HF conc. and $AgNO_3$ conc. using a single step MACE process at a temperature of 50°C. 108

4.8 Optical measurements for varying length of SiNWA. A kink is observed in the bulk reflectivity between 800 - 900 nm wavelength. This caused by a change in reflectivity of the mirror (see Appendix 1) used as a reference in the measurements and not as a feature of the bulk material. 109

4.9 This figure illustrates the reflection (blue), transmission (green), and absorption (red) spectra for various SiNWA structures as well as a spatial map of carrier generation rate ($m^{-3}\,s^{-1}$). The NWA length is 500 nm. a) Diameter = 50 nm b) Diameter = 100 nm c) Diameter = 150 nm d) Tapered wire with top diameter = 50 nm and base diameter = 150 nm. The presence of confined modes can be observed in the carrier generation profile, corresponding to peaks and troughs in the reflection, transmission and absorption(RTA) data. These increase with increasing diameter. The most significant reduction in reflectivity is observed when tapering the wire. . . . 110

4.10 This figure illustrates the reflection (blue), transmission (green), and absorption (red) spectra for various SiNWA structures as well as their spatial carrier generation profile. The NWA length is 5 μm. a) Diameter = 50 nm b) Diameter = 100 nm c) Diameter = 150 nm d) Tapered wire with top diameter = 50 nm and base diameter = 150 nm. Fabry-perot resonances are observed due to the interface between top (air/NWA) and bottom (NWA/bulk) of the wire. 111

4.11 Reflectivity (%), represented by the colorbar, of various NWA radius as a function of wavelength for short SiNWA. 113

4.12 Reflectivity of SiNWs with varying roughness or disorder. (a): Perfect SiNWA; (b) and (c): rough SiNWAs and (d) is the pseudo disordered case. 114

5.1 a) Si crystal with cubic lattice and the different lattice planes. b-d) Illustrates the density of the packed atoms for planes <111>, <110> and <100>. The densely packed atoms on the <111> direction means it etches much more slowly. e) Pyramid structures formed under crystallographic etching on a <100> substrate. f) Pillar structures formed under crystallographic etching on a <110> substrate. 117

5.2 The impact of KOH conc. and solution temperature on etch rates and surface roughness of the pyramids formed. a) Etch rates increase with increasing temperature b)Increasing KOH conc. leads to a maximum etch rate. c) Increase in KOH conc. leads to increase in roughness. d) Increase in solution temperature leads to increase in roughness. 119

5.3 Resist mask on the substrate post-lithography. a) $W_{ox} = 20\mu m$ b) $W_{ox} = 10\ \mu m$ c) $W_{ox} = 5\mu m$. d) oxide mesa for the case of $W_{ox} = 10\ \mu m$, once the resist is removed. 123

5.4 SEM image of the pyramids formed after crystallographic etching, whereby $W_{ox} = 10\ \mu m$ has the most dense array. a) $W_{ox} = 10\ \mu m$ b) $W_{ox} = 5\ \mu m$ c) $W_{ox} = 20\ \mu m$ including the remaining oxide masks post etch. d) Top view of $W_{ox} = 20\ \mu m$. 124

5.5 Optical measurements for varying low density pyramid arrays. 125

5.6 Optical measurements for different depths of a pyramid formed with $W_{ox} = 5\ \mu m$. 125

5.7 a) Example pattern file b) Example control file. The overall dosage used to write the fields is determined by the dwell time, C, and incrementation, I, in the pattern file, and the beam current in the control file. 126

5.8 a) Oxide mask , with $W_{ox} = 1\ \mu m$, fabricated after e-beam lithography. b) Gaps occur between the writing fields, as well as unwanted spots in the corner and centre of the fields. 127

5.9 SEM image of pyramid array ($W_{ox} = 1\ \mu m$, $t_{etch} = 2$ min) using oxide masks from e-beam lithography. a) Array of densely ordered pyramids and mesas formed from over exposed resist b) The gaps between the writing fields are observed in the pyramid array c) Close up of densely ordered pyramids d) Oxide masks on pyramid array. The scale bar is 10 μm for a and b, and 1 μm c and d. 128

5.10 a) 6 different oxide mask arrays, whereby the writing fields are shifted (by incorporating offsets, Y_δ, in the control file) to counter stage movement error. b) Successful stitching of the writing fields achieved by an $Y_\delta = 6\ \mu m$. 129

5.11 Oxide masks under e-beam lithography with the unwanted centre spot of the array removed. This was achieved by lowering the beam dosage. 129
5.12 Schematic diagram of the process flow used to fabricate the dense array of pyramids. A) oxidation, B) deposit resist, C) expose and develop using mask, D) deposit Cr, E) strip resist, F) etch oxide, G) remove Cr, H) KOH etch of Si, I) BOE of oxide layer. 131
5.13 Oxide mask after lithography of high density array. a) $W_{ox} = 2\ \mu m$ b) $W_{ox} = 1\ \mu m$ c) $W_{ox} = 0.8\ \mu m$. 132
5.14 SEM image of high density pyramid arrays. a) $W_{ox} = 2$ µm b) $W_{ox} = 1$ µm c) $W_{ox} = 0.8$ µm 134
5.15 Optical Measurements for varying high density pyramid arrays. 135

6.1 Reflectivity of bulk, pyramids, NWA and pyramids-NWA. 137
6.2 Spatial map of carrier generation rate ($m^{-3}\,s^{-1}$), in logarithmic scale, of (a) rough, quasi random NWA, (b) bulk, (c) pyramids and (d) pyramids-NWA. 138
6.3 SEM image of a NWA on $W_{ox} = 20\ \mu m$ pyramids. a) Top view of array b)Top view close up of pyramid c) Side view close up of pyramid. 139
6.4 SEM image of a NWA on pyramids, with $W_{ox} = 2\ \mu m$, and NWA on bulk. a) Cross-section view of pyramid-NWA b) Cross-section view of NWA on bulk Si c) Close up cross-section view of pyramid-NWA. The NWAs etch with a uniform skyline and are well aligned. 140
6.5 SEM images illustrating NWA formation on $W_{ox} = 2\ \mu m$ pyramids, the scale bar is $4\mu m$. Inset: close-up view of singular pyramid-NWA. 140
6.6 SEM images illustrating NWA formation on $W_{ox} = 1\ \mu m$ pyramids, the scale bar is $2\mu m$. Inset: close-up view of singular pyramid-NWA. 141
6.7 SEM images illustrating NWA formation on $W_{ox} = 0.8\ \mu m$ pyramids, the scale bar is $1.6\mu m$. Inset: close-up view of singular pyramid-NWA. 141
6.8 SEM image comapring NWA fomration on bulk, pyramids, and a close up view inbetween pyramids (inset). This shows that the valleys in-between the pyramids are more porous Si than NWAs. 142

6.9 SEM images comparing dendrite formation on bulk-NWA array and pyramid-NWA array. Whilst the bulk region contains dendrites of a large variety of sizes, the valleys in-between the hybrid structures contain minimal dendrites. a) Top view of dendrites on bulk-NWA array and pyramid-NWA array b) Close up of dendrites on bulk-NWA c) Close up of dendrites on Pyramid-NWA. 143
6.10 Experimental reflectivity of (a) bulk, (b) NWA, (c) pyramids and (d) pyramid-NWA structures. 144
6.11 Experimental reflectivity of NWA and different density of hybrid structure. 145
6.12 Net Active (cm^{-3}) doping profile of the four different structures. 146
6.13 Simulated current-voltage characteristics of the various structures under AM1.5 illumination. 147
6.14 Influence of the surface recombination velocity (SRV) and the interface trap state density (IFS) on the short circuit current density $J_{sc}(mA/cm^2)$. The white line represents the threshold below which SRV and IFS are required to observe benefits in hybrid structures. 148

7.1 IV characteristics of Al contact on n-type Si substrate with varying annealing treatments. 154
7.2 IV characteristics of Cu-Au contact on p-type Si substrate with varying annealing treatments 154
7.3 This figure illustrates the impact of O_2 composition in an ITO layer on its resistivity (right axis) and transparency (left axis). 155
7.4 PDMS thickness measurements for various spin speeds. 156
7.5 a) SEM image of SiNWA with cracks using a two step etching MACE process and a delamination step. b) An image of transferred SiNWA onto a layer of PDMS on glass substrate. c) The mechanical set up used for the transfer process. A Peltier element is used to apply heat for curing the PDMS whilst a self-levelling vacuum chuck is used to transfer the NW substrate. This work was undertaken with Mr Roger Liew and Dr Chuanbo Li. 157

7.6 Modelled reflection measurements of PbS film (left) and PbS NPs (right) on bulk Si. 158
7.7 Modelled reflection measurements of randomly distributed PbS NPs embedded in SiNWA 159
7.8 Modelled power absorption profile of randomly distributed PbS NPs embedded in SiNWA under varying wavelengths of incident light. 159
7.9 SEM image of PbS NPs deposited onto SiNWA. The scale bar is 200 nm. . 160
7.10 Optical measurements of PbS NPs on bulk Si (left) and in SiNWA (right) . 160
7.11 a) The modelled efficiency against cell thickness for different light trapping schemes under low surface recombination velocity. This shows that with passivation and very good light trapping, thinner cells can offer a performance advantage b) The tandem structure of the proposed device. 162

8.1 An image illustrating the optical setup used to undertake the reflection measurements. The key items are the reflection probe, spectrometer and the halogen light source 182

List of Tables

1.1 A table summarising the key performance parameters, FF, η, I_{sc}, V_{oc}, for various solar cells. . . . 36

2.1 PV characteristics of modelled and experimental SiNWA. Experimental data shown in red. . . . 74

5.1 A table summarising the etch rates on different planes at KOH conc. of 40%. The unit is $\mu m/min$ . . . 118

5.2 Parameters defining the pyramid geometry for a given oxide mask size and etch time for the low density mask. . . . 124

5.3 Parameters defining the pyramid geometry for a given oxide mask size and etch time for the high density mask. . . . 132

6.1 The short-circuit current (J_{sc}), open-cricuit voltage (V_{oc}) and efficiency (η) of various structures, for both passivated (PS) and unpassivated (UPS). . . 147

1 Introduction

1.1 Motivation for Photovoltaic research

It is well documented that the consumption of fossil fuels is neither sustainable nor environmentally friendly. With rising global demand for energy exhibiting no signs of retreat, harmful fuel emissions are reaching record heights. In addition, recent political uprisings, continued natural disasters and volatile energy markets are pushing the global security of energy supplies to its limits [1]. As such, significant changes to the global generation mix are apparent as we move towards a low carbon economy; driving forward the need for clean, renewable energy sources. An attractive means of this is to harvest it directly from sunlight.

The department of energy and climate change have identified Photovoltaic (PV) devices as a key renewable energy technology that can help to create a clean, balanced UK energy mix. The advantages it offers include versatility and scalability, as it can be deployed in a variety of environments from domestic households to commercial buildings as well as on the ground when appropriate. PV projects can be developed and installed very fast compared to other means of renewable energy. Furthermore, solar radiance is both in abundance and free - see Fig. 1.1 [2].

In the past year, the UK has almost doubled its PV deployment, with installed capacity at 4.7 GW in July this year [3]. This led to record solar power generation in the summer, peaking at 8% load during the solstice. Given that the UK government targets renewable energy to contribute 15% of the demand by 2020, the potential role and contribution that PV technology can provide is encouraging. Furthermore, it lays strong foundation towards decarbonising the UK economy.

Currently, conversion efficiencies (see Fig. 1.2) close to 44.7% have been achieved in

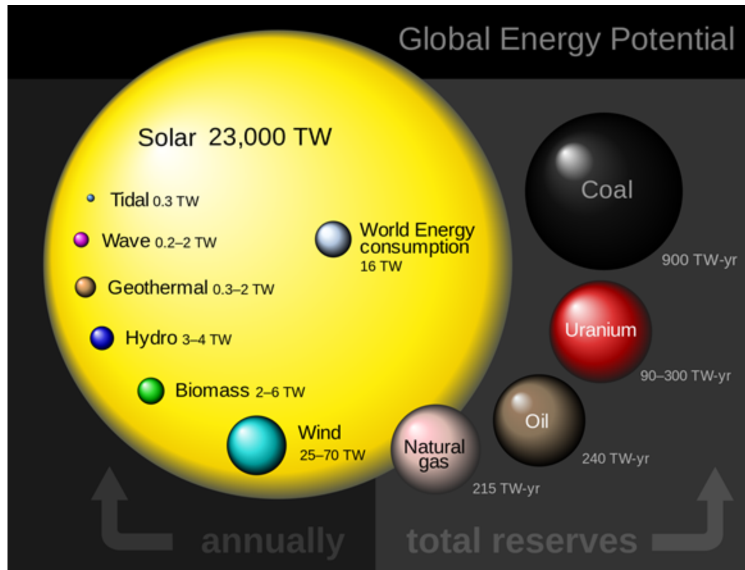

Figure 1.1: An illustration for the global energy potential of both renewable and finite energy sources. Given that the world energy consumption stands at approximately $6 \times 10^{20} J$ annually , the ability to rely on fossil fuels is reaching its limits over the coming decade. However, the abundant solar power a viable annually shows great potential in tackling the long term energy challenge. [2]

research environments [4], whilst commercially manufactured solar cells have reached a significantly lower peak efficiency of around 23% [4]. Whilst significant progress has been made, with installed solar cell capacity able to provide 3-5% of the national load (see Fig. 1.3), they still remain economically non-competitive compared to conventional energy sources such as fossil fuels. In order to make progression and grow the PV sector, further reduction in cost is needed such that it can compete with other low-carbon energy sources. Costs can be reduced through increasing efficiency, reducing materials expense, lengthening the lifecycle and a more recent strategy of integrating it directly into building production. Currently, PV has the highest public approval rating, standing at 85%, of all renewable energy technologies [3]. To retain this, any development and deployment must ensure that community engagement is sustained, including factors such as visual impact and toxicity to environment.

Although technology has advanced rapidly in the last decade, ample literature illustrates that this area has been researched for centuries; with the harnessing of sunlight reported to have existed by civilizations from almost 2 millennia ago. A common starting point is the discovery of the photovoltaic effect by Edmond Becquerel in 1839, in which he

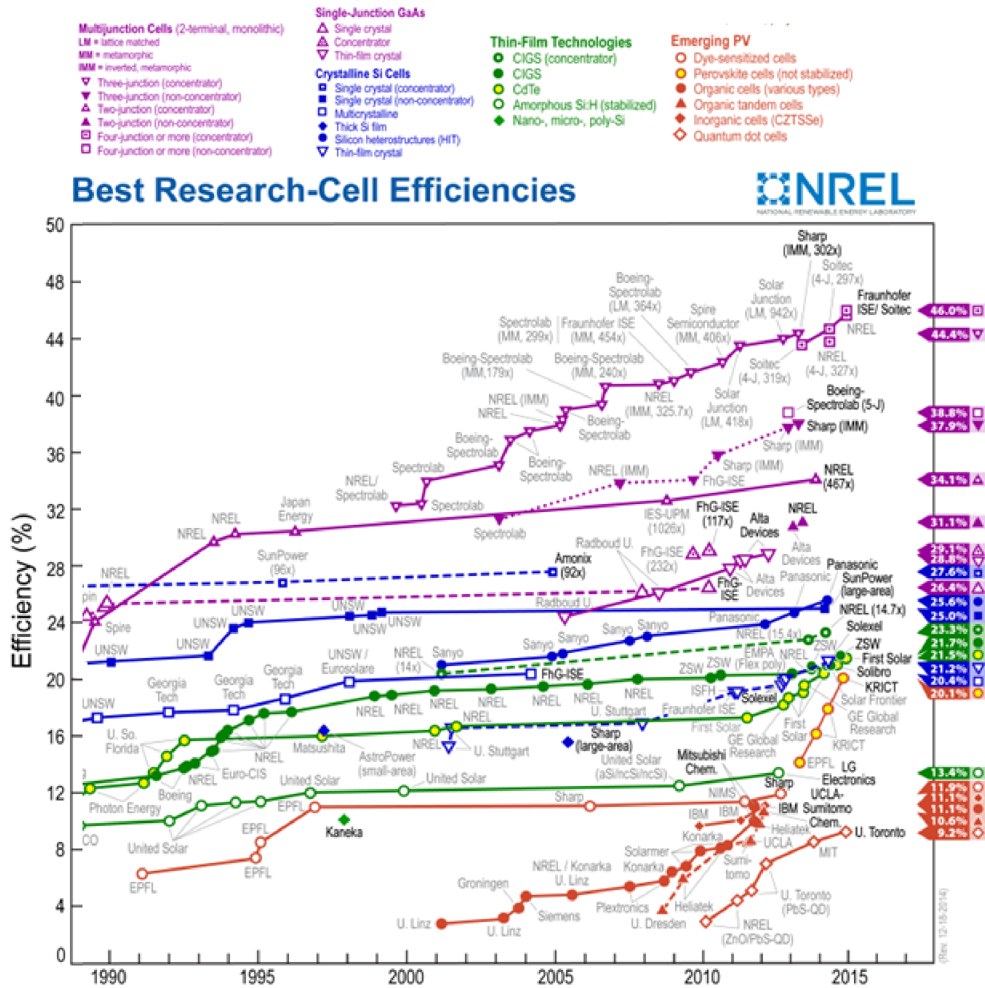

Figure 1.2: The National Renewable Energy Laboratory (NREL) conversion efficiencies chart for research solar cells. Cell efficiency results illustrates the varying families of PV technology, which include multi-junction cells, single-junction GaAs cells, crystalline Si cells, thin film technologies, emerging photovoltaic. [4]

observed a light induced current; similar effects were observed in Se decades later [5]. However, it was not until a century later, that Chapin *et al.* demonstrated the first commercially viable solar cell - a crystalline silicon (c-Si) based solar cell invented at Bell labs in 1954 [6]. The realization of PV technology as an alternative source of power occurred after the oil crisis of the 1970s. The first device generation, which currently still hold the biggest market share, are the solar modules fabricated from mono and poly-crystalline Si wafers. The generation which followed focused on reducing costs by using thin film semiconductors. Of these, the amorphous Si cell, thin poly-crystalline Si on a low cost substrate, the $CuInSe_2/CdS$ hetero-junction cell, and the $CdTe/CdSe$ hetero-junction cell have emerged as commercially significant [5], [7]. Progressing on from this, driven

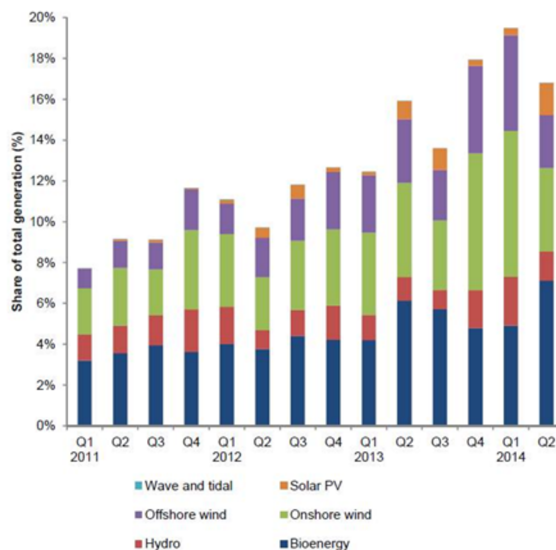

Figure 1.3: A bar chart illustrating the current PV capacity in UK. In the last quarter of 2014, a 4% point increase was observed for the renewable energy share in electricity generation (18% to 22%). It can be seen that PV is a crucial factor in this. [3]

by the need for lower manufacturing costs, dye-sensitized solar cells (DSSC) and organic photovoltaic cells (OPV), based on conducting polymers and fullerenes, were developed [8], [7]. The forefront of current research embraces multi-junction and Si nanotechnology in search of cost effective solar cells with promising efficiencies [4].

1.2 Fundamentals of Solar Cells

1.2.1 Sunlight

The amount of energy that the Earth receives from the sun is $\approx 2{\times}10^{17}\ Js^{-1}$ [9]; which is enough to meet the worldwide yearly demand within one hour [10]. Sunlight not only provides the source of energy for PV technology but is the root supply for most forms of energy on earth. Carbon hungry fossil fuels such as petrol and coal, originate from plant matter a millenia ago, which grew from the photosynthesis of sunlight and is thus stored solar energy. Cleaner forms of energy are also indirectly sourced from the sun such as wind energy and hydroelectricty. These are based on heat from sunlight which generate air currents to form wind and evaporate water to form rain. PV technology provides a direct means to harvest sunlight into electrical power, thereby utilising an ample source

of energy that is fundamental to the existence of earth and its ecosystem.

The sun is a hot plasma emitting thermal radiation with a temperature of ≈ 6000 K. Using Planck's law [11], established by Max Planck in 1900, the spectral irradiance (defined as the irradiance of a surface per unit wavelength, with units $Wm^{-2}\ nm^{-1}$) for a black body can be represented. The AM1.5 spectrum, shown in Fig. 1.4, best represents the solar irradiance on earth's surface given the absorption of dust and molecules within the atmosphere. Whilst the amount of energy irradiated by the sun is vast, in order to harness it, the bandgap, E_g, of any PV device material must first fit well with the AM1.5 spectrum.

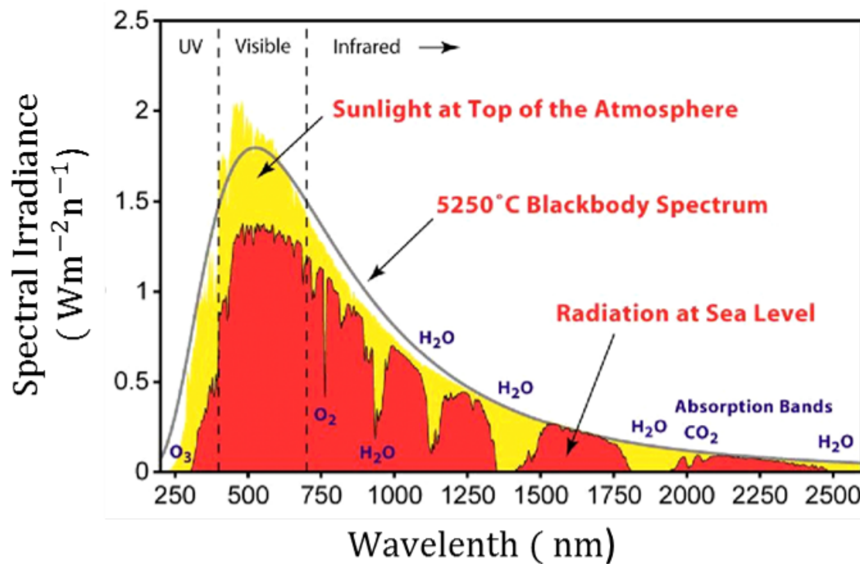

Figure 1.4: This figure illustrates the solar radiance at both the top of the Earth's atmosphere and at sea level. The data is based on the American Society for Testing and Materials (ASTM) Terrestrial Reference Spectra, and is the standard used by the photovoltaic industry for testing solar cells. The regions for ultraviolet, visible and infrared light are indicated. [12]

The spectrum spans from ultra-violet, through visible and onto infra-red wavelengths. The largest proportion of energy occurs within the visible spectrum 400 - 700 nm. Relating wavelength, λ, to photon energy , E_{ph}, using the following equation:

$$E_{ph} = \frac{hc}{\lambda} \tag{1.1}$$

where h is Planck's constant and c is speed of light, gives an energy band of 3.1 - 1.8 eV for a corresponding wavelength range of 400 - 700 nm.

1.2.2 Device

The p-n junction is the core element within a solar cell. An archetypical device is made of a homojunction formed from Si. This is a semiconductor material with a bandgap $E_g =$ 1.1 eV. This property of the material is an important factor since photons of energy (E_{ph}) greater than this can generate electron-hole pairs (EHP) whilst photons of energy less than this fail to be absorbed and are consequently lost. When ($E_{ph} \geq E_g$), bound electrons from the valence band of the material are excited to the conduction band to become free carriers; thereby leaving a free hole in the valence band. At the interface between a p-type material, with a Fermi level closer to the valence band, and an n-type material, with a Fermi level closer to the conduction band, a potential barrier is formed equal to the difference in work function, see Fig. 1.5. The established electric field in the depleted region prevents the flow of majority carriers, whilst driving minority carriers across the junction. In the dark, thermally generated minority carriers that are within the diffusion

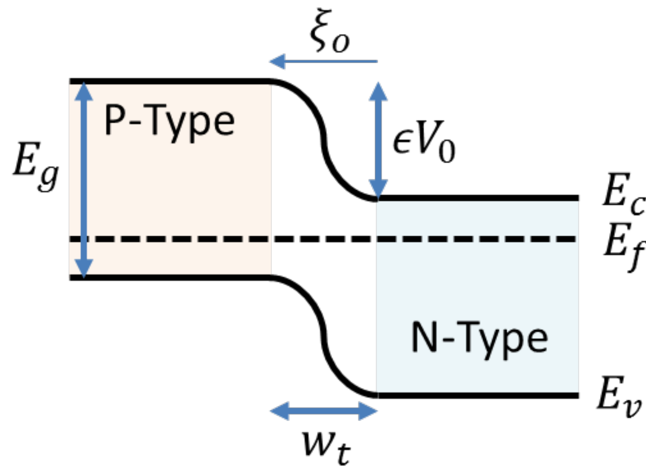

Figure 1.5: This figure illustrates the interface between a P-type and N-type material. E_g is the band gap, E_f is the Fermi level, which lies closer to E_c ,the conduction band, in an N-type material and to the valence band, E_v, in a P-type material. At the interface a transition region, with a width , W_t, is formed containing an insulating area depleted of free carriers. This establishes an electric field, ξ_0 and a built in voltage eV_0 equal to the difference in workfunction $(e\phi_p - e\phi_n)$

length (Ln, Lp) of the junction will be swept across by the electric field, this is the drift current across the junction. When this junction is illuminated, a generation of carriers with a rate, g_{op}, measured in $cm^{-3}s^{-1}$,will occur. These carriers will consist of minority carriers, n_p and p_n, generated per second within a diffusion length of the transition region;

as well as within the transition region itself. Majority carriers n_n and p_p are not considered because in a p-n junction excess minority carriers limit maximum current that can flow. The current as a result of collecting these optically generated minority carriers can be defined as:

$$I_L = qAg_{op}(L_p + L_n + W_t) \tag{1.2}$$

where q is the elementary charge, A is the area, L_p and L_n are the diffusion lengths, and W_t is the transition region width. Alongside the standard pn junctions, a p-i-n junction formation has also been utilised in solar cells. This incorporates an intrinsic layer sandwiched in between the p and n regions, thereby increasing the area in which the photons can be generated and converted. The generation of carriers depend on the absorption coefficient, the thickness of material and the number of photons incident on the material. These can be related using the following equation [13]:

$$g_{op}(E, x) = [1 - R(E)]\alpha(E)b_s(E)e^{-\int_0^x \alpha(E,x')dx'} \tag{1.3}$$

where

- $g_{op}(E, x)$ is the generation rate as a function of the photon incident energy, E, and distance into the material, x. $[cm^{-3}s^{-1}]$
- $R(E)$ is the reflectivity.
- $b_s(E)$ is the incident spectral photon flux density. $[cm^{-2}s^{-1}]$
- $\alpha(E)$ is the absorption coefficient. $[cm^{-1}]$

$b_s(E)$ is determined by the aforementioned AM1.5 spectrum. However, not all of the incident photons is absorbed by the material. Some is reflected at the surface, whilst others will be transmitted through the device. Both the reflected and transmitted incident photons are regarded as a loss of energy and do not participate in the photo-generated current. $\alpha(E)$ determines how the absorbed photons are utilised to excite carriers. This material parameter determines how far a photon, with a given energy, can traverse through a material before being absorbed. $\alpha(E)$ for different materials is given in fig 1.6.

As a photon is absorbed in Si, an indirect transition (through phonon emmision) is required for an electron to be excited from the valence band to the conduction band such that total momentum is conserved, see Fig. 1.7. This is because Si has an indirect

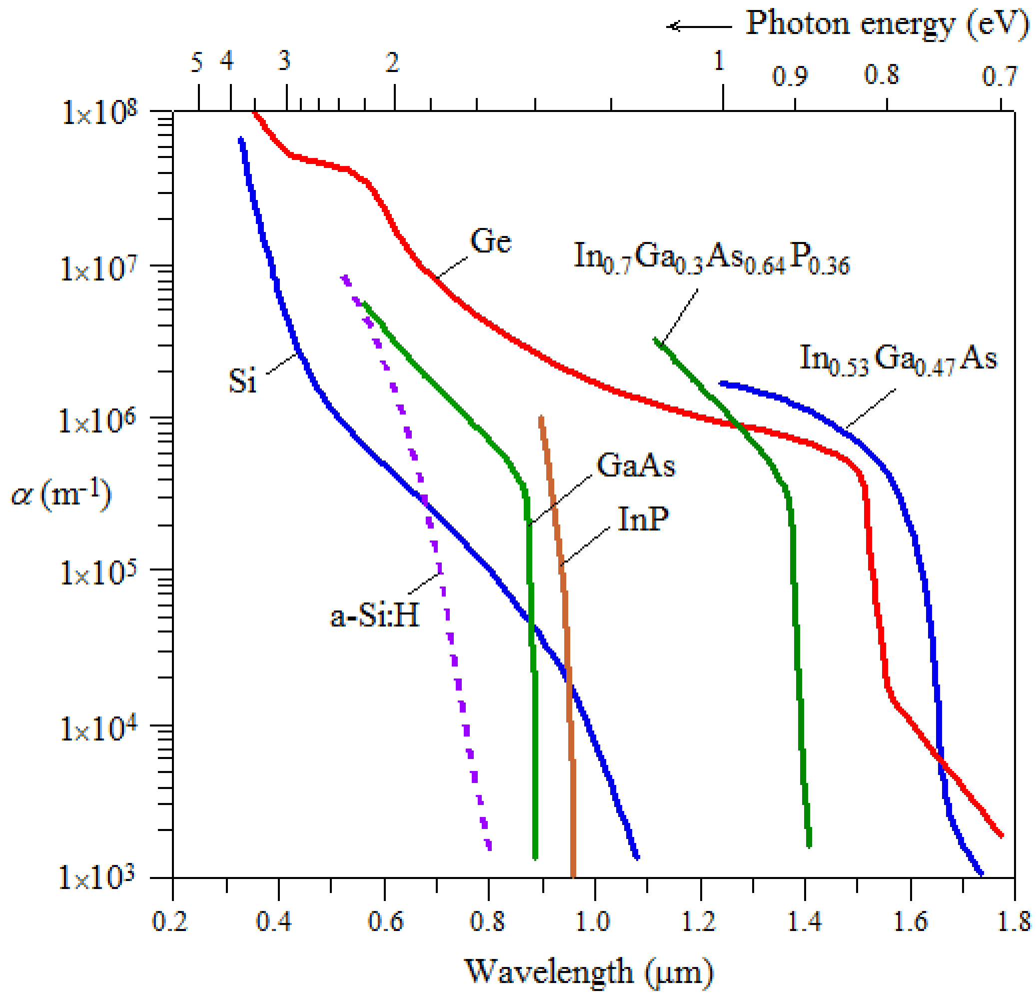

Figure 1.6: The graph illustrates the absorption coefficient, α as a function of wavelength, λ for different materials. In the case of Si a second order relation can be seen, whereby the shorter wavelengths are absorbed within a few hundred nanometers of traversing the material whilst longer wavelengths can traverse up to hundreds of microns. [14]

bandgap. Equations defining energy and momentum conservation for this transition are defined as follows [15]:

$$hv = E_a - E_b + hv_{ph} \tag{1.4}$$

$$k = k_a - k_b + k_{ph} \tag{1.5}$$

where

h is the Planck's constant

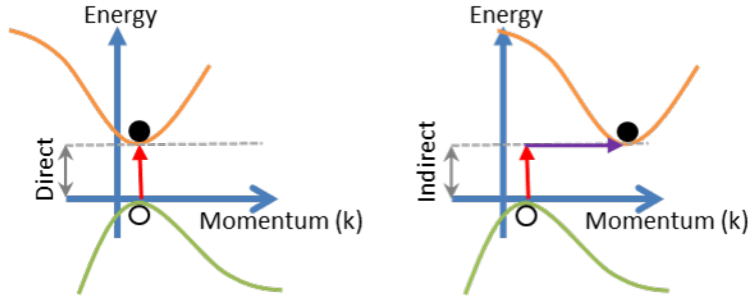

Figure 1.7: This figure illustrates the transition of electrons from the valence band to the conduction band in a direct and indirect bandgap. The latter requires an additional step of phonon emission, highlighted by the purple arrow.

a and b denote the initial and final state of the electron, which in this case will be from the valence band to the conduction band.
v and k are frequency and wavevector of the photon
v_{ph} and k_{ph} are frequency and wavevector of the phonon

Relating the absorption coefficient to the photon energy results in a second order relation, also observable from Fig 1.6.

$$\alpha \propto (hv - E_g - hv_{ph})^2 \tag{1.6}$$

$g_{op}(E, x)$ is highest at the surface and reduces exponentially with penetration depth, x. This suggests that in order to utilise the maximum amount of generated carriers, the p-n junction should exist as close to the surface as possible. However, the location of the junction should also consider the efficiency in separating and collecting these carriers.

The likelihood that a generated minority carrier will reach the junction so that it can be swept across the junction and be collected at the terminal is reduced by recombination events. There are three common forms of recombination: Radiative, Auger and Trap Assisted. The first is unavoidable yet is a strong limiting factor in the efficiency of direct band-gap solar cells. This recombination event occurs due to the relaxation of electrons across a band gap, subsequently releasing a photon. Auger recombination is the relaxation of a charged carrier with the emitted energy exciting another charged carrier to a higher energy state and is important in heavily doped Si [13]. Trap assisted events occur with the relaxation of an electron into an intermediate state in the band gap, before recombining with a hole in the valence band; the energy lost is given up as heat (phonons).

The collection probability of photo-generated minority carriers (i.e. the probability that an electron or hole will be swept across the electric field) is highest near the p-n junction, and decreases with distance away from it. Generated carriers near the surfaces are very unlikely to be collected since they are far away from the junction and dangling bonds mean that trap assisted recombination is prevalent.

The collection of light generated carriers by the p-n junction will cause holes to traverse towards the p-type region and electrons will move towards the n-type region. If the device is under short circuit condition, the carriers exit the device as light generated current (I_L) and therefore there is no build up of charge. However, under open-circuit conditions, the collected light generated carriers cannot flow out of the device. Therefore, an increase in the number of electrons on the n-type side and similarly an increase in holes in the p-type side is observed. This separation of charge will impose an electric field across the junction, opposing the field which already exists, and as such reduce the net electric field. This reduction of the electric field increases the forward bias diffusion current. This reverse current is often referred to as the dark current (I_0); since this is the current that would be produced if the solar cell was under bias without illumination. In the dark, the solar cell is essentially a diode. The net current in a solar cell, when illuminated, will be the photocurrent (I_L) minus the dark current (I_0). A new equilibrium is reached when the light-generated current is exactly balanced by the forward bias diffusion current, and the net current is zero. The bias required to balance these two currents is called the open circuit voltage. Applying the superposition principle to solar cell analysis [16], leads to the following: .

$$I \approx I_0 e^{\frac{q(V)}{kT}} - I_L \tag{1.7}$$

$$V_{oc} = \frac{kT}{q} ln(\frac{I_L}{I_0}) \tag{1.8}$$

Therefore, the charge separation of the optically generated carriers will develop a photovoltage (V_{oc}) at open circuit and establish a photocurrent (I_{sc}) in short circuit, see Fig. 1.8a. In the presence of a load, the solar cell can do electrical work since both voltage and current are produced, see Fig. 1.8b.

V_{oc} is limited since an increase in minority carriers by optical generation will in turn increase the recombination rate. Since the maximum applied forward bias that can appear across a junction is the contact potential, the photovoltage will reach this limit.

Fig 1.8 [13] shows typical current-voltage characteristics. Although I_{sc} and V_{oc} give the maximum current and voltage output respectively from a solar cell, it produces no power. When illuminated, a maximum power point (MPP) is observed. Ideally the solar cell should operate at this point with a current, I_m, and voltage, V_m. The Fill Factor (FF) gives the "squareness" of the curve; relating I_m, V_m, I_{sc}, V_{oc}:

$$FF = \frac{I_m V_m}{I_{sc} V_{oc}} \tag{1.9}$$

The efficiency of the solar cell is defined as the power delivered at the operating point, MPP, as a fraction of the incident light power, P_s:

$$\eta = \frac{I_m V_m}{P_s} = \frac{I_{sc} V_{oc} FF}{P_s} \tag{1.10}$$

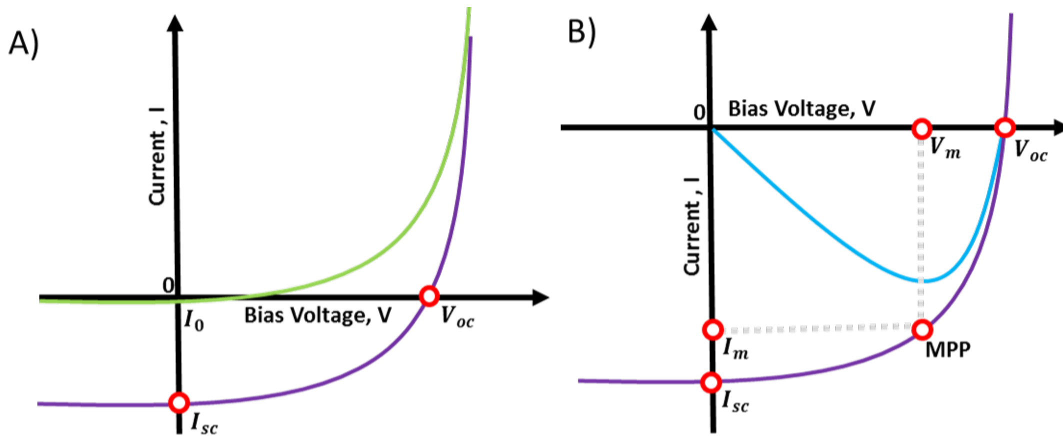

Figure 1.8: a)The current-voltage characteristics of an illuminated p-n diode. b) Characteristics of a solar cell - I_{sc} is the short circuit current, V_{oc} is the open circuit voltage, I_m and V_m are the current and voltage at the maximum power point [13].

Parasitic resistances dissipate power and thereby reduce the efficiency in the solar cell, see Fig. 1.9. The resistance to current flow in the cell, predominantly through the contacts, leads to series resistance (R_s); whilst leakage currents leads to low shunt resistance (R_{sh}) [13]. The main performance characteristics, FF, η, I_{sc}, V_{oc}, for various solar cells are shown

in Table 1.1. These include crystalline Si (c-Si), Dye Sensitized Solar Cells (DSSC)[1] and Multi-junction[2] .

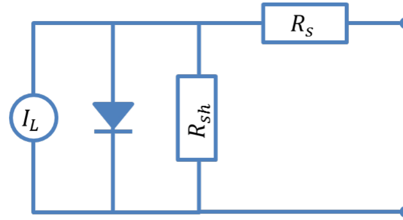

Figure 1.9: This figure provides an equivalent circuit for a solar cell, including parasitic series (R_s) and shunt (R_{sh}) resistances.

Table 1.1: A table summarising the key performance parameters, FF, η, I_{sc}, V_{oc}, for various solar cells. [19]

Solar Cell	J_{sc}	V_{oc}	FF	η
Standard c-Si	41.8	0.74	82.7	25.6
Thin film c-Si	38.1	0.68	77.4	20.1
Thin film CdTe	28.6	0.85	80.0	19.6
DSSC	22.5	0.74	71.2	11.9
Multi-junction	14.27	3.07	86.7	37.9

In order to reduce optical reflection, $R(E)$, a typical inorganic solar cell will have a textured surface with an antireflection layer. The contacts are usually buried to minimise shading effects. Beneath the surface, it is common to find a thin n-type layer followed by a vastly thicker p-type layer. This is because electron mobility in the p-type layer is greater than the hole mobility in the n-type layer for the same doping density; therefore a large p-type layer will increase the efficiency of carrier collection. Having the p-n junction close to the surface is a compromise between avoiding the effects of surface recombination whilst maximising the separation of generated charge carriers. Furthermore, a thin oxide coating is often used for passivation of the front surface in order to reduce surface recombination [13]. The structure also has heavily doped layers surrounding the front and back contacts; this provides a reduction in contact resistance and forms ohmic contacts.

[1]These are photo-electrochemical cells which implement the optical absorption and charge separation using a sensitiser that generally has a wide band gap and non-crystalline morphology [17]

[2]These cells contain multiple junctions using different band-gap materials to utilise a broader wavelength spectrum [18]

1.2.3 Theoretical limit

The maximum theoretical efficiency, η, of a photovoltaic device with a single p-n junction is defined by detailed balance technique proposed by Shockley and Queisser in 1961 [20], and is referred to as the Shockley and Queisser limit. This limit examines the amount of electrical energy utilized per incident photon. The three factors to consider are:

Spectrum Losses The bandgap of the solar cell material will place an abrupt limit on the amount of energy utilised from the incident spectrum. For the case of Si, this is 1.1 eV. All photons with energy less than this will not excite electrons from the valence band to the conduction band. Further losses in energy from the incident spectrum also occur from photons that exceed the energy of the bandgap. The excess energy is not captured by the cell but is dissipated as heat. These bandgap associated losses are the dominant limiting factors, reducing the theoretical efficiency down to 48%.

Recombination The recombination processes described earlier place an upper limit on the generation rate of EHPs, in particular radiative recombination. These losses limit the V_{oc} and reduce the theoretical efficiency by 10% in addition to the thermal losses.

Blackbody radiation A solar cell at room temperature (300 K) will emit spontaneous thermal radiation known as blackbody radiation. This energy cannot be captured by the cell, and represents approx 7% loss of the incident energy of the sun (6000 K). Inefficiencies in a PV device generally results in energy lost as heat, therefore under sunlight the temperature of a solar cell will increase. The intensity at all wavelengths of the blackbody radiation increases with increasing temperature until equilibrium.

Given these limits under an AM1.5 spectrum, a single junction c-Si solar cell has a maximum $J_{sc} \approx 43\ mA\ cm^{-2}$ and a minimum $J_0 \approx 1\ fA\ cm^{-2}$. This equates to a theoretical efficiency limit of approximately 33%.

1.3 Key role: Light trapping

Taking into consideration the operation and limits of a solar cell, as described previously, it is clear that the design principles for maximising a single junction cell efficiency are:

- increase light collection by the solar cell
- increase generated carrier collection by the p-n junction
- minimise the forward bias dark current
- minimise resistive losses.

The focus of this project is to implement the first two principles. Optical losses occur due to the reflectivity at the surface and also the shadowing from contact regions. Minimising the contact area or applying transparent electrodes will often be at the expense of increased series resistance. The primary issue of high surface reflectivity of materials, such as Si, can be tackled through anti-reflective coatings and surface texturing [21–27]. Furthermore the optical path of light entering the solar cell can be increased through light trapping strategies, that increase the density of generated carriers.

The reflectivity, R, between air and a slab of Si under perpendicular irradiation can be determined by:

$$R = (\frac{n_{air} - n_{Si}}{n_{air} + n_{Si}})^2 \tag{1.11}$$

where n_{air} is the refractive index of air and n_{Si} is the refractive index of Si. Fig 1.10b plots the reflectivity from 400 nm to 1100 nm wavelength range.

1.3.1 Anti-reflective coatings

Anti-reflective coatings (ARC) are prevalent in many lens technologies as well as solar cells [28]. They utilise a thin layer of dielectric material above the semiconductor material such that interference effects lead to reduced reflectivity. The thickness of the anti-reflective coating is chosen such that the reflected wave from its surface is out of phase with the wave reflected from the semiconductor surface. Destructive interference will occur as from the out of phase wave and thus the reflected energy is zero net.

The thickness of the coating is dependent on the wavelength of the incident wave on the dielectric material. The minimum reflection is given by a thickness, d, of a material with refractive index, n_1, in the following relation [29]:

$$d = \frac{\lambda}{4n_1} \tag{1.12}$$

Alongside the thickness of the coating, the refractive index is also chosen such that it is the geometric mean of the materials on either side, i.e. silicon and air. This is expressed by:

$$n_1 = \sqrt{n_0 n_2} \tag{1.13}$$

where n_0 is refractive index of surrounding material, n_2 is refractive index of semiconductor and n_1 is optimal refractive index of the anti-reflection layer.

The reflectivity for a single layer ARC above a given semiconductor material with thickness t_1, see Fig. 1.10a, can be calculated by [29]:

$$R = \frac{r_1^2 + r_2^2 + 2r_1 r_2 cos2\theta}{1 + r_1^2 r_2^2 + 2r_1 r_2 cos2\theta} \tag{1.14}$$

where:

- $r1 = \frac{n_0 - n_1}{n_0 + n_1}$
- $r2 = \frac{n_1 - n_2}{n_1 + n_2}$
- $\theta = \frac{2\pi n_1 t_1}{\lambda}$.

The plot for reflectivity of a common silicon nitride material above a c-Si solar cell is shown in 1.10b.

Whilst ARC can reduce overall reflectivity, in the single layer case its largest impact is at a sole wavelength (in general focuses on 0.6 μm as it has the highest intensity peak for the AM1.5 spectrum) rather than a broadband spectrum of the incident light. This can be improved with multiple layers. Green *et al.* optimized a double layer ARC using ZnS and MgF_2 for high-efficiency Si solar cells by solving a multilayer non-absorptive thin-film coating system using a matrix method [30]. Whilst ARC improves solar cells performance, it also introduces complexities in processing passivated layers and contact layer as well as increasing expense.

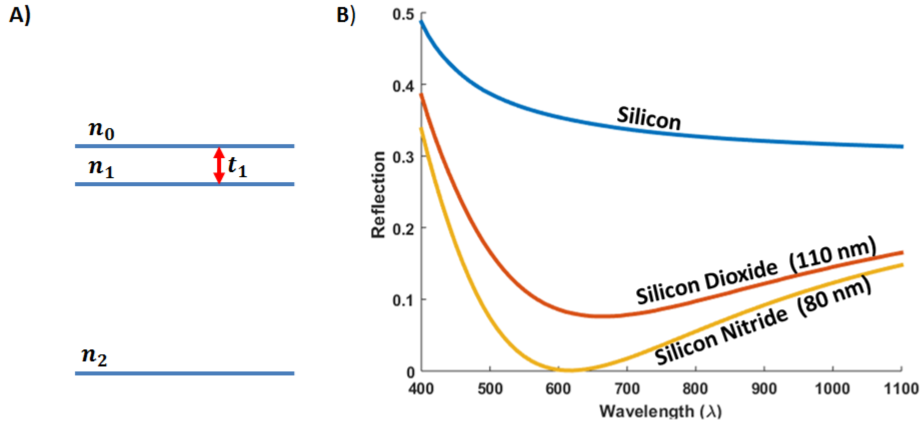

Figure 1.10: a) Schematic of an anti-reflective stack, whereby a dielectric material (n_1) is sandwiched in between air (n_0), and a semiconductor (n_2). b) The reflectivity of bare Si, Si coated with SiO_2, and Si coated with Si_3N_4. The application of a single anti reflective layer shows significant reduction of reflectivity, although for a limited range of wavelengths. The plot was achieved by implementing Eq. 1.4 on MATLAB

1.3.2 Surface Texturing

Alongside anti-reflective coatings, another common technique in reducing reflectivity is to implement surface texturing. This is more effective as this technique of light trapping may also increase the optical path length of the incident light to several times the thickness of the solar cell. The optical path length is defined as the distance travelled by an unabsorbed photon exiting the device, either by reflection at the front or transmission at the back. The incident light can be trapped in the solar cell by implementing an angled (rough) surface rather than a flat (smooth) surface. The roughness of the surface will couple light obliquely into the semiconductor material and as such increases the optical length - see Fig. 1.11. This is more effective as this technique of light trapping may increase the optical path length of the incident light to several times the thickness of the solar cell. The angle of refracted light can be calculated using Snell's Law [29]:

$$n_0 sin\theta_0 = n_1 sin\theta_1 \tag{1.15}$$

where θ_0 is the incident light angle relative to the normal plane of the interface and θ_1 is the refracted angle.

A common method is to implement crystallographic etching on single crystalline solar

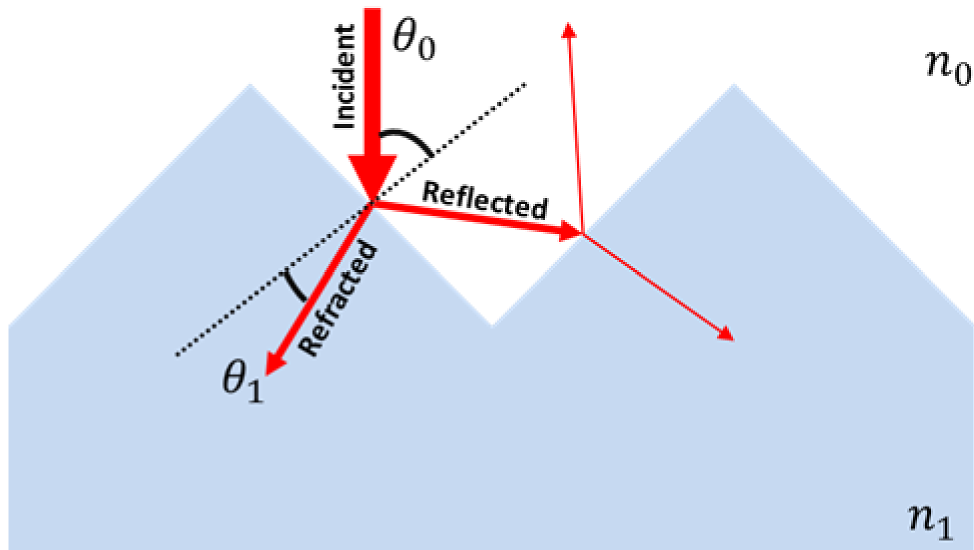

Figure 1.11: The light trapping mechanism using pyramid structures for photovoltaic. The incident light has partial refraction into a pyramid and the remainder reflected onto an adjacent pyramid.

cells to form random pyramids [31]. This occurs due to the etchant reacting differently along the different faces of crystal planes. Singh *et al.* reports the use of this etching process by using Si wafers in inorganic alkaline solutions for use in commercial solar cells. The use of KOH and NaOH solutions, with the addition of Isopropanol, produced effective surface texturisation (see Fig. 1.12a) by forming straight pyramids at prefered sites due to crystalline defects and wetting [31]. The use of these pyramids reduced reflectivity to 11%-14% for the wavelength range 450 nm -1000 nm, see Fig. 1.12b [31]. The addition of anti-reflective coatings on the textured surface reduced reflectivity down to less than 3%. Furthermore, they related improvements in J_{sc} directly to the optical effectiveness of the textured surface. A more comprehensive analysis of crystalline etching is discussed in chapter 5.

Light can be trapped even further by introducing roughness to the rear of the solar cell. The Lambertian back reflector is designed to reflect light in random directions and when implemented at the rear of a solar cell can direct a large amount of light back into the device giving unabsorbed photons an increased probability of absorption [32]. This scattering of light from the rear surface can lead to light undergoing total internal reflection on returning to the top surface. Total internal reflection will occur when light passes from a high refractive index medium to a low refractive index medium. The angle at which this

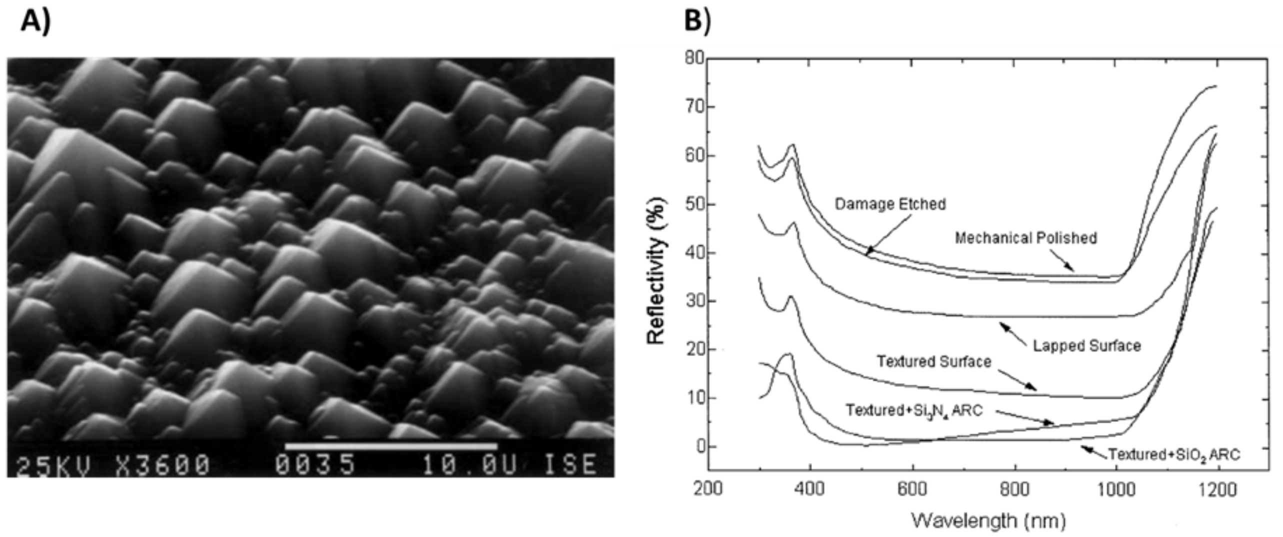

Figure 1.12: a) Scanning electron micrograph of random sized fabricated pyramids using KOH solution. b) Reflectivity of Si wafers with various surfaces - lapped mechanically polished, damage etched, pyramidal textured, and pyramidal textured with anti reflective layers. [31]

occurs can be found using the following relation:

$$\theta = sin^{-1}(\frac{n_0}{n_1}) \tag{1.16}$$

Using these trapping mechanisms the optical path length of the incident spectrum can be enhanced up to a factor of $4n^2$, where n is the refractive index of the substrate. This is almost 50 times the device thickness for the silicon case . This theoretical limit was first proposed by Yablonovitch and Cody [33] and is only applicable when the geometry of the device is much larger than the wavelength of the incident light.

1.3.3 Surpassing the Ray Optics Limit

When the geometry of the device approaches the wavelength of the incident spectrum, the propagation of light no longer follows the ray optic theory but can be described better by wave optics. In this case, the ray optic limit can be surpassed and further light trapping can be achieved. For the case of silicon solar cells, this can occur when using nanostructures such as a nanowires and nanoparticles.

A formulation for particle-light interaction structures comparable to the wavelength can be achieved using Mie theory, developed by Gustave Mie in 1908 [34]. This utilises

the electromagnetic wave (EMW) concept and employs Maxwell's equations to derived incident, scattered and internal fields. When an EMW is incident on a particle, discrete electric charges such as protons and electrons oscillate to emit secondary radiation known as scattering. If the particle has a complex index of refraction then it will also absorb (due to excitation of oscillating dipoles) the incident radiation and thus extinguish some of the incident light. The reduction of incident light as it traverses through a particle is known as extinction (i.e. the net effect of absorption and scattering).

The type of scattering from a particle with an incident photon is determined using the dimensionless Mie parameter [35]:

$$\alpha_{mie} = \frac{2\pi r}{\lambda} \tag{1.17}$$

where r is the radius of the particle, and λ is the wavelength of the incident light.

The type of scattering can then be classified in terms of α_{mie}:

- Mie-Scattering ($0.1 < \alpha_{mie} < 50$)
- Geometric (optics) scattering ($\alpha_{mie} > 50$)
- Rayleigh Scattering ($\alpha_{mie} < 0.1$)

The amount of light extinction is dependent on the geometrical cross section of the particle as well as the optical properties like dielectric constant of the particle and the surrounding medium. Furthermore, a cross-sectional area can be used to analogise the interaction between the incident EMW and the electronic charges within a particle.

According to Mie theory, the extinction cross section area, C_{ext}, is proportional to the extinct power. The extinction efficiency, Q_{ext}, in the object can be described by:

$$Q_{ext} = \frac{C_{ext}}{A_{light}} \tag{1.18}$$

where A_{light} is the area under illumination.

In the regime of geometric optics, a perfect absorbing black body will have an $Q_{ext} = 1$ as $C_{ext} = A_{light}$ and an imperfect absorber, where $C_{ext} < A_{light}$, will have $Q_{ext} < 1$. However, when light is incident on structures of sub-wavelength, $Q_{ext} > 1$ has been observed.

The efficiency of gallium aresenide (GaAs) solar cells was estimated to surpass its Shockley-Queisser limit using a p-i-n NW structure [36]. The generation of ultra high photo generated current is attributed to a resonance trapping effect caused by the geometry of NW at sub-wavelength scale. The results of this work show that the effective absorption area is far greater than the cross sectional area of the NW, see Fig. 1.13, and thus the Q_{ext} is approximately 8 times greater than the Beer-Lambert law prediction [36].

.

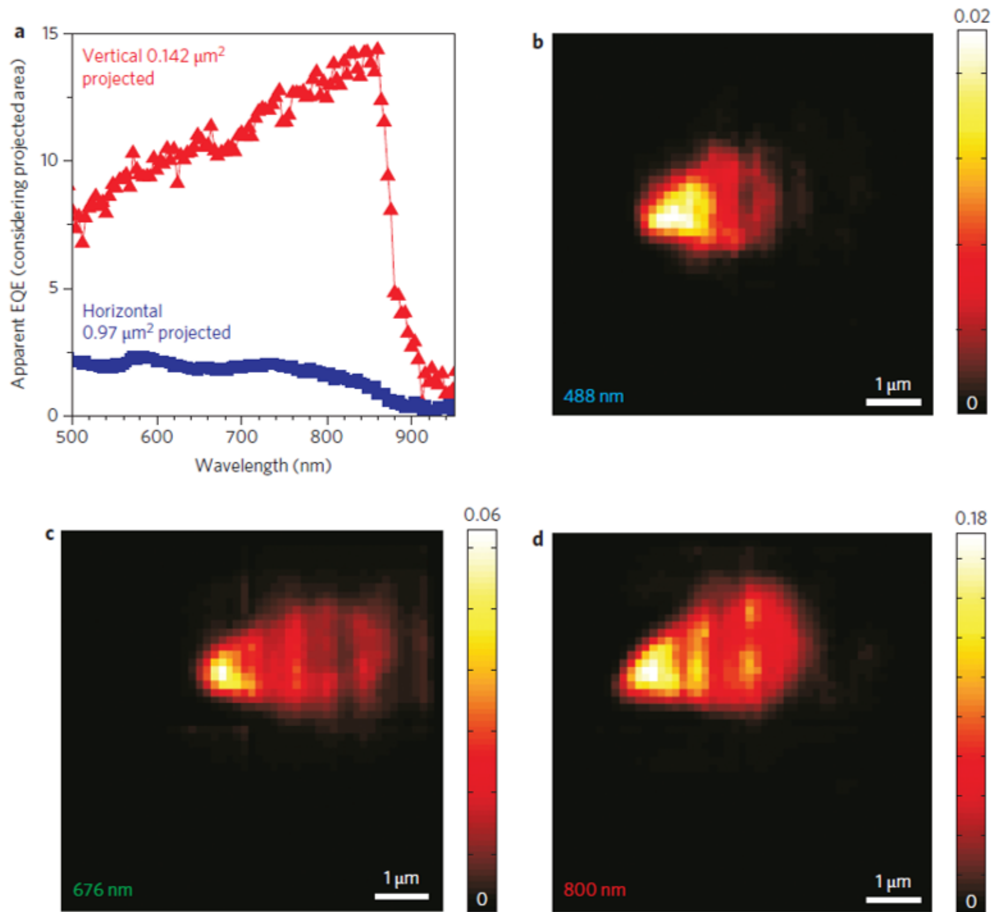

Figure 1.13: a) External quantum efficiency (EQE) comparing vertical and horizontal GaAs p-i-n NW solar cell. b-d)photocurrent generated by the vertical NW device for 488 nm, 676 nm and 800 nm excitation wavelengths. It is observable that a photocurrent from an area much larger than the size of the laser spot appears for all cases [36].

Cao *et al.* uses the Lorentz-Mie theory to provide an understanding to the enhanced Q_{abs} observed [37]. The paper views a NW as a microcylinder resonator that traps light through multiple internal reflections and as such exhibits resonant leaky modes. This work

also observes the sensitivity of Q_{abs} to the radius of the NW and the wavelength of incident radiation. Resonances are observed for specific wavelength and diameter interactions, and as such branches appear in an Q_{abs} spectra - see Fig. 1.14.

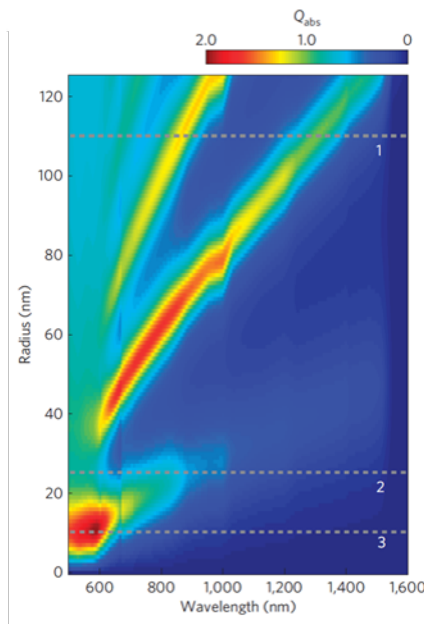

Figure 1.14: The sensitivity of absorption efficiency in Ge NWs as a function of radius and incident wavelength. It can be seen that increasing radii leads to resonances at longer wavelengths. [37]

Similar results are observed by Cao *et al.* for the case of SiNWs [38]. Fig. 1.15 illustrates Q_{abs} of a c-Si NW as functions of the λ and diameter. Distinct streaks of high intensity is observed and this indicates the presence of the various leaky mode resonances [38].Furthermore, these correspond to photocurrent enhancement peaks. These resonant modes are due to the high refractive index of the NW compared to its surroundings, thereby trapping the light by multiple internal reflections from its boundary. This is somewhat analogous to the simpler case observed in planar wave-guides. Fig 1.16 shows a ray-optics picture of light being guided by multiple reflections. If a transverse electromagnetic plane wave (TEM) is associated to each optical ray, then a self-consistency condition is imposed by requiring that as the wave reflects twice, it reproduces itself, so that we have only two distinct plane waves, see Fig. 1.17. Fields that satisfy this condition are called the modes, or eigenfunctions, of the wave-guide [39]. As a general definition, modes are fields that maintain the same transverse distribution and polarization at all locations along the

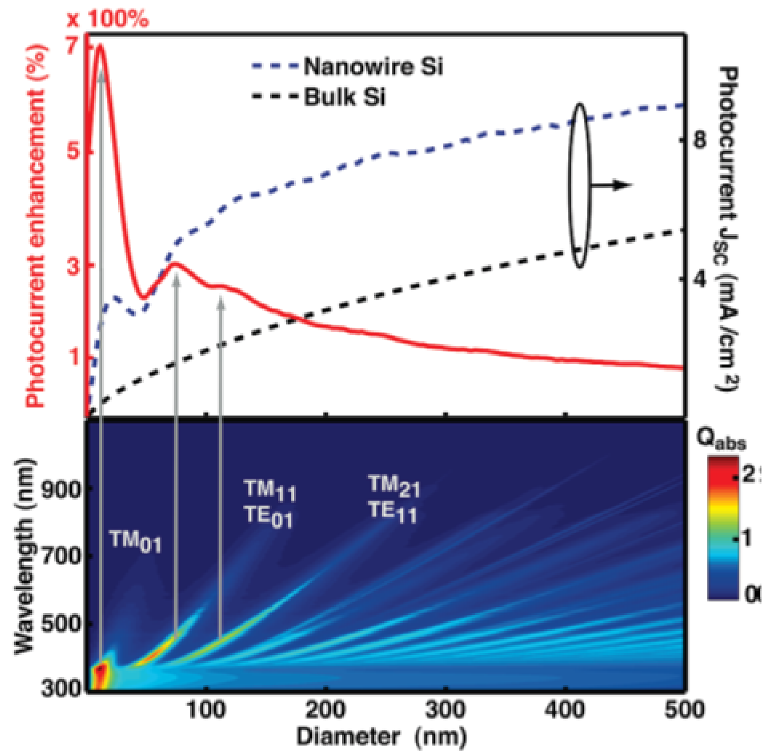

Figure 1.15: Two-dimensional plot of Q_{abs} of a SiNW as functions of the λ and diameter. The streaks illustrate the presence of leaky mode resonances [38].

wave-guide axis [39]. Fig. 1.18 illustrates the field distributions of zero order and some higher order modes in a planar-mirror wave-guide. For the case of the SiNWs (whereby the boundary of SiNW/Air is a not a perfect reflector) the modes are termed leaky due the electromagnetic field decaying monotonically for a finite distance in the transverse direction.

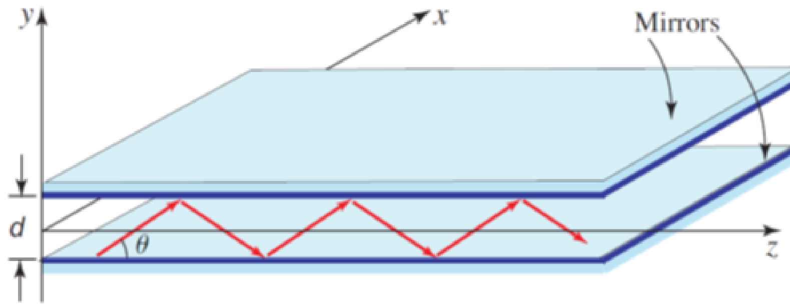

Figure 1.16: Guided optical ray in a planar-mirror wave-guide [39].

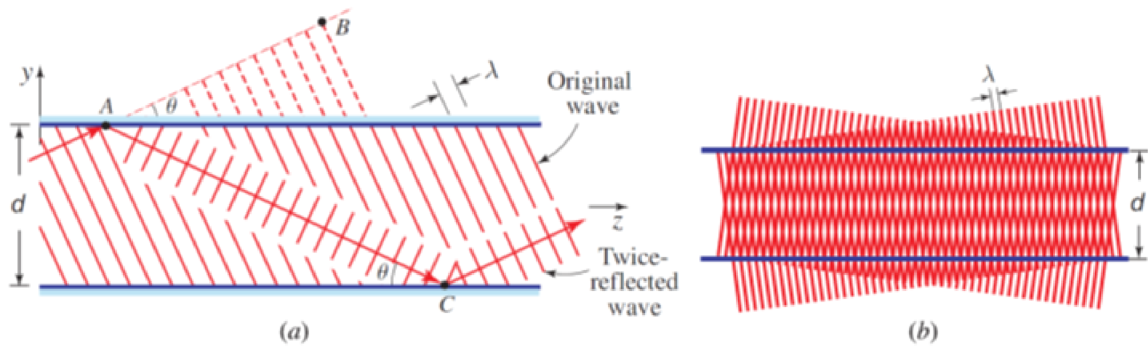

Figure 1.17: a) Condition of self-consistency, whereby a wave reflects twice and duplicates itself. (b) The two waves interfere and create a pattern that remains constant with z. This occurs only for angles for which self-consistency is satisfied [39].

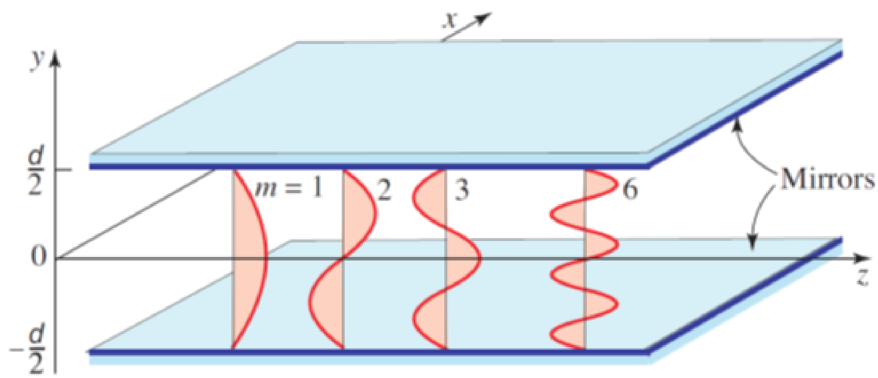

Figure 1.18: Field distributions of the modes of a planar-mirror wave-guide [39].

1.4 Nanowire Technologies

The use of NW in solar cell technology is a vast field, growing considerably in the last decade. This research has been driven due larger demands in solar cell efficiencies for lower prices meeting the progress achieved in nano-scale fabrication of high performing electronic devices. The benefits provided by nano-wire PV over planar devices (i.e. solely wafer based or thin-film technologies) is multidimensional, including carrier generation, separation and collection as well as production costs. The majority of these benefits are applicable when the PV device takes the form of an ordered array of radial junctions - see Fig. 1.19. Functioning NW photovoltaics have been fabricated using a wide variety of materials in both a top-down (i.e. etching material away from the top surface) and bottom up process (i.e. growth of material on top of a substrate) [40].

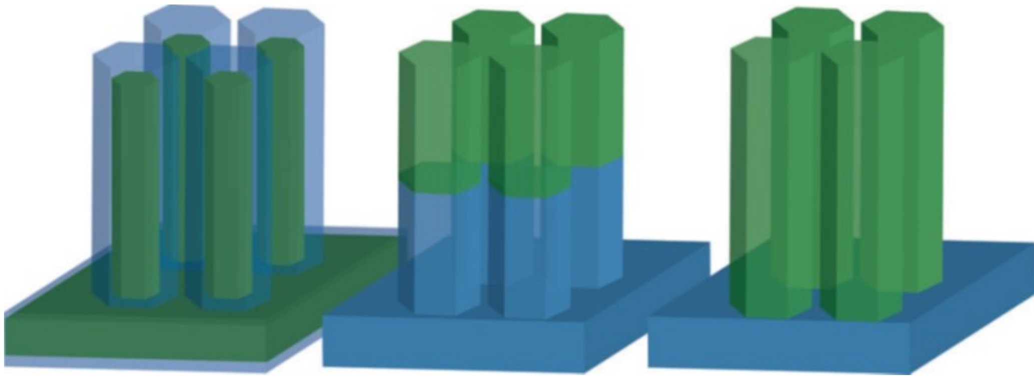

Figure 1.19: The junction types within a nanowire PV. The junction can be of radial, axial or a substrate junction. The former constitutes the most benefits as it provides an increase in junction area as well as the light trapping benefits of the other two [40].

Among various semiconductor nanowires, those made from III-V compound materials show potential as solar cells due to high absorption, direct band gap, superior carrier mobility, and well-developed synthesis techniques [41]. Mariani *et al.* report work on a GaAs NW solar cell with a radial p-n junction [42]. They are fabricated using a bottom up process of metal organic chemical vapour deposition (MOCVD). They produce a patterned architecture by utilising electron beam lithography techniques to precisely define radius and pitch in a mask from which the NWs can be grown. This controlled growth of NWs produced power conversion efficiencies (PCE) of 2.54%, an improvement from the 0.83% reported by LaPierre *et al.* [43]. The latter fabricated randomly distributed GaAs NWs

fabricated from Au-catalyzed vapor-liquid-solid (VLS) growth. Yao *et al.* report GaAs NWs which are also fabricated from a MOCVD process but form axial p-i-n junctions. Their results showed a significant increase of PCE to 7.58% which they attribute to better doping control over radial junctions [41]. Gao *et al.* fabricated NWs using InP using selective area growth inconjucntion with the MOCVD process. They fabricated axial junctions with an overall conversion efficiency of 1.51% [44]. Wallentin *et al.* report efficiencies up to 13.8% using arrays of InP NWs fabricated via epitaxial growth with an axially defined p-i-n doped structure. The arrays were patterned with nano-imprint lithography of gold seed articles [45], see Fig. 1.20. Their work illustrated that the NW diameter and length are critical for PV performance, with the best performance achieved by using resonant light trapping in 180 nm diameter NWs.

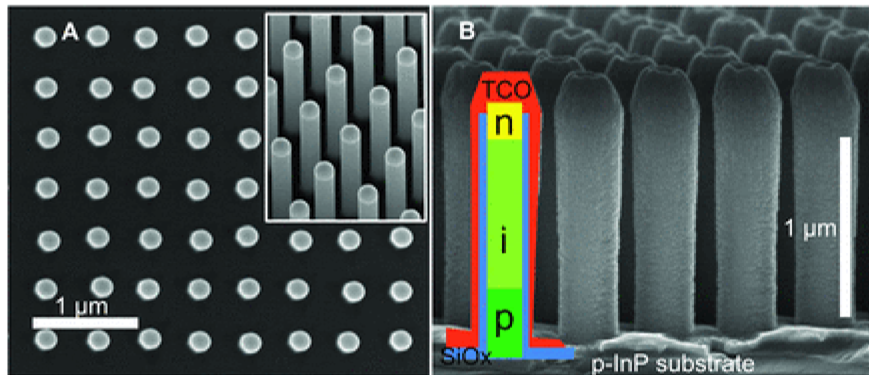

Figure 1.20: a) SEM image showing InP NWs fabricated via epitaxial growth with an axially defined p-i-n doped structure. The arrays were patterned with nano-imprint lithography of gold seed particles. b) Superimposed schematics showing the SiOx (blue), TCO (red), and the p-i-n doping layers in the NWs. [45]

NW solar cells fabricated with heterojunction structures have also become a growing research topic. Tak *et al.* report a ZnO/CdS solar cell with 3.53% efficiencies [46]. The core layer of ZnO NWs were fabricated via an ammonia solution process using a sputtered ZnO film. The outer shell layer of CdS is then made by immersing the ZnO NWs in alternating solutions of Cd and S ions, resulting in a layer-by-layer build up of the film. Williams *et al.* reports a heterojunction NW cell formed using CdTe as the core [47], see Fig. 1.21. The CdTe NWs are grown via Au-catalysed VLS growth, in which Mo substrates are initially coated with thin films of of CdTe. The outer shell is fabricated by sputtering CdS onto the NWA. The efficiency of the cell reached up to 2.49% through the

inclusion of a ZnO layer inbetween the outer shell of CdS and the ITO contact layer.

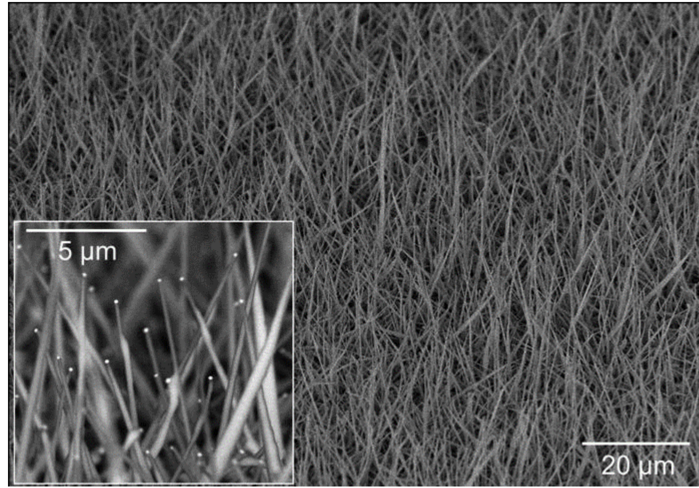

Figure 1.21: SEM image of CdTe NWs are grown via Au-catalysed VLS growth, in which Mo substrates are initially coated with thin films of of CdTe [47].

The implementation of NW technology on Si solar cells is also a promising research field. Stelzner *et al.* report Si NW solar cells fabricated using a chemical vapour deposition - vapour liquid solid (CVD-VLS) growth process [27]. This begins by flowing gaseous Si precursors such as silane or Si tetrachloride onto a substrate at high temperatures. A metal catalyst is used to form a liquid eutectic with the desired NW material. Chemical decomposition and dissolution into this droplet will lead to precipitation and eventually NW growth. Fabricating vertically aligned silicon NWAs that are dense and with a high aspect ratio can be achieved by this process using an appropriate substrate, precursor, temperature, catalyst and concentration [48]. The advantage of this process is that it provides good control over NW growth - density, diameter, length, as well as in situ doping [48]. This process however is vulnerable to metal contamination that can lead to degradation of minority carrier lifetimes and diffusion lengths in the SiNW due to deep level electronic states being induced in the Si bandgap [48]. Kendrick *et al.* report a SiNW solar cell fabricated via a VLS method with a Au catalyst showing efficiencies up to 2.3% [49], see Fig. 1.22. An important step in the fabrication process is a cleaning step of repeated thermal oxidation and oxide etching of the NWs. This process removes residual catalyst material. Using $POCl_3$ thermal diffusion, a p-n junction is fabricated with V_{oc} of 0.5 V [49].

As well as growth of NWs , a top down approach of fabricating nanostructures on

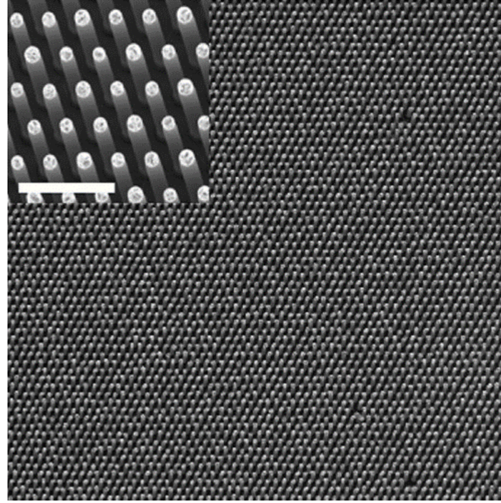

Figure 1.22: SEM image of an array of Si wires grown via a Vapour-Liquid-Solid method with Au catalyst. The scale bar represents 20 μm [49]

silicon is also a popular method - this includes reactive ion etching (RIE) [50–52], laser ablation [53–57] and metal assisted chemical etching (MACE) [48,58–63]. Hsu *et al.* report on the fabrication of a SiNWA using RIE with controlled diameter and pitch, ranging from 60 - 600 nm [50], see Fig. 1.23. The process for fabricating this involves first a deposition of a monolayer SiO_2 nanospeheres. The radius and pitch of these spheres are then tuned by selective isotropic RIE of SiO_2, in a plasma of O_2 and CHF_3. The SiNW is then etched via RIE using these spheres as a mask. Alongside diameter and pitch tuning, they also illustrated the ability to define vertical and tapered walls for the NW structure. Morton *et al.* utilised deep reactive ion etching (DRIE) to fabricate high aspect ratio SiNWA [51]. Nanoimprint lithography is used to produce the mask. They optimize the cycle times and gas flows to achieve vertical sidewalls with NW roughness less than 8 nm peak to peak, and aspect ratios greater than 60:1 [51]. Lu *et al.* presents a SiNWA solar cell fabricated via RIE producing efficiencies up to 10.8%. The mask used for etching utilises a self-powered parallel electron lithography technique whereby a large-area planar radioactive β-electron thin film emitter exposes e-beam resist through a stencil mask, resulting in sub-35-nm resolution. The SiNWA shows absorption up to 99% over wavelengths 400-1100 nm with a thickness of only 5 μm.

Laser ablation is also a prevalent research field in texturing Si with nanostructures. Lee *et al.* report a nano scale surface roughness that strongly enhances light-trapping

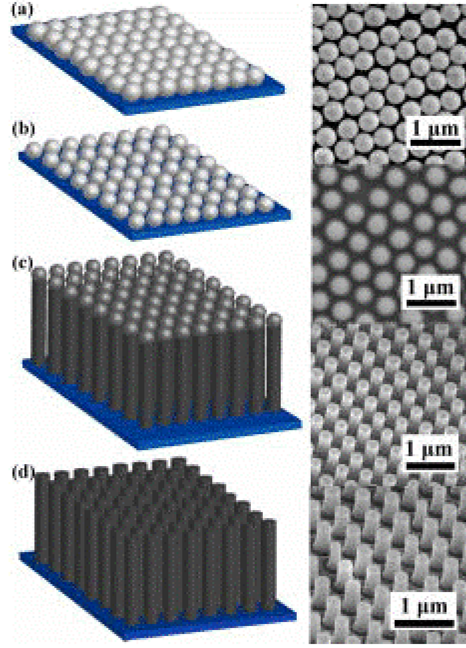

Figure 1.23: Fabrication process of SiNW. (a) Deposition of SiO_2 (b) Tuning mask by isotropic reactive ion (RIE) etching of SiO_2 . (c) Anisotropic etching of Si by RIE. (d) Removal of the residual SiO_2 by HF etching. [50]

in thin film c-Si solar cells [57]. They achieve this by scanning femtosecond laser pulses onto a Si surface under vacuum. The pulse locally melts Si at the surface, which rapidly resolidifies. Texturing in the morphology occurs due to interference effects, see Fig. 1.24. They found the enhancement of the optical absorption from light-trapping approaches the Yablonovitch limit [57]. Shen *et al.* report a high density array of nanoscale rods formed on Si surface using femtosecond laser irradiation with the substrate immersed in water. The formation of structures is due to interference of refracted and scattered light in the molten layer of Si and the increased cooling rate in the water [53].

MACE in particular is a popular NW preparation method for solar cell use, having produced vertically aligned SiNW that are uniform in terms of doping profile, crystal orientation, density, size, and shape [48]. This can be a two-step process which begins with nucleation via metal catalyst such as Ag or Au, and is followed by etching in an oxidizing HF solution [58, 59]. Due to the large surface-to-volume ratio of these NWs, the electrical properties will be heavily influenced by the surface states such as dangling bonds and defects. This sensitivity was tested by Zhang *et al.* who observed that the NWs had a larger current drive in air compared to vacuum [64]. The cause for this somewhat

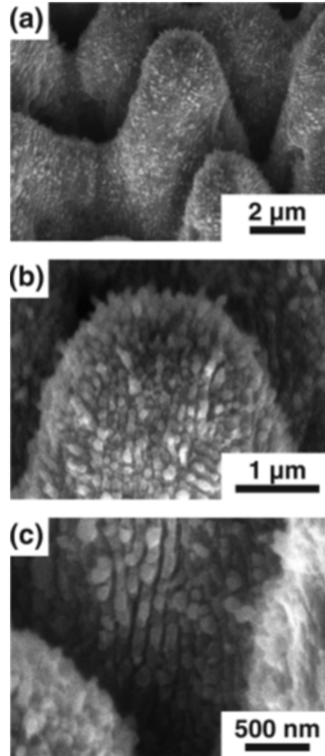

Figure 1.24: SEM picture of nanometer-scale rods formed via femtosecond laser pulses onto a Si substrate. (a) Low-magnification image (b) Top of spikes (c) In-between spikes. [57]

surprising outcome was identified as chemisorption of oxygen and humidity in the air. To elucidate this they passivated the surface of the SiNW, with 250 nm thick SiO_2 and found improved performance in carrier transport [64]. As an alternative to this insulating and hydrophilic surface, a hydrophobic passivated surface can be formed by dipping the SiNWA in HF to form hydrogen terminating bonds [65]. The SiNWA fabricated from the MACE process have shown to exhibit good optical properties for PV applications. Peng *et al.* observed that the SiNWA significantly suppressed light reflection for wide spectral bandwidth, $< 1.4\%$ for 300 - 600 nm range [48], see Fig. 1.25. These arrays are able to trap light, since it scatters between the dense SiNWs, causing it to travel longer than the array thickness. The optical properties of SiNWA were further improved by Kelzenberg *et al.* through the introduction of an anti-reflection layer of SiNx and nanoparticles to induce light scattering [66]. As the MACE process uses AgNPs, there is potential to use these to further improve the optical properties of the SiNWA. It has been shown that AgNPs can influence the performance of Si solar cells due to local surface plasmon

excitation [67, 68]. One of the drawbacks of this fabrication process is that the NWs have shown to conglomerate at the tips to reduce surface tension [60]. The bunching occurs as MACE is a water-based etching process, so the NWs agglomerate in order reduce surface tension. Li *et al.* reported on some ways to reduce bunching, including adding ethanol during the etching process, applying freeze drying and also post-RIE treatment [69].

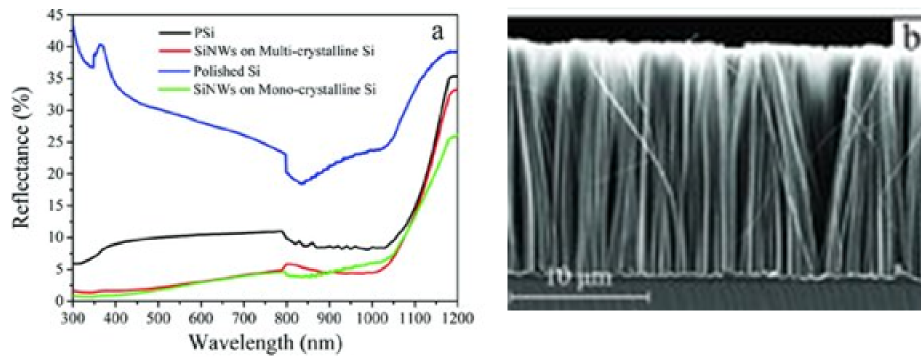

Figure 1.25: a) Reflectance measurements of SiNWA, porous Si (PSi), and polished c-Si. b) Cross-sectional SEM image of SiNWA by metal assisted chemical etching [48].

1.5 Aims and Organisation of Thesis

In this work, the focus is on the material Si. The current PV market is dominated by c-Si which has in excess of 80% market share [70]. This can be attributed to numerous factors:

- Semi-conductive material with a high minority carrier lifetime and diffusion length.
- Abundance of this material, with enough availability to meet even the most demanding production needs for extreme energy scenarios.
- Due to its non-toxicity there is more ethical freedom in its product life and recycling.
- Stability of this material has produced reliable solar modules lasting into decades.

1.5.1 Project Aims

The brief background on solar cell operation identifies the need to attain high absorption (i.e. generate a large current) and minimise recombination (i.e. operate at a large working voltage) in order to increase efficiencies. In this study the aim is to utilise a combination of SiNWAs and pyramids as a light trapping mechanism to increase the amount of carriers

generated. The proposed structures are Silicon Nanowires on a high density Pyramid array. In order to achieve successful use of these for a solar cell the following research questions need to be solved.

First Silicon Nanowire fabrication processes: The fabrication of the SiNWs has to be optimised to improve control, uniformity, yield and develop a repeatable recipe to achieve sub-micron length NWs. A sub-micron NW length is required for light absorption to occur as close to the junction as possible for optimal carrier collection. Furthermore, the fabrication must be cost-effective and mass producible.

Second Hybrid pyramid-nanowire fabrication: To increase the junction area further and increase light trapping, hybrid silicon NW-pyramid arrays are developed requiring micrometer size control of pyramids based on well established processing techniques in the photovoltaic industry and NWA definition within the pyramid structure.

Third Modelling: In order to optimise the design of the hybrid texturing an appropriate modelling tool needs to be developed that can cope with both optically and electrically complex structures. This required the development of a flow tool to connect two commercial TCAD packages specialised in optics and electronics respectively.

1.5.2 Organisation of Thesis

The remainder of this thesis consists of 6 more chapters and is organised as follows:

Chapter 2 gives an overview on the technology computer aided design package Sentaurus. It focuses on structure formation using the SProcess tool (used for emulating cleanroom fabrication steps), and electrical modelling using the SDevice tool. The tools are used to study the impact of doping profiles on SiNWA solar cell efficiency.

Chapter 3 focuses on the optical modelling using the commercial package Lumerical, providing an overview of the finite difference time domain method for solving Maxwell's equations. The tool is used to study the optical performance of SiNWAs. Furthermore, a new tool flow is developed to integrate the optical results into TCAD Sentaurus to perform electro-optical modelling of SiNWA and Pyramid-SiNWA hybrid devices.

Chapter 4 discusses the fabrication process for making SiNWA. The chapter focuses on the optimisation of a metal assisted chemical etch process to fabricate sub-micron length NWs. Measurements of optical performance as well as surface morphology are shown. Optoelectronic modelling for the fabricated structures is also presented.

Chapter 5 provides an overview of crystallographic etching of pyramids onto Si. It discusses the recipe for both a coarse and dense array of pyramids using a combination photolithography and wet etching processes. Measurements of optical performance as well as surface morphology are shown. Optoelectronic modelling for the fabricated structures is also presented.

Chapter 6 presents the fabrication of a hybrid structure which incorporates SiNWA onto a dense array of Pyramids. The fabrication process is discussed and measurements of optical performance as well as surface morphology is shown. The impact of surface recombination on solar cell performance of these high surface area structures is also studied using optoelectronic modelling.

Chapter 7 is the concluding chapter which summarises the results of the thesis and discusses how to implement the work produced in this project for future research. This includes the development of Ohmic contacts for complete solar cell device fabrication, as well as implementing the light trapping structures in hetero-junction devices by incorporating emerging materials of metal sulphide nanoparticles and perovskites.

2 TCAD

The semiconductor industry is a multi-billion pound commerce of which computer aided design plays a crucial role. At the device engineering stage Technology Computer Aided Design (TCAD) is prevalent. It helps engineers optimize *process* flows and the *device* characteristics prior to fabrication. TCAD can predict the electrical, optical, thermal and mechanical properties under set operating conditions given the data is properly calibrated. At the level above device engineering is circuit design. At this stage Integrated Circuit Computer Aided Design (IC-CAD) is prevalent. The integrated circuits are built from the devices designed by process flow/device engineering, and utilised as building blocks for system engineering. Unlike IC-CAD, TCAD is purely physics based - using fundamental physical models such as drift-diffusion and Poisson equations to simulate the behaviour of devices.

TCAD packages consist of several tools, however the common four are: a graphical user interface (GUI), a process simulator, a device simulator and finally a plotting tool. Numerous TCAD packages exist including Synopsys, Silvaco, Crosslight and Cogenda. The dominant package in the TCAD field is Synopsys, which is employed by 19 of the 20 leading semiconductor manufacturers [71]. It is also used extensively in the research field of semiconductor devices, most notably field effect transistors [72–76] and photovoltaics [77–84]. As such, it is used for this project. The four key tools used are Sentaurus Workbench, SProcess, SDevice and SVisual.

2.1 SProcess

SProcess models the various fabrication steps involved in semiconductor processing such as material deposition, diffusion and etching, using various meshing strategies to generate

a mixed grid element mesh [85]. This is advantageous as 3D structures can be formed from material growth and etching rather than explicit geometry definition. This allows a means of forming complex 3D structures through lithography steps followed by impurity diffusion as a function of time and temperature - key processing steps that are common to PV fabrication [86].

2.1.1 Diffuse

The diffuse command is central to SProcess as it models impurity diffusion during thermal processing in both inert and oxidizing environments. The general formulation [85] used for the particle current, J, of a diffusing species A is given by:

$$J_A = -d_A(\frac{n}{n_i}) \bigtriangledown (A(\frac{n}{n_i})) \tag{2.1}$$

where A is the concentration, d_A is the diffusivity, n is the electron concentration, and n_i is the intrinsic electron concentration.

The continuity equation for species A is given by:

$$\frac{\partial A}{\partial t} = - \bigtriangledown \cdot J_A + R_A^{trans} - R_A^{clus} \tag{2.2}$$

where R_A^{trans} and R_A^{clus} are contributions from transport models and cluster reactions. A vast amount of transport models are utilised by SProcess. These are used to compute particle flux of impurities given its interactions with space charge and lattice point defects (e.g. interstitials and vacancies). The latter refers to dopant-defect pairs whereby impurities require point-defects as a diffusing vehicle as they cannot transport themselves [85]. Alongside such pairing reactions, there also exists reactions involving the formation of impurity clusters, whereby dopants react with several interstitials or vacancies.

For the case of charge neutral impurities, the diffusion is simply based on Fick's first and second law.

$$J = -D\frac{\partial A}{\partial x} \tag{2.3}$$

$$\frac{\partial A}{\partial t} = D\frac{\partial^2 A}{\partial x^2} \tag{2.4}$$

where J is the diffusion flux, D is the diffusion coefficient, A is the concentration of

impurities, x is the position, t is time.

This postulates that impurities will diffuse from regions of high concentration to regions of low concentration, with a magnitude that is proportional to the concentration gradient. Furthermore, the diffusion causes the concentration to change with time.

The *diffuse* command is used to set the diffusion parameters of which the basic two are time and temperature. Ramp rates and wet/dry/ambient conditions can also be set. In order to see the doping within the structure, we plot the net active concentration against depth, see Fig. 2.1. This figure, which illustrates the doping concentration for different diffusion times at a temperature of 900°C and 1000°C , indicates how deep the junction forms within the device by observing the point at which the injected dopants match the substrate doping. When processing, we need to ensure the junction is deep enough away from the surface to reduce surface recombination whilst still close enough to be within the absorption depth of the illumination.

2.1.2 Deposit

SProcess simulates the deposition of materials, both within its database and newly defined ones, in several different forms. The three key deposition methods utilised in this project are 'anisotropic', 'isotropic' and 'fill'. Depositing materials requires geometric algorithms that are provided through the Sentuarus MGOALS package. The algorithms are vast and complex, however they can be summarised as follows:

1. Identify the original exposed top surface. This accounts for masks, non-etched layers, and user-defined structures which restrict visibility.

2. If the surface is flat, then the task is trivial and a translation of the surface upwards occurs for the desired thickness. However, if during the surface scan it finds adjacent mesh points not on the same line but with an angle difference, then it proceeds to form vectors which are normal to the two connecting lines. Furthermore, an arc of mesh points are formed to join the vectors. This results in a top surface that is smoother than its original.

The above describes very simple cases. In general, SProcess solves the time-independent boundary-value formulation of the Hamilton-Jacobi equation to compute the new bound-

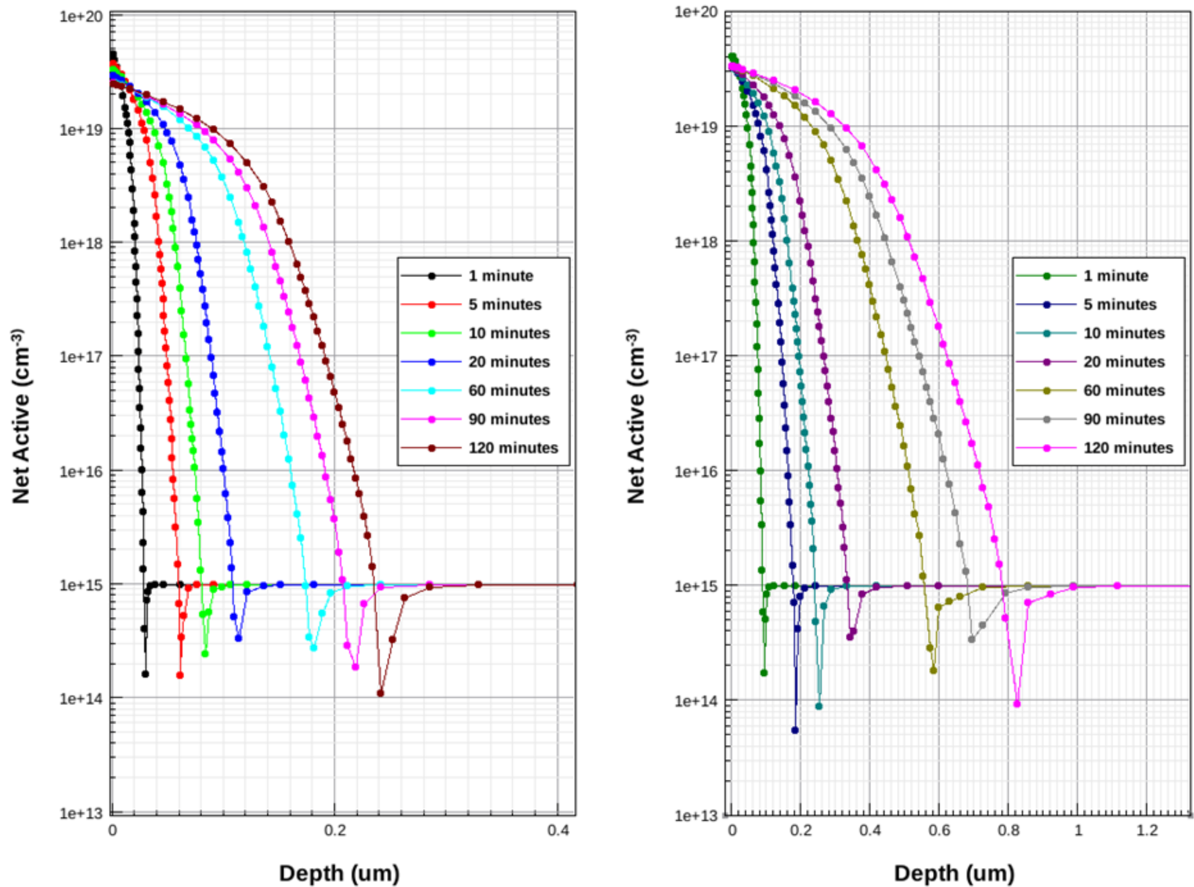

Figure 2.1: Doping concentration for different diffusion times at a temperature of $900°C$ and $1000°C$. The substrate has doping concentration of $1 \times 10^{15} cm^{-3}$ It can be seen that the increase in temperature significantly shifts the junction depths (i.e the point at which the dopants matches the substrate doping of 1e15 cm^{-3}).

ary locations. This has the ability to identify and rectify colliding mesh points.

The command for deposition is *deposit* and can be defined using 3 key parameters: type, thickness, and material. The deposition types used in this work are 'anisotropic', 'isotropic' and 'fill'. Fig 2.2 shows the results of the above commands applied to a silicon mesa. It can be seen that whilst isotropic depositions places material all around the mesa, anisotropic only adds on the normal surface. The 'fill' depositions places material within the whole volume up until the location specified in the command.

A very common deposition is that of photo-resist in order to simulate lithography steps. To implement this the command is *photo*. This implements the process of resist deposition, exposure under a mask, and development, thereby leaving a resist layer with vertical walls that is either the negative or positive of the mask depending on the command specified.

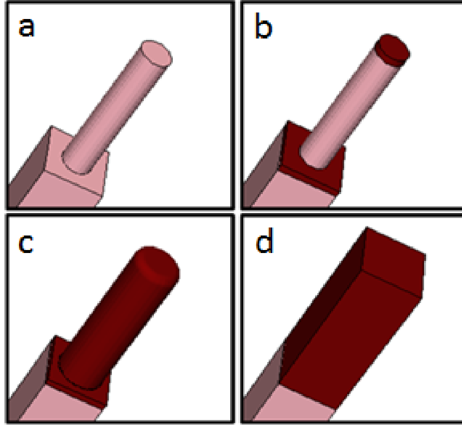

Figure 2.2: Example of deposition commands in SProcess whereby a layer of oxide material is deposited on a silicon nanowire represented as a cylinder on top of a cuboid. (a) without oxide, (b) anisotropic deposition, (c) isotropic deposition and (d) fill deposition.

The mask can be defined with geometric coordinates, drawn on ligament editor (part of the Sentaurus package) or else imported from common mask drawing tools (e.g. GDS files).

In order to implement roughness in the etched surface, resist roughness can be implemented. SProcess has a function entitled 'Line edge roughness' (LER) that is employed to the mask. This creates deviations to the ideal straight mask edges due to statistical fluctuations [85]. To randomise the deviation, a random noise function is generated using the Gaussian autocorrelation function:

$$Autocorrelation(f_{random}) = \Delta^2\sqrt{\pi}\Lambda^{-(\frac{x^2}{\Lambda^2})} \tag{2.5}$$

whereby Δ is the standard deviation, Λ is the correlation length, and x is the coordinate of the line edge. The roughness is incorporated by first dividing the mask edge into segments according to 'max.segment.length' parameter. Then a deviation, that is normal to the initial orientation, is added at each segment. Fig. 2.3 illustrates the etched surface roughness due to deviations in resist formation.

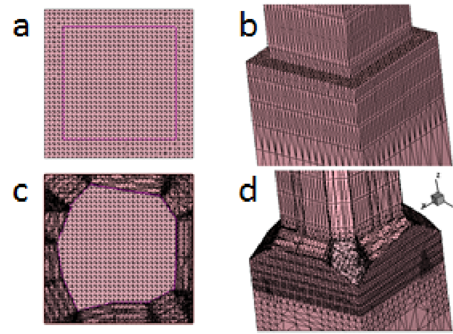

Figure 2.3: Illustration of the impact of LER on photo-resist deposition and etch. a) Top view of NW without LER b) 3D view of NW without LER c) Top view of NW after using LER d) 3D view of NW after using LER.

2.1.3 Etch

Although SProcess offers a variety of different etch processes, the 3 used in the project are anisotropic, isotropic and crystallographic etch. Anisotropic etching is used to remove material vertically downwards whilst isotropic etching removes material in all directions. The former is particularly useful when working with masked layers. As anisotropic etching results in vertical walls, it can often be sensitive to numeric round-off error. A common means to tackle this problem is to apply an over etch to prevent thin regions remaining. Crystallographic etching, whereby silicon can be etched along its crystal planes, can also be simulated in SProcess. The etch rates for the crystallographic planes can be defined by the Miller indices. There also exists a simple means to remove material in its entirety as long as there exists some exposure to the top surface. The command for this is *strip* and its only parameter is the target material, which is most commonly resist. This is useful for implementing lift off steps.

2.1.4 Mesh Generation

Throughout the processing stage, and in preparation for the electrical solve, the Sentaurus package implements various meshing strategies to maintain a balance between accuracy of results and simulation time. The tool produces finite-element meshes which spatially discretesize structures using a Delaunay mesh generator which produces triangles in 2D and tetrahedra in 3D. Delaunay triangulation for a set of P points in a plane is a triangulation DT(P) such that no point in P is inside the circumcircle of any triangle in DT(P) [87]. This

algorithm maximises the minimum angle for all triangles, producing a smoother mesh, and is named after Boris Delaunay. Fig 2.4 illustrates the difference between Delaunay and non-Delaunay triangulation.

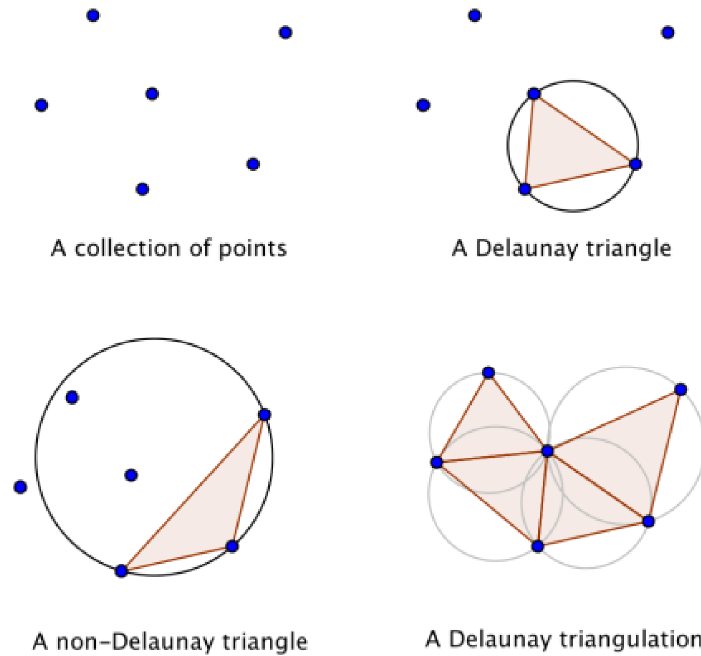

Figure 2.4: Comparison of Delaunay and non-Delaunay triangulation. It can be seen that no points are within any circumcircle for the Delaunay case. [88]

Meshing is defined by first stating a refinement window. This can encapsulate an entire region or material type, a defined cuboid, or a more intricate means of extruded mask data. Minimum and maximum element size for the mesh grid is then defined. This will put limits as to how small and how big each element within a window can be, depending on the refinement functions. This will determine the exact size of the elements in the mesh grid. Using the doping profiles of the device is a good guide in ensuring the mesh is refined appropriately. Furthermore, any interfaces between different materials are places where a fine mesh is required because relevant parameters such as doping, electric field and electrostatic potential show large variation in this region. Fig 2.5 illustrates the meshing between material interfaces.

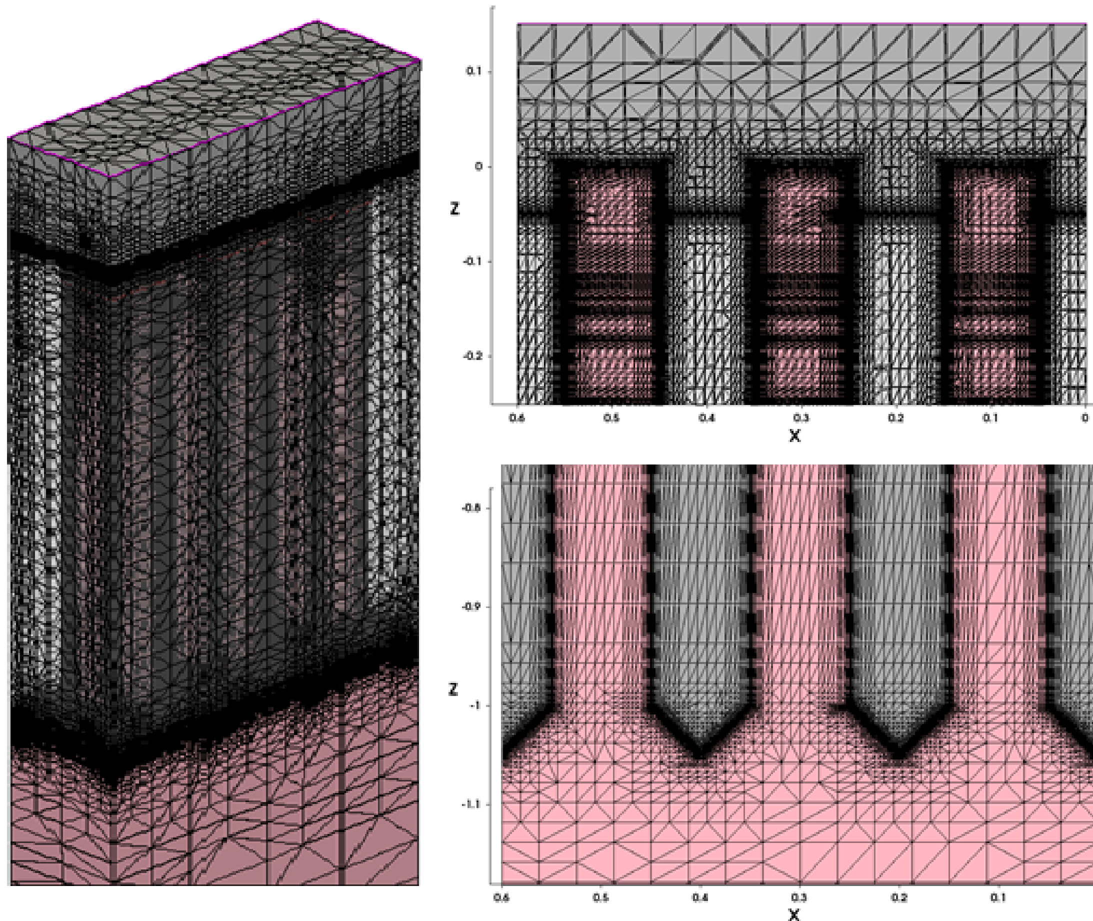

Figure 2.5: An example of mesh refinement at an interface of two materials. The mesh density is finest at the interface and coarser as it moves away into the bulk.

2.2 SDevice

SDevice simulates the electrical behaviour in a semiconductor device that is represented as a mesh grid file [89]. For PV devices, the input grid file should contain the geometry of the structure, the doping profile and optical generation profile. Differential equations describing the electric potential and carrier distributions are applied to each element of the mesh, with boundary conditions (i.e. potentials) provided at each electrode. The equations are then solved to find the potential and carrier concentrations in each element. The software uses a numerical solver which iterates repeatedly until a solution converges to a given accuracy. SDevice is purely scripted and the generic layout is as follows:

File This section is where the input and output files are defined. An example code listing is in shown listing 2.1. The grid file is an essential input file which is produced by

SProcess. It contains the critical data for defining the structure including mesh, materials, doping profiles and contacts. The optical generation input file contains the carrier generation data either from a previous simulation or from an external software package (discussed further in the chapter 3). The plot file contains all the output spacial data that has been solved by SDevice. The current file outputs all the electrical data such as IV characteristics. The output file is a simple log file. Finally the parameter file is used to read properties of newly defined materials or overwrite current properties within the database.

Listing 2.1: Script defining input and output files.

```
1 File {
2 Grid= "sprocess.tdr"
3 OpticalGenerationInput = "OGI.tdr"
4 Plot= "plot_data.tdr"
5 Current = "IV.plt"
6 Output = "log_file"
7 Parameter= "@parameter@"
8 }
```

Electrode This section defines the electrodes by setting the initial boundary conditions (i.e. bias) on the contacts. These can be either Ohmic or Schottky, with a specified potential barrier. An example code is shown in listing 2.2:

Listing 2.2: Script defining electrode names and initial bias.

```
1 Electrode{
2 { Name="Top Contact" Voltage=0.0 }
3 { Name="Bottom Contact" Voltage=0.0}
4 }
```

Physics When simulating a semiconductor device, there are a vast amount of physical models to consider and as such SDevice has a comprehensive database to pick from. They are stated and defined in this section. For PV devices, the models of particular significance are mobility, recombination, traps and optics. In most cases, the doping dependent mobility model is applied which takes into account degradation due to impurity scattering in doped materials. In addition to this, surface phonon and surface

roughness is also accounted for by considering mobility degradation at interfaces. For recombination, Shockley-Read-Hall (SRH) and radiative Auger recombination are accounted for. Traps are discussed later on in this chapter whilst optics models are discussed in chapter 3. An example code for this section is in listing 2.3:

Listing 2.3: Script defining a set of global physics models for recombination, mobility and bandgap for all materials.

```
1 Physics {
2   Recombination(   SRH   Auger   Radiative   SurfaceSRH     )
3   Mobility( DopingDependence HighFieldSat Enormal  )
4   EffectiveIntrinsicDensity(  BandGapNarrowing (delAlamo) )
5 } * end physics
```

Plot This section specifies all of the solution variables that are saved in the plot file. An example code for this section is shown in listing 2.4.

Listing 2.4: Script defining the various data to be saved during a simulation

```
1 Plot {
2 Doping BandGap eDensity hDensity ElectricField/Vector
3 Potential SpaceCharge Current/Vector eMobility hMobility
4 SRHRecombination OpticalGeneration eTrappedCharge hTrappedCharge
5 }
```

Math This section defines the method by which the device equations are solved, such that a solution converges to an acceptable error level. In most cases, an iterative linear solver (ILS) is used. This approach reduces the memory requirements and thus is the preferred solver for all 3D TCAD simulations. This method is also designed for parallel processing and the number of threads to use can be specified. An example code is shown in listing 2.5:

Listing 2.5: Script defining iterative process used for solving equations and the utilisation of processors

```
1 Math {
2 Number_of_Threads=30
3 Method= ILS
4 }
```

Solve In this section, the bias conditions are set. An initial basic solve of the Poisson equation occurs to solve the device under the steady state bias specified through the electrode statement. This is then followed by a quasistationary statement which ramps the bias voltage in a series of steps. The InitialStep, MinStep, and MaxStep parameters define the iterative procedure. An example code is shown in listing 2.6:

Listing 2.6: Script defining bias sweep of electrodes

```
1 Solve{
2 Poisson
3 Quasistationary(
4   InitialStep=0.01 MinStep=1e-5 MaxStep=0.2
5   Goal{ Name="TopContact Voltage= 1.0 }
6 ){ Coupled{ Poisson Electron Hole } }
7 }
```

2.2.1 Basic Equations

The key computation in the device simulation is to calculate the electrostatic potential determined by mobile (electrons and holes) and stationary charges (ionized dopants or traps). The simulator solves this using the Poisson equation

$$\varepsilon\nabla^2\phi = -q(p - n + N_D - N_A) - \rho_{trap} \tag{2.6}$$

where:

ε is the electrical permittivity.
ϕ is the electrostatic potential.
q is the elementary electronic charge.
n and p and are the electron and hole densities.
N_D is the concentration of ionized donors.
N_A is the concentration of ionized acceptors.
ρ_{trap} is the charge density contributed by traps and fixed charges

Eq. 2.6 is coupled to the drift-diffusion transport equations

$$\nabla.\vec{J_n} = qR_{net} + q\frac{\partial n}{\partial t} \quad , \quad -\nabla.\vec{J_p} = qR_{net} + q\frac{\partial p}{\partial t} \tag{2.7}$$

where:

- $\vec{J_{n,p}}$ is the electron and hole current density
- R_{net} is the net recombination rate

2.2.2 Traps

One of the key physical quantities that can drastically affect the electrical performance of a NWA solar cell is the surface recombination as it scales with the surface area. As such, traps and surface recombination velocities are important physical quantities.

The SRH recombination is defined in TCAD as [89]:

$$R^{SRH} = \frac{np - n_i^2}{(n + n_1)\tau_p + (p + p_1)\tau_n} \tag{2.8}$$

where:

- $n_1 = n_i \mathrm{e}^{\frac{E_{trap}}{kT}}$
- $p_1 = p_i \mathrm{e}^{\frac{-E_{trap}}{kT}}$
- n_i is the intrinsic carrier concentration
- E_{trap} is the energy difference between the defect level and intrinsic level
- $\tau_{p,n} = \frac{1}{\sigma N_\tau \upsilon + \frac{S_{n,p}}{y}}$. This is the recombination lifetime which is evaluated by taking into account trap states (defined by trap density, N_τ, and trap capture cross section σ) and surface recombination velocity ($S_{n,p}$). As the distance from the surface, y, is reduced, the impact of the surface recombination velocity on the recombination lifetime is increased. The final parameter in the recombination lifetime is the thermal carrier velocity, υ.

In SDevice, two different types of interface traps exist, an acceptor (or eNeutral) trap and a donor (or hNeutral) trap. The former is uncharged when unoccupied and becomes negatively charged when capturing an electron, whilst the latter is uncharged when unoccupied and becomes positively charged when capturing a hole. Several options for trap density of states (DOS) exists in SDevice in order to define the trap energy distribution inside the semiconductor: single trap level, exponential, Gaussian and uniform. The latter is most commonly used, and represents a uniformly energy distributed trap inside E_g, defined by the energy reference point, EnergyMid and EnergySig parameters.

Alongside the trap concentration, given in $cm^{-2}eV^{-1}$, the trap cross-section also defines the effective trap time constant. This can be estimated as:

$$\tau_{trap} = \frac{1}{N_t v_{th} \sigma} \quad (2.9)$$

where:

- N_t is the trap level concentration
- v_{th} is the thermal velocity
- σ is the trap cross-section

An example code for traps is shown in listing 2.7:

Listing 2.7: Script defining uniformly distributed interface traps between Si and air

```
1 Physics (MaterialInterface="Silicon/Gas") {
2 Recombination(SurfaceSRH)
3 Traps (
4                 (hNeutral Uniform Conc= 1e11 EnergyMid= 0 EnergySig= 1
                    FromMidBandgap
5                   eXsection= 1e-14 hXsection= 1e-14)
6         )
7 }
```

2.3 Simulation of SiNWA

In the fabrication of p-n core-shell NW structures via doping diffusion, the goal is to prevent carrier inversion in the whole wire. In this work, we investigate the effects of various spin-on-doping (SOD) processes to convert the NWs into core-shell p-n junctions. This research was presented at the 2013 European Modelling Symposium [86].

2.3.1 Process Simulation

We first initiate a rectangular beam of dimensions 200 nm $\times$ 200 nm $\times$ 20 μm. The initial bulk concentration n_i is defined to be $5 \times 10^{15} cm^{-3}$ of P dopants. To activate the dopants without redistributing them within the device, a diffusion step with zero time is used.

The etch is performed by first masking the nanowire area (150 nm $\times$ 150 nm) using photoresist and then performing an anisotropic etch (2 μm deep) on the exposed area. We then incorporate a trapezoidal etch to form interface roughness between NWs and

remaining bulk Si material, analogous to that formed by the MACE[1] process used in our labs to fabricate the Si NWAs. This creates an etch at an angle of 45°. In order to model the roughness further, LER is employed to the mask.

Doping

To simulate the spin-on-dopant (SOD) process we first deposit a layer of B dopant (N_A), approx 300 nm in thickness with a conc. of $5 \times 10^{21} cm^{-3}$ and then implement a diffuse step. This consists of annealing the structure and an-isotropically etching the oxide. When processing, we need to ensure the junction is deep enough, away from the surface, to reduce surface recombination whilst still close enough to be within the absorption depth of the illumination. Furthermore, for SOD on NWAs, these simulations will help to attain diffusion times and temperatures to ensure the junction area is present within the wires.

Using the Sentaurus Workbench, whereby we can vary different parameters within the same code, we can run experiments to find the sensitivity of time, t, and temperature, T, on junction depth. Multiple simulations are undertaken in which temperature is varied between 850°C $< T <$ 950°C in steps of 5°C. For each T, the diffusion time, t, is varied between $0 < t < 120$ min in steps of 5 min. This leads to numerous doping profiles (>1000). The data is then processed on MATLAB to find the junction depth W (i.e. $N_A = n_i$), for any given temperature and time combination , which is illustrated as a surface plot in Fig. 2.6. This plot shows that annealing at 900°C allows for a smooth variation of W with t and thus allows precise control. Fig. 2.7 illustrates the doping profile of 4 NWs which have been annealed for different times. It is apparent that at 30 min the B dopants have compensated the original n-type doping throughout the wire.

2.3.2 Electrical Simulation

Once the structure is meshed, optical generation within the device is calculated[2]. For the simulations in this section, the Sentaurus Electromagnetic Waves solver is used. Once the optical results are calculated[3], an electrical solve is undertaken using SDevice. The

[1] This is a metal assisted chemical etch process. See chapter 4 for more details.

[2] The optical solve methods to simulate SiNWA and the simulated results are shown extensively in the next chapter

[3] An alternative and more accurate optical solver using Lumerical FDTD is utilised in the next chapter

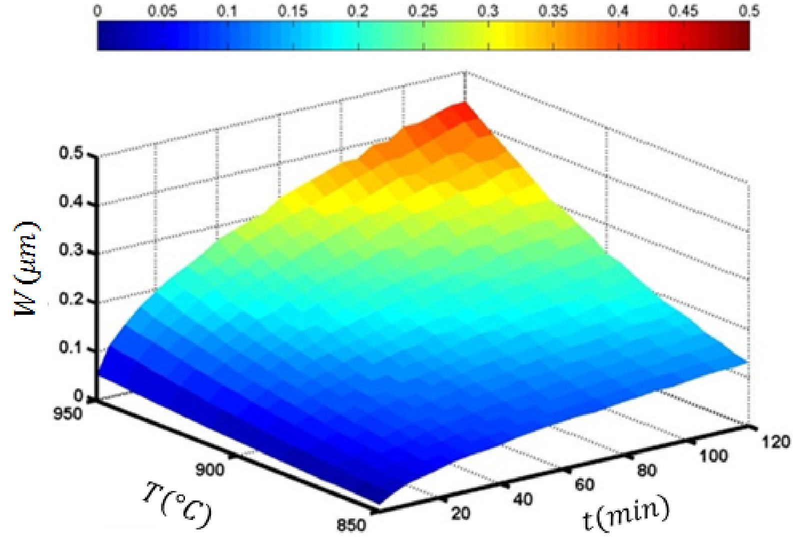

Figure 2.6: Surface plot of junction depth, W with varying anneal times, t, and temperature, T.

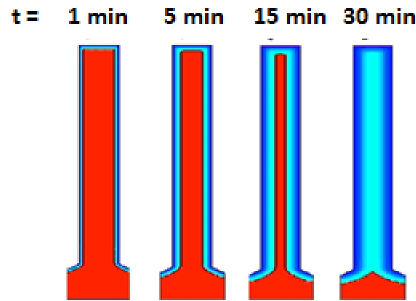

Figure 2.7: Thermally annealed N type NWs with B SOD at 900°C for different times, resulting in dopant inversion at t = 30 min. Red is P dopant and Blue is B dopant.

results for differing doping concentration, anneal time and temperature are given in figures 2.8-2.13 and are summarised as follows.

Effect of changing initial doping concentration

From Fig. 2.8 and Fig. 2.9, it is apparent that an increase in the initial B dopant concentration results in an increase in overall efficiency, η. The V_{OC} remains the same at 0.47 V, whilst the J_{SC} increased with doping concentration from 14.6 mA/cm^2 to 16 mA/cm^2. The highly doped NW provides both an increase in extraction of hole carriers to the contact as well as an increase in carrier collection due its junction area within the

wire.

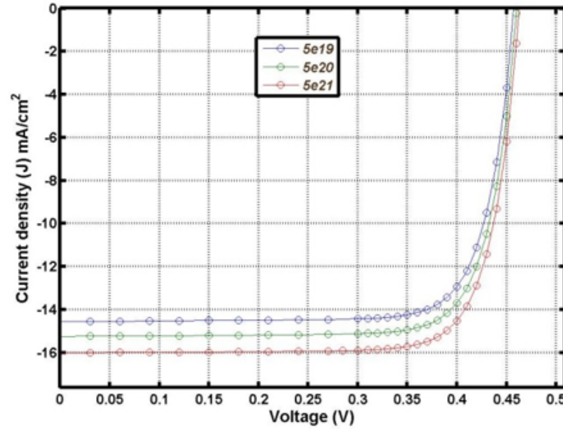

Figure 2.8: JV characteristics for varying initial B doping concentration, N_A, on an n-type NW with $n_i = 5{\times}10^{15}cm^{-3}$. The SOD process is undertaken at T = 900 and t= 1 min with $N_A = 5{\times}10^{19}cm^{-3}$, $5{\times}10^{20}cm^{-3}$, $5{\times}10^{21}cm^{-3}$

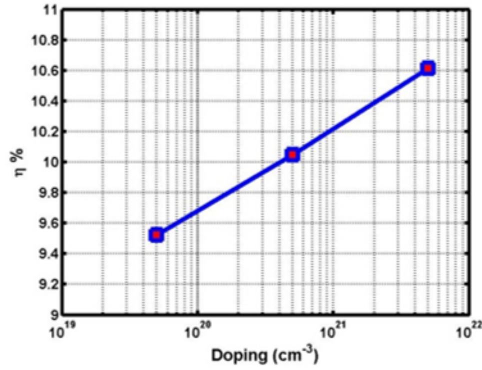

Figure 2.9: Efficiencies, η, for varying initial B doping concentration, N_A, on an n-type NW with $n_i = 5\ {\times}10^{15}cm^{-3}$. The SOD process is undertaken at T = 900 and t = 1 min with $N_A = 5\ {\times}10^{19}cm^{-3}$, $5{\times}10^{20}cm^{-3}$, $5{\times}10^{21}cm^{-3}$

Effect of changing annealing temperature

As shown in Fig. 2.10 and Fig. 2.11, an increase in temperature had negligible effect up to 950°C, after which it became detrimental to η. This suggests that the thinning of the core n-type material is resulting in reduced carrier extraction. V_{OC} = 0.47 V remained constant for all anneal, whilst J_{SC} had a value of 14.7 mA/cm^2 for all anneal temperatures up to 950°C. After this point, it drops to 13.8 mA/cm^2.

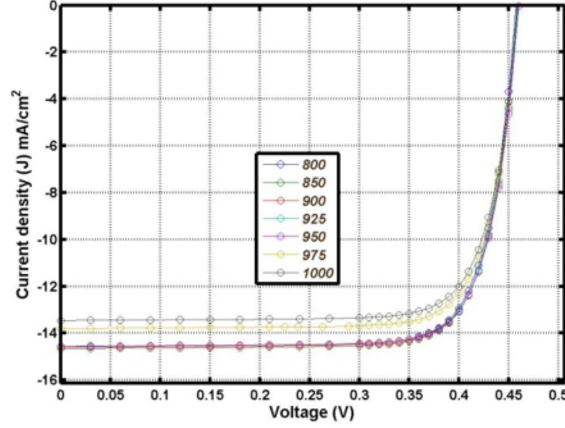

Figure 2.10: JV characteristics for varying anneal temperature, T, on an n-type NW with $n_i = 5 \times 10^{15} cm^{-3}$ and $N_A = 5 \times 10^{21} cm^{-3}$. The SOD process is undertaken for t= 1 min and 800°C<T<1000°C.

Effect of changing annealing time

Fig. 2.12 and Fig. 2.13 shows the largest drop in efficiency. This is due to reverse doping of the wire over time such that the junction is no longer within the wire but is now within the bulk silicon. The drop in efficiency is 1.3 percentage points. V_{OC} = 0.47 remained constant for all anneal time processes, whilst the J_{SC} reduced from 14.6 mA/cm^2 to 12.8 mA/cm^2.

2.3.3 Conclusion

In this chapter, n-type SiNWAs with B SOD to form p-n core-shell solar cells were simulated and studied by TCAD. It was shown that annealing at 900°C allows for a smooth variation of the junction depth with time and thus allows precise control. Optimised junction depth show that the core-shell p-n junction within the wire increases the efficiency by approximately 15%. Table 2.1 compares the result against experimental data observed [90]. The simulation results are in good qualitative agreement with the experimental measurements, with both showing some improvements in η for the radial junction. Whilst the trends are simillar, the absolute values in η differ greatly. This differential can be accounted for by the limitations in the simulation. The various losses through parasitic resistances were not taken into account, hence the similarity in J_{sc} and V_{oc}, but

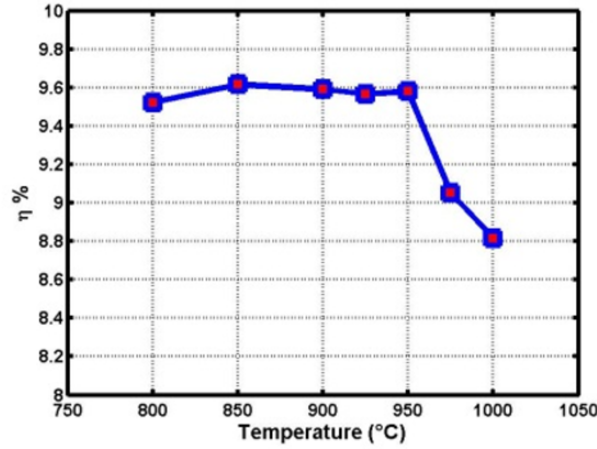

Figure 2.11: Efficiencies, η, for varying anneal temperature, T, on an n-type NW with n_i = 5 $\times 10^{15} cm^{-3}$ and N_A = $5\times10^{21} cm^{-3}$. The SOD process is undertaken for t= 1 min and 800°C<T<1000°C.

discrepancy in overall η.

Table 2.1: PV characteristics of modelled and experimental SiNWA. Experimental data taken from the paper by [90] and is shown in red.

	Planar Junction	Radial Junction
$J_{sc}(mA/cm_2)$	12.6 (9.34)	14.2 (14.42)
V_{oc}(V)	0.47 (0.548)	0.47 (0.485)
η(%)	8.6 (3.73)	9.9 (4.40)

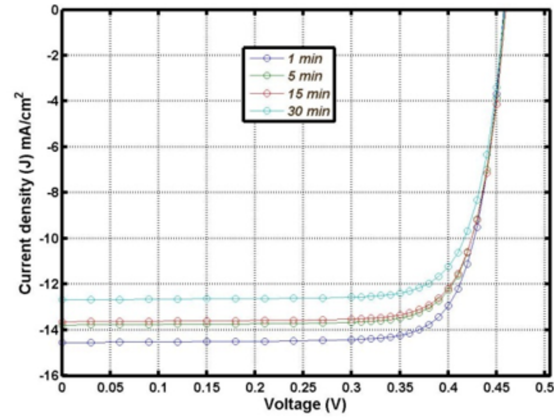

Figure 2.12: JV characteristics for varying anneal time, t, on an n-type NW with n_i = $5{\times}10^{15}cm^{-3}$ and N_A = $5{\times}10^{21}cm^{-3}$. The SOD process is undertaken for T = 900°C and 1 min < t < 30 min.

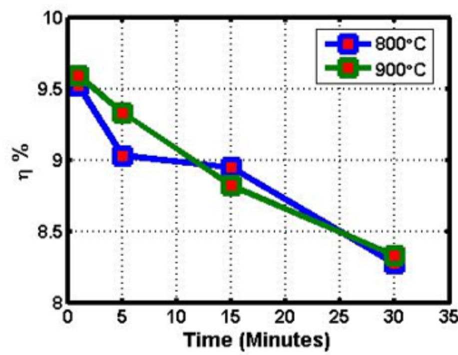

Figure 2.13: Efficiencies, η for varying anneal time, t, on an n-type NW with n_i = $5{\times}10^{15}cm^{-3}$ and N_A = 5 $\times10^{21}cm^{-3}$. The SOD process is undertaken for T = 800°C and 800°C with 1 min < t < 30 min.

3 Opto-Electronic Modelling

As shown in the previous chapter, TCAD tools help to simulate devices prior to processing in order to explore and optimize variables [83, 91–93]. This can lead to observable trends in performance which can be used to determine suitable designs before fabrication. The modelling of PV can be separated into three elements: processing, optical and electrical characteristics. Sentaurus TCAD is a comprehensive suite of modelling tools, and an industry standard for semiconductor processing and device simulation of complex geometry structures. However for optical modelling, Lumerical has more recently grown to an immensely popular finite difference time domain (FDTD) package, as shown by the number of papers (>100) published utilising this tool since 2010 [94]. Alongside commercial packages such as Lumerical, accurate open source FDTD solvers are also available in the field, including MEEP [95]. In this work, Lumerical is integrated with Sentaurus TCAD to establish an efficient and easy to use tool flow which will allow researchers to explore innovative 3D PV devices. Whilst both packages contain optical and electrical simulation tools, they offer optimum performance and versatility in one of the two tasks[1]. Current approaches to ameliorate this issue has involved utilising the Sentaurus structure editor to define new data fields within a device to write custom carrier generation data that have been calculated externally [96]. The process established in this work provides an alternative method by manipulating the optical generation data files formed using Sentaurus Device. Furthermore, the work here extends to 3D devices that can be designed using the Sentaurus SProcess tool. As such, the integration of both packages allows the user a powerful tool that provides the accuracy and efficiency needed for intricate nano-scale PV modelling.

[1]This is shown in section 3.2 of this chapter

3.1 Lumerical

For PV simulations, the modelling of light propagation through various media as well as scattering from interfaces is a crucial step and several approaches are available, each with a trade-off between computational load and accuracy. As PV technologies push further towards thin films and nanoscale structures, methods such as raytracing, which provide solutions based on geometric optics alone, are no longer applicable for accurate results when wavelengths are comparable to the feature size. Current approaches to compute nanoscale optics require solving Maxwells equations. A variety of methods exist to solve these equations, including Finite Difference Time Domain (FDTD) method, Finite Element Method (FEM), Transfer Matrix Method (TMM) and Rigorous Coupled-Wave Analysis (RCWA), to name a few. For PV simulation whereby the injected wave has broadband wavelength range, the FDTD method is most efficient. Lumerical, like many commercial optical solve packages, uses this method [94].

3.1.1 FDTD

The FDTD method solves Maxwell's equations in the time domain. In this approach, both space and time are segmented into discrete sectors. Space is divided into cuboid cells whereby the electric fields are located on the edges of the cell and the magnetic fields are found on the faces, see Fig. 3.1. Furthermore, time is discretized into small steps where each step represents the time required for the field to propagate between adjacent cells. A leapfrog scheme is used to update the electric and magnetic fields as a function of time. Through this method it can obtain complex-valued fields and normalised transmissions as a function of frequency. The FDTD algorithm was first proposed by Kane Yee in 1966 using the Yee cell, shown in Fig. 3.1. Developing the full set of three-dimensional equations is tedious and not within the scope of this project, however to understand the mechanism of this process, the one dimensional algorithm is as follows [97].

For a one-dimensional space varying in the x direction and assuming that the electric

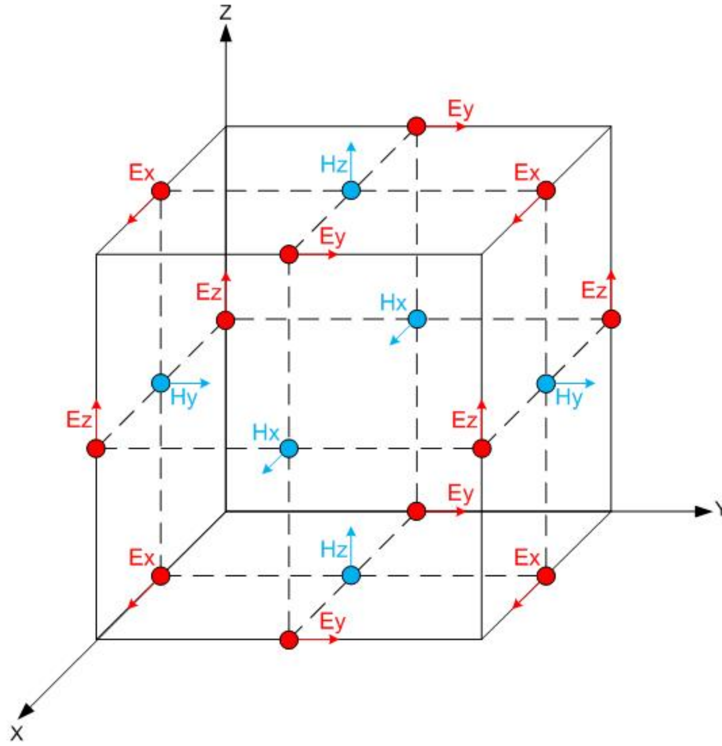

Figure 3.1: This figure illustrates the Yee cell used in the FDTD method [98]. It represents the discreticized electric and magnetic fields in a 3D domain.

field only has a z component, then using Faraday's law :

$$-\mu\frac{\partial H}{\partial t} = \nabla \times E = \begin{bmatrix} \hat{a}_x & \hat{a}_y & \hat{a}_z \\ \frac{\partial}{\partial x} & 0 & 0 \\ 0 & 0 & E_z \end{bmatrix} = -\hat{a}_y\frac{\partial E_z}{\partial x} \tag{3.1}$$

Thus, Ampere's law:

$$\epsilon\frac{\partial E}{\partial t} = \nabla \times H = \begin{bmatrix} \hat{a}_x & \hat{a}_y & \hat{a}_z \\ \frac{\partial}{\partial x} & 0 & 0 \\ 0 & H_y & 0 \end{bmatrix} = -\hat{a}_z\frac{\partial H_y}{\partial x} \tag{3.2}$$

This leads to two scalar equations, the temporal derivative of the magnetic field in terms of the spatial derivative of the electric field and vice versa:

$$\mu\frac{\partial H_y}{\partial t} = \frac{\partial E_z}{\partial x} \tag{3.3}$$

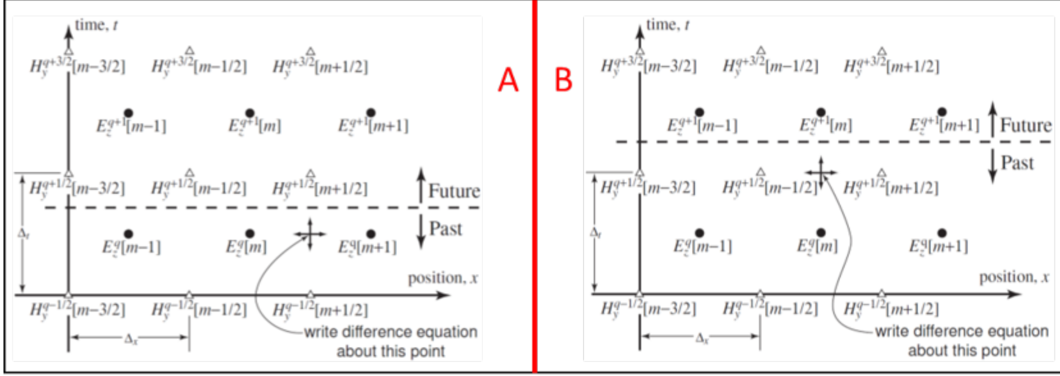

Figure 3.2: The sampling in space and time for the FDTD algorithm [97]. The dashed line represents the present point of the injected fields, and its traversing forward in time is shown between A and B.

$$\epsilon \frac{\partial E_z}{\partial t} = \frac{\partial H_y}{\partial x} \tag{3.4}$$

The next step is to replace the derivatives with finite differences. This can be achieved by sampling space and time as shown in Fig. 3.2. Δ_x is the spatial offset, Δ_t is the time offset, m is the spatial index, and q is the temporal index. This leads to following notation:

$$E_z(x,t) = E_z(m\Delta_x, q\Delta_t) = E_z^q[m] \tag{3.5}$$

$$H_y(x,t) = H_y(m\Delta_x, q\Delta_t) = H_y^q[m] \tag{3.6}$$

The aim of the FDTD algorithm is to transition from situation A to B in Fig. 3.2. Consider Faraday's law for the space-time point shown in part A of the figure.

$$\mu \frac{\partial H_y}{\partial t}|_{(m+\frac{1}{2})\Delta_x,\Delta_t} = \frac{\partial E_z}{\partial x}|_{(m+\frac{1}{2})\Delta_x,\Delta_t} \tag{3.7}$$

These derivatives are replaced by their finite differences, i.e $H_y^{q+\frac{1}{2}}[m+\frac{1}{2}]$ and $H_y^{q-\frac{1}{2}}[m+\frac{1}{2}]$ for the temporal derivatives and $E_z^q[m+1]$ and $E_z^q[m]$ for the spatial derivatives.

This yields:

$$\mu \frac{H_y^{q+\frac{1}{2}}[m+\frac{1}{2}] - H_y^{q-\frac{1}{2}}[m+\frac{1}{2}]}{\Delta_t} = \frac{E_z^q[m+1] - E_z^q[m]}{\Delta_x} \tag{3.8}$$

A simple rearrangment results in an updated equation for H_y:

$$H_y^{q+\frac{1}{2}}[m+\frac{1}{2}] = H_y^{q-\frac{1}{2}}[m+\frac{1}{2}] + \frac{\Delta_t}{\mu\Delta_x}(E_z^q[m+1] - E_z^q[m]) \tag{3.9}$$

This generic equation can be applied to any magnetic-field node as it shows H_y dependent on only its previous H field and adjacent E fields. Once all H_y nodes are solved above the dashed line in A of Fig. 3.2, the line can transition a half time step to scenario B. Applying Ampere's law to the space-time indicated in this scenario will result in a similar updated equation for the E_z field, as seen for H_y.

$$E_z^{q+1}[m] = E_z^q[m] + \frac{\Delta_t}{\epsilon\Delta_x}(H_y^{q+\frac{1}{2}}[m+\frac{1}{2}] - H_y^{q+\frac{1}{2}}[m-\frac{1}{2}]) \tag{3.10}$$

Likewise, the future value of E_z depends on only its past value and the value of the neighbouring magnetic fields. Once all E_z nodes are solved above the dashed line in B of Fig. 3.2, the line can transition a half time step to the next scenario, and so on. This inter-change between solving H_y and E_z illustrates the aforementioned leap frog method.

3.1.2 Tool

The key input parameters to consider for the simulation are the material properties, light sources, data monitors, boundary conditions and also meshing - see Fig. 3.3. When using dispersive media, as is the case for PV devices, a fitted model of multi-coefficients is used to represent tabulated refractive index (n,k) data.

Various types of sources exist to excite the structures within the simulation domain such as: Gaussian source, Total-field scattered-field (TFSF) and plane wave. The latter is used to model uniform electromagnetic fields with wavelength range (300 - 1000 nm) impinging from one side of the simulation domain.

Structures tend to have a periodicity and therefore the boundary conditions are periodic in the x and y direction, whilst the z direction have perfectly matched layers to absorb any reflected and transmitted fields. Furthermore, in many instances, the structure is also symmetric as well as periodic. Under these conditions we incorporate symmetric and antisymmetric boundaries to reduce computation time. Boundary conditions are required due to the dependency of the update equations on their surrounding fields. Therefore,

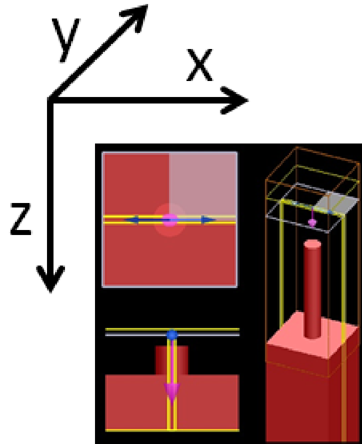

Figure 3.3: The simulation domain for a Lumerical optical solve. The nanowire is represented as a cylinder above a cuboid. The injected plane wave is shown by the grey plane, whereby the purple arrow is the direction of propagation and the blue arrow is the polarisation. The yellow planes illustrate the data monitors. A 2D cross section monitor is used to observe carrier generation within the wire. Also, 2D monitors are used above the injected wave and bottom of the substrate to measure reflectivity and transmission respectively.

at the edge of the Yee cell, there are field components missing - see Fig. 3.4. These situations are handled using boundary conditions. The two most common are Dirichlet and periodic, and a pseudo boundary condition known as perfectly matched layers (PML). The Dirichlet boundary conditions forces fields outside the grid to zero, and thus the boundary is assumed either a ”perfect electric conductor” or a ”perfect magnetic conductor”. Periodic boundary conditions force the fields on the left of the grid to be same fields as the far right side of the grid, and vice versa. The PML incorporates loss into the outer layers of the grid to absorb exiting waves. This prevents reflection, but it is not a true boundary condition as it has not defined the values at the edge of the Yee cell. Therefore, it is common to use Dirichlet boundary conditions alongside PML.

In addition to the boundary condition, the quality of the mesh will also affect the accuracy of results. The mesh is a Cartesian grid which represents the structure. For each mesh point, the material and geometrical information is stored and electric and magnetic fields are solved. As such, a trade-off exists between a fine mesh (i.e. a smaller minimum mesh length) and computation time. A meshing algorithm is applied by the solver to form a mesh as a function of the material refractive index and structure interface. Fig. 3.5 shows a variance of the reflection spectrum solved for a 50 nm diameter NW as a function

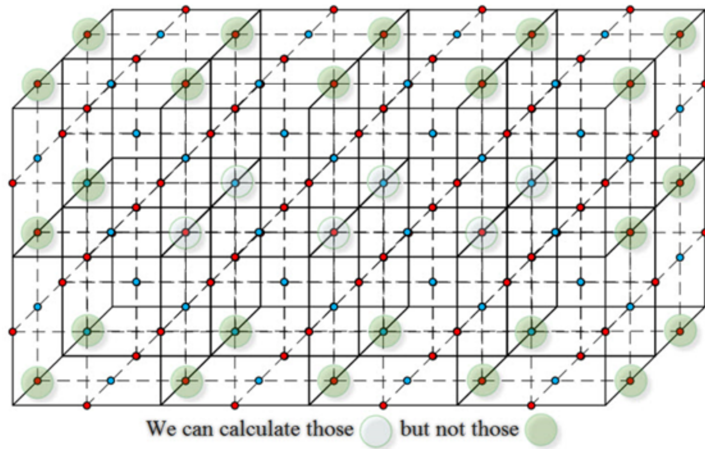

Figure 3.4: Missing field components at the edge of Yee Cell [98].

of mesh accuracy. The mesh accuracy varies from 1-8, whereby 1 is a coarse mesh with a minimum mesh size of 10 nm whilst 8 is a fine mesh with a minimum mesh size of 1.5 nm. The computation time is 90 s and 914 s using 2 × Intel Xeon E5-2680, respectively. We can see from the figure that at the coarse meshes, particularly at the smaller wavelength regions there is large error. This tends to smooth out as the mesh becomes finer. In this work, as a trade-off and to keep comparisons between structures consistent, a mesh accuracy with a minimum mesh length of 2.5 nm is used.

We also use a termination criteria of 1×10^{-5} , to ensure simulations end when the spectral response obtained by the Fourier transformation is valid. We measure the reflection (R) data from a monitor placed at the top of our simulation domain. Since a semi-infinite lossy Si substrate is modelled, absorption is $A = 1 - R$. A power absorption (P_{abs}) monitor is used to automatically map a spatial absorption profile by recording the electric field (E) intensity and imaginary part of the permittivity (ε) [94]. This is proportional to the carrier generation (G) by using the following relations:

$$P_{abs} = -0.5\omega|E|^2 imag(\varepsilon) \tag{3.11}$$

$$G = \frac{P_{abs}}{\hbar\omega} \tag{3.12}$$

with $\hbar$ is the reduced Planck's constant and ω is the angular frequency.

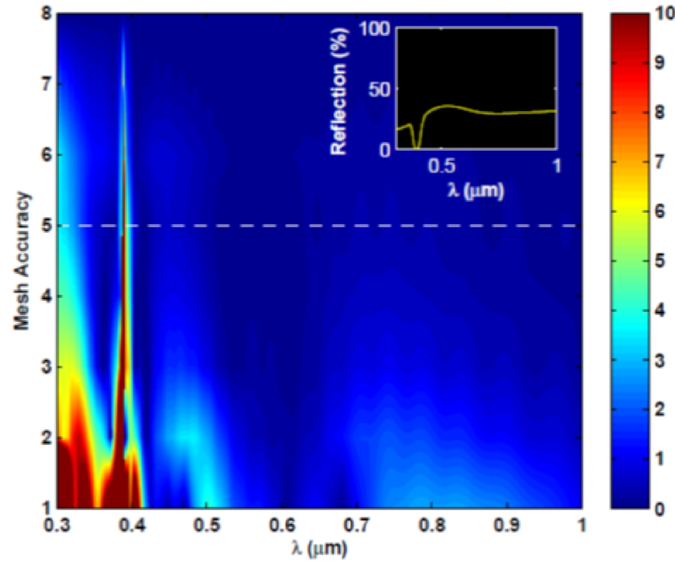

Figure 3.5: Variation in reflection spectrum as a function of mesh accuracy. The dashed line represents the accuracy level at which reflection measurements become relatively consistent with increasing accuracy thereafter. The inset illustrates the reflectivity under high accuracy. It can be seen that around wavelength at which resonant modes would occur (i.e. very low reflectivity) the influence of mesh accuracy is more significant.

3.2 Comparison of Lumerical and Sentaurus

Both Lumerical and Sentaurus provide tools for structure generation, optical modelling and electrical modelling. However, integrating the two removes the bottlenecks of each package and utilises their advantages. The content of this section was published in [99].

Structure generation

Whilst Lumerical has a comprehensive library of structures from which to build the device, it lacks the freedom and versatility to define unique designs based on material processing chemistry. This is of particular importance in PV as complex 3D doping profiles can be modelled rather than pre-defined. The ability of Sentaurus to replicate fabrication processes using elaborate meshing strategies, is based upon decades of experience in modelling semiconductor devices [100].

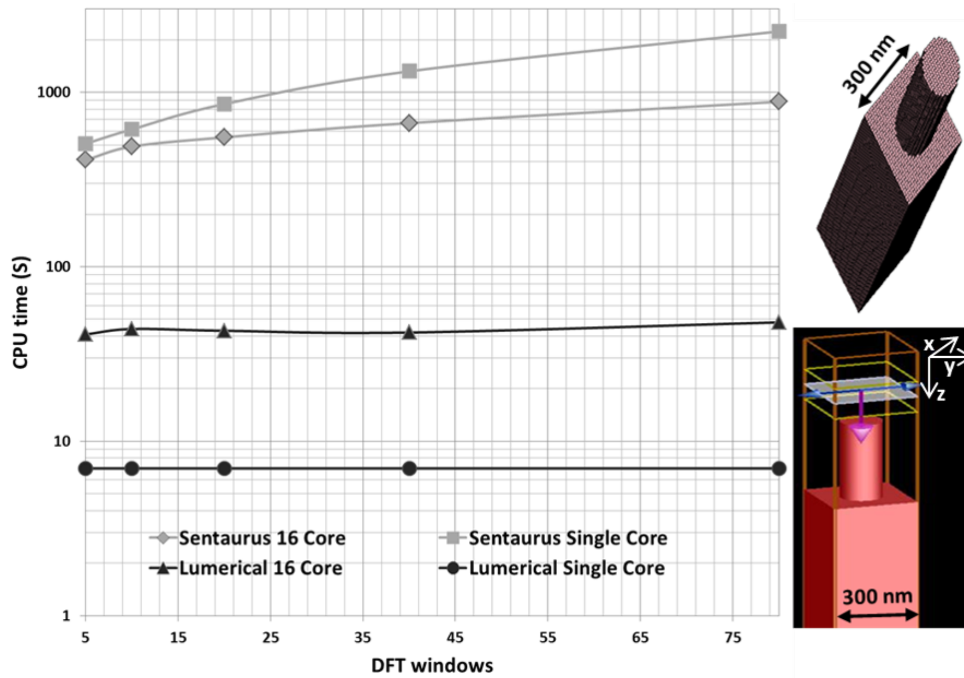

Figure 3.6: Comparison of simulation times using multi-core and single-core for Lumerical and Sentaurus Packages. The simulation is of a basic periodic SiNWA formed from a cylinder and a cuboid. The NW has a radius of 75 nm and a height of 500 nm, whilst the bulk region has dimension of 300 nm × 300 nm × 1 μ m. A mesh density of 10 nm is set. The boundaries are periodic in x and y, and PML in z. The structure formed in Sentaurus is shown on the top-right (plotted with SVisual), whilst the simulation domain for Lumerical is shown on the bottom-right (plotted with Lumerical Visualiser).

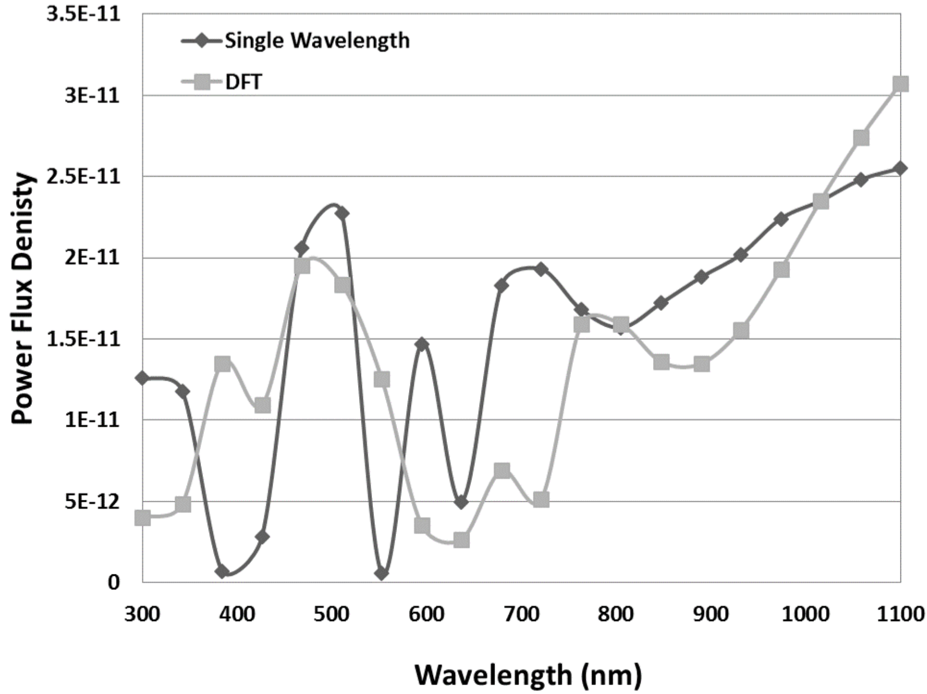

Figure 3.7: Comparison of reflected power flux density on silicon nanowire using DFT and single-wavelength simulation with the Sentaurus EMW solver.

FDTD Optical modelling

Sentaurus provides an electromagnetic wave (EMW) solver that also uses the FDTD method [101]. However, Lumerical shows enhanced simulation time efficiency as observed in Fig. 3.6. The simulations were performed on a SiNWA whereby all parameters, including boundary conditions, mesh density and termination criteria are kept consistent. These results show that Lumerical is more efficient and has negligible dependence on the discrete Fourier transform (DFT) resolution (i.e. number of wavelengths measured). Furthermore, for this example, due to the simplicity of the structure, Lumerical works more efficiently in single-core than in multi-core. This however, is not observed in the Sentaurus case. Potentially, Lumerical can outperform Sentaurus further by using symmetry and antisymmetry boundaries in x and y (this exploits the symmetry of these structures and quarters the simulation domain).

The Lumerical package has also proven to provide more consistent optical results for broadband wavelength simulations compared to that of the Sentaurus EMW solver. An error noted by Sentaurus on their internal site, as a code defect in calculating the discrete Fourier transform (DFT) phase factors, may be the root cause of this inaccuracy in DFT

simulations. As a result, optical quantities extracted from EMW simulations using DFT can exhibit errors compared to continuous wave results [102]. To illustrate the error observed, Fig. 3.7 compares the power flux density through a reflection data monitor for both cases. To circumvent this problem, Synopsys advise to either use a sequence of single-wavelength continuous wave simulations instead of a single DFT simulation for multiple wavelengths, or else create user-defined dispersive model poles to produce better fitting of the complex refractive index data [102]. The newest version of the Sentaurus EMW solver provides a visual fitting tool to aid in the latter process. Whilst this may provide a suitable workaround to improve accuracy, it can be a complex step in performing FDTD modelling. Furthermore, the ease of use of Lumerical surpasses that of Sentaurus due its graphical user interface (GUI) whereas the Sentaurus EMW solver is purely code based [101].

Electrical modelling

The Sentaurus Device package is a more advanced electrical modelling package compared to that of Lumerical Device. It provides a more comprehensive physical model database as well as greater choice with respect to numerical solving algorithms. This provides not only more efficient electrical modelling but the ability to analyse a far greater amount of device parameters [89].

3.3 Integration of Lumerical into Sentaurus

The principle behind the tool flow is the ability for SDevice to run an electrical solve using optical data from previous simulations. It does this by reading an input file known as 'optical generation input file (OGI.TDR)'. SDevice reads this TDR file that contains optical generation data and interpolates it to the geometry and doping data also provided, to run optoelectronic simulations. This means that if the optical solve data from Lumerical can be written to a TDR file, then it can be used in SDevice.

As such, the process is as follows: the structure is formed using SProcess; this structure is used in SDevice to run purely electrical simulations and therefore give dark IV characteristics. The tool at this stage is also used to produce an 'optical generation output

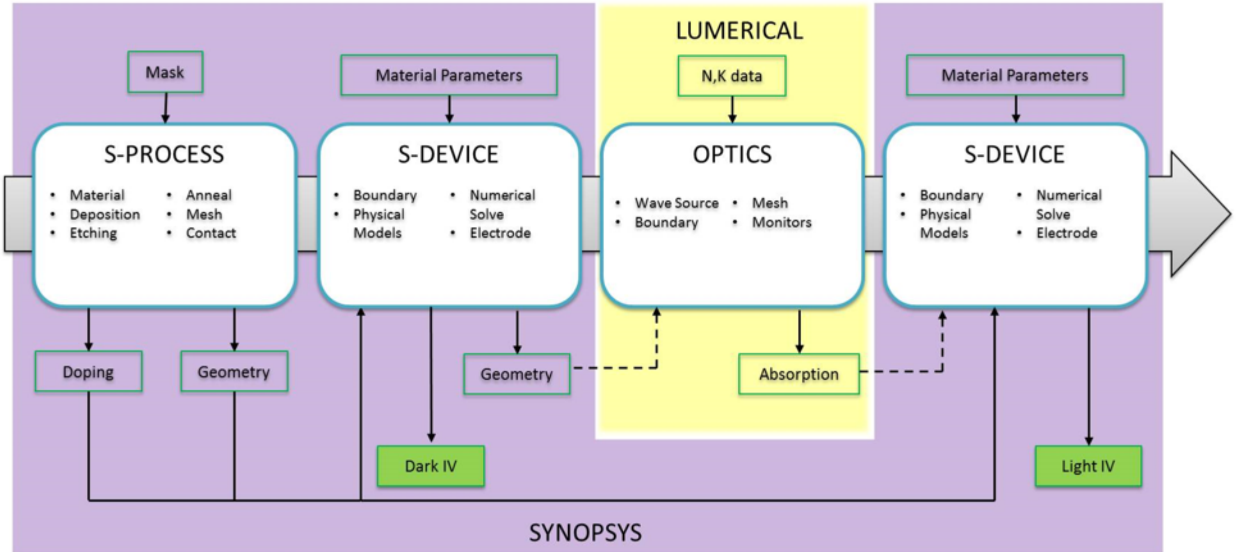

Figure 3.8: An overview of the tool flow used in this work. The key input and output files are shown, as well as the main packages which are called upon and its order of use. The dashed line represents the use of TCL language and Matlab script to interface the files between Sentaurus and Lumerical

(OGO)' file. Whilst no optical solve is executed, it will produce an OGO.TDR, with zero for carrier generation but containing the necessary coordinate information, that is used as the template on which to write Lumerical output data. Once Lumerical data is written onto this OGO.TDR file, this then becomes an optical generation input file (OGI.TDR) at the second stage of SDevice.

3.3.1 Tool flow

The tool flow can be seen in Fig. 3.8. The four main tools used, are SProcess, SDevice, Lumerical and finally SDevice again. To illustrate the use of this tool flow, a hybrid Si pyramid-NWA structure is modelled [103], as this utilises many of the useful steps that are provided for PV simulation. The full script used to form this structure on SProcess and model on SDevice are provided in Appendix 2. The following shows pseudo-code for descriptive purposes. The first tool used is SProcess.

Listing 3.1: Script defining SProcess pseudo-code for fabricating a hybrid Si pyramid-NWA structure

```
1 Initialise Silicon structure
2 Etch Pyramid{
```

```
3         Grow Oxide
4         Deposit Resist
5         Apply Mask and expose (read from Mask file)
6         Etch Oxide
7         Strip Resist
8         Apply crystallographic etch on Silicon
9         Etch Oxide}
10 Etch Nanowires{
11        Deposit Resist
12        Apply Mask and expose (read from Mask file)
13        Apply anisotropic etch on Silicon
14        Strip Resist}
15 Apply Mesh algorithm
16 Dope structure{
17        Deposit spin-on-dopant (e.g. Phosphorous)
18        Thermally anneal structure to diffuse dopants
19        Etch grown oxide}
20 Define new material (Indium Tin Oxide)
21 Deposit Indium Tin Oxide
22 Define Contacts
23 Save structure (SPROCESS.TDR)
```

This tool works by first (as shown in listing 3.1) defining an initial Si substrate, followed by the various fabrication steps to build the structure. This often involves a mask file that is used for lithography steps. New materials are also defined, as well as meshing strategies to ensure accurate processing and future convergence in device simulations. Contacts are defined as the last step. The output data is of TDR format, and contains a multitude of datasets (e.g. doping concentration, geometry, stress, etc.) that completely describe the geometry and material parameters at equilibrium.

The second tool is SDevice.

Listing 3.2: Script defining SDevice pseudo-code for simulating the SProcess structure in the dark, i.e. no optical solve is undertaken

```
1 Set input data{
2         Grid = SPROCESS.TDR
3         }
4 Set output data{
```

```
5         Plot= FULL_PLOT.TDR
6         Current = DARK_IV.PLT
7         OpticalGenerationOutput = OGO.TDR
8         }
9 Set data fields to plot {
10        Doping Profiles, Band structure
11        Carrier Densities, Currents, Traps
12        Fields, Potentials and Charge distributions
13        Generation/Recombination, Optical Generation
14        ...
15        }
16 Define Electrodes
17 Define Physics models{
18        Traps
19        Recombination{
20                Shockley-Read-Hall, Auger
21                Radiative, Surface
22                }
23        Mobility
24        }
25 Set Iterative method and power{
26        Newton/Gummel
27        Number of CPU
28        }
29 Apply electrical sweep{
30        Quasistationary Voltage Start, Step, End
31        Solve Poisson for electrons  and holes
32        }
```

This stage (as shown in listing 3.2) is to use the output structure from SProcess to run current-voltage (IV) simulation without any light absorption. This will give the IV characteristics in the dark and also produces an optical generation output TDR file. The SDevice command file takes in the geometry and doping data from SProcess and applies a numerical solve. It implements specified device physics models from a comprehensive database. User-defined material parameters can overwrite default parameters to account for more recent published or in-house experimental data (e.g. surface recombination velocity for NW-air interfaces). A full output TDR file is also produced and this contains

all the specified plot data (e.g. electric fields, carrier generation profile, current density, mesh, etc.).

The third tool is Lumerical.

Listing 3.3: Script defining Lumerical pseudo-code for simulating the SProcess structure

```
1 Import structure{
2         Binary file = OGO.TXT
3         Refractive index = Published tabulated data
4         }
5 Define simulation domain{
6         Mesh Accuracy
7         Boundary conditions{
8                 Periodic
9                 Anti-Symmetric, Symmetric
10                Perfectly Matched Layers
11        Termination Criteria
12        }
13 Define source wave{
14        Type = Plane
15        Wavelength range = 300 nm - 1000 nm
16        Location = plane above structure
17        }
18 Define monitors{
19        Reflection monitor{
20                2D
21                Location = plane above source wave
22                }
23        Absorption monitor{
24                3D
25                Downsampling
26                Location = boxes covering structure
27                }
28 Set CPU/Memory power
```

The Lumerical tool (as shown in listing 3.3) which is sandwiched in-between the two SDevice packages imports the structure from the output data of the first SDevice simulation. Whilst the complex 3D structure can be imported from Sentaurus tools, simpler

structures can be resconstructed without any importation using Lumerical own structure editor. This tool can also make use of the mask file as both packages utilised the industry standard GDS format. Once the structure is imported, the refractive index data of the materials is also required. The structure is then re-meshed depending on the simulation constraints.

The three key elements to the simulation is the injected wave source, the boundary conditions and the monitors used. The latter determines the output data. For PV simulations a key monitor is an analysis group 'solar generation'. This outputs a spatial carrier generation profile of the structure in a MAT file. For very complex structures that require fine meshing, often the output files are too computationally intensive, limited by random access memory (RAM) to calculate in one simulation. As such, the monitor can be down-sampled such that adjacent mesh cells are averaged, or often the simulation is run numerous times and each time the monitor is confined to a different section of the structure. As a smaller number of cells are now computed, less RAM is required. The total generation profile is then merged from the numerous monitor files.

The final stage is SDevice

Listing 3.4: Script defining SDevice pseudo-code for simulating the SProcess structure under light, i.e. optical models are included and optical data is imported

```
1 Set input data{
2         Grid = SPROCESS.TDR
3         OpticalGenerationInput = OGI.TDR
4         }
5 Set output data{
6         Plot= FULL_LIGHT_PLOT.TDR
7         Current = LIGHT_IV.PLT
8         }
9 ...
10 ...
11 Define Physics models{
12        Traps
13        Recombination{
14                Shockley-Read-Hall, Auger
15                Radiative, Surface
```

```
16                  }
17          Mobility
18          Optics{
19                  ReadFromFile=OpticalGenerationInput
20                  }
21          }
22 ...
23 ...
24 Apply electrical sweep{
25          Transient{
26                  Gradual increase to OGI data
27                  Time start, step, end
28                  }
29          Quasistationary Voltage Start, Step, End
30          Solve Poisson for electrons and holes
31          }
```

This final stage (shown in listing 3.4) is the IV simulation under illumination. It uses the already processed OGI.TDR file and interpolates the carrier generation data. Since geometry from this will match that of SPROCESS.TDR exactly, there is negligible error. Therefore, no optical solve is undertaken using SDevice in this tool flow, only its ability to take in carrier generation data from a TDR file. Since this simulation generates a large current density at the initial guess of the electrical solve (0 V), an initial transient simulation is undertaken before the quasi-stationary voltage sweep.

3.3.2 TCAD-Lumerical Interface

The integration of the two separate packages is achieved by data extraction using a TCL language script and data mapping using a MATLAB script. In this section the pseudo-code is shown, such that other languages can be used, however the full script is available in Appendix 2. See Fig. 3.9 for a comparison of the mesh and the carrier generation profile after mapping between Sentaurus and Lumerical.

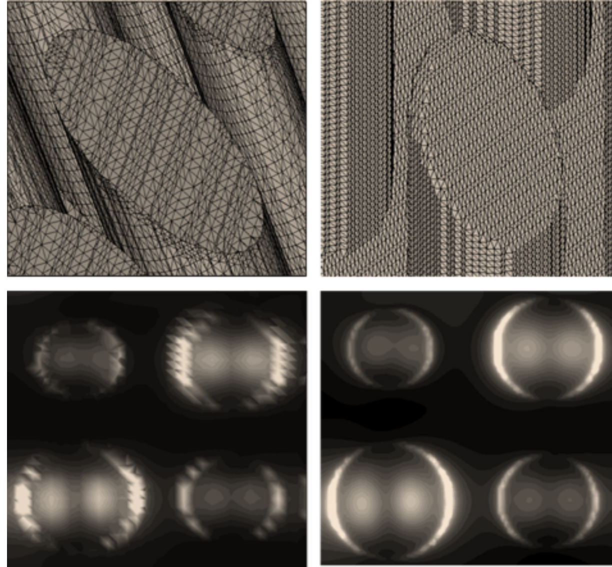

Figure 3.9: Top: Comparison of mesh quality between Delaunay mesh in Sentaurus (left) and Cartesian mesh in Lumerical (right). Bottom: Comparison of the optical carrier generation data, after mapping from Lumerical (right) to Sentaurus (left). The images for Sentaurus are plotted in SVisual and for Lumerical in Matlab.

File types

As mentioned previously, the standard file format throughout TCAD Sentaurus is TDR. It contains various datasets (e.g. dopant concentration) for every state (for transient simulations), region and geometry of the structure. To import the structure to Lumerical, the coordinate data must be in a TXT file format. The output of Lumerical (i.e. spatial absorption profile) is in a .MAT file. Finally, for post data mapping, the absorption data must be written into the TDR format for use in SDevice.

Sentaurus to Lumerical

The first step is to access the TDR file and unfold the data into a format that is readable by external packages such as Lumerical. The TDR file in this case is the optical generation output after the first stage of SDevice. This has no optical solve and as such the dataset 'optical generation' will have a zero value. However, this file is useful as it contains the relevant coordinate list for optical modelling. The aim is to extract this coordinate list into a data form that can be read by Lumerical.

Listing 3.5: Script defining TCL pseudo-code for outputting structure data from the TCAD file format to a TEXT file readable by MATLAB

```
1 set input file {
2         Input = OGO.TDR,
3         permission = "read"
4         }
5 set output file {
6         Output = OGO_coordinates.TXT
7         permission = "write"
8         }
9 Find number of datasets {
10        Specify location in TDR{
11                Geometry, Region, State
12                }
13        Get number of datasets
14        }
15 Find coordinate data {
16        For all datasets{
17                find those that contain 'optical generation' quantities
18                extract x,y and z coordinate
19                save coordinate to 'coordinate list'
20                }
21        }
22 Write 'coordinate list' to 'OGO_coordinate.TXT'
```

This process (shown in listing 3.5) is necessary as it extracts the coordinates of the simulation space that is relevant for optical modelling. This data can be reconstructed such that the structure is reproducible in Lumerical. The import function in Lumerical requires a binary list whereby 1 and 0 represents the presence and absence of material, respectively. This list refers to the geometrical location (X_1, Y_1, Z_1) to (X_j, Y_k, Z_l) where j, k and l are last indices in each respective plane. The following code is used for this purpose:

Listing 3.6: Script defining MATLAB pseudo-code for outputting TCAD structure data to a binary list readable by the Lumerical import function

```
1 set input data{
```

```
2         structure_xyz = Read 'OGO_coordinate.TXT'
3 }
4 create full coordinate list {
5         find all unique coordinates x,y,z
6         define mesh density factor  Nx,Ny,Nz
7         list all possible combinations of x,y,z
8         }
9 create binary list {
10        for all rows in full coordinate list{
11                if coordinates match input data
12                        then write 1 to binary_list
13                        else write 0 to binary_list
14                        }
15                }
16 Write 'binary_list' to 'binary_list.TXT'
```

Listing 3.6 essentially creates a coordinate list for a Cartesian grid with uniform spacing in each plane. The density of this depends on the values of the mesh density factors (Nx, Ny and Nz). When equal to 1, this will represent a grid density which ensures no loss of data when replicating the structure in Lumerical. As these values increase, there is some loss in data but any degradation in the replica will depend on the complexity of the structures. In cases of simple structures on a low RAM computer, increasing these numbers may be beneficial.

Lumerical to Sentaurus

The output of the Lumerical simulation is a 3D matrix data representing the carrier generation profile within the whole simulation domain. In order to map this 3D profile to the structure back in TCAD, the first stage is to list the carrier generation data for each coordinate that exists for the structure. This data will then be written into the TDR format.

Listing 3.7: Script defining MATLAB pseudo-code for mapping carrier generation data outputted from Lumerical to the structure profile from TCAD

```
1 set input data{
2         structure_xyz = Read 'OGO_coordinate.TXT'
```

```
3         absorption_profile {
4                  Read 'lumerical_1.MAT'
5                  Read 'lumerical_2.MAT'
6                  Read 'lumerical_3.MAT'
7                  ....
8         }
9 For the number of rows in structure_xyz{
10        match coordinates in absorption_profile{
11                limit search space{
12                        check if coordiante exists in MAT file 1,2,3..
13                        }
14                find minimum distance {
15                        absorption_data(x,y,z)-structure_xyz(x,y,z)
16                }
17                Extract absorption data
18                }
19        if absorption data < 1 {
20                increase search space
21        until absorption data found
22        extract absorption data
23        }
24 }
25 Write absorption data to OGI.TXT file.
```

Lines 19-23 in listing 3.7 are used to ensure that at an air-structure interface, the surface of the TCAD structure, takes the data of absorbed material in Lumerical and not the air material. This is achieved by first checking if the absorption data taken for the nearest matching coordinate is negligible, i.e. less than 1. If this is the case, then a search method begins whereby the search space grows by one mesh cell in all directions until the nearest absorption cell is found.

Once the absorption data has been collated into a list corresponding to the structure coordinates, it is then written onto the TDR file. Since the coordinate list is taken from the structure post-device, it is a simple process of overwriting the carrier generation (currently 0 after "dark" simulation) for each location. This TDR file then assumes an illuminated structure and the IV simulation can be undertaken.

Listing 3.8: Script defining TCL pseudo-code for writing carrier generation data from a TEXT file into a TCAD structure file

```
1
2 set input file {
3         Input = OGI.TXT,
4         permission = "read"
5         }
6 set output file {
7         Output = OGI.TDR
8         permission = "write"
9         }
10 Find number of datasets {
11        Specify location in TDR{
12                Geometry, Region, State
13                }
14        Get number of datasets
15        }
16 Overwrite Absorption data {
17        For all datasets{
18                find those that contain 'optical generation' quantity
19                overwrite data quantity with Input data
20                }
21        }
```

The key component in listing 3.8 is that the number and order of coordinates in the TDR and TXT file must match.

3.4 Conclusion

In this chapter optical modelling techniques and tools is shown, and an integration tool for Lumerical and TCAD Sentaurus is developed. A finite-difference time domain approach is used to undertake the optical simulations as this allows sub-wavelength features to be modelled accurately, and broadband wavelengths to be modelled efficiently. The optical results from the commercial package Lumerical FDTD was then interfaced to Synopsys Sentaurus TCAD (This package is described in the previous chapter). A tool flow was established to integrate these two softwares in order to undertake accurate and efficient

opto-electronic simulations. The work for this chapter was published in [99]. The full code for achieving the integration is shown in Appendix 2.

4 Silicon Nanowire Array

In chapter 1, section 1.3, surface roughness was highlighted as a technique to reduce reflection and increase effective junction area. Texturing the surface can be achieved via physical etching such as deep reactive ion etching (DRIE), or chemical etching in the form of alkalines such as potassium hydroxide (KOH) or acids such as hydro-fluoric (HF) acid. Utilising wet chemical etching to form textured surfaces is more cost effective for mass production and thus advantageous over plasma enhanced chemical vapour deposition (PECVD) and DRIE.

At the sub-micron level, where the wavelength is at the same length scale as the feature size, NWAs have been utilised. Vertically aligned SiNWAs are a growing technology field in photovoltaic (PV) cells [25–27]. The current photovoltaic industry is dominated by crystalline or poly-crystalline Si in a planar p-n junction configuration. The use of SiNWAs within this industry has shown great promise due to its application as an anti-reflective layer. In fact, with SiNWAs, absorption can be increased to above 90% for a wavelength range of 400 - 800 nm [66, 104]. Furthermore, the fabrication process of SiNWAs can be of low-cost using metal assisted chemical etching (MACE) [48]. Other methods such as vapour liquid solid [105] growth as well as pattern and RIE [106] also show promise, forming more ordered arrays than the MACE process but at a higher cost.

SiNWs can either be prepared through a top-down or bottom up approach. The first involves a dimensional reduction of bulk silicon; this can be done via RIE, MACE, or electron beam lithography. The bottom up approach, whereby silicon atoms are assembled to form the NWs, can occur through processes such as vapour liquid solid (VLS) growth [65] and oxide assisted growth (OAG) [107]. Currently the most common of these methods are chemical vapor deposition (CVD) through a VLS mechanism and MACE. Although the bottom up approach can produce NWs with smaller diameter generally (< 10 nm), the

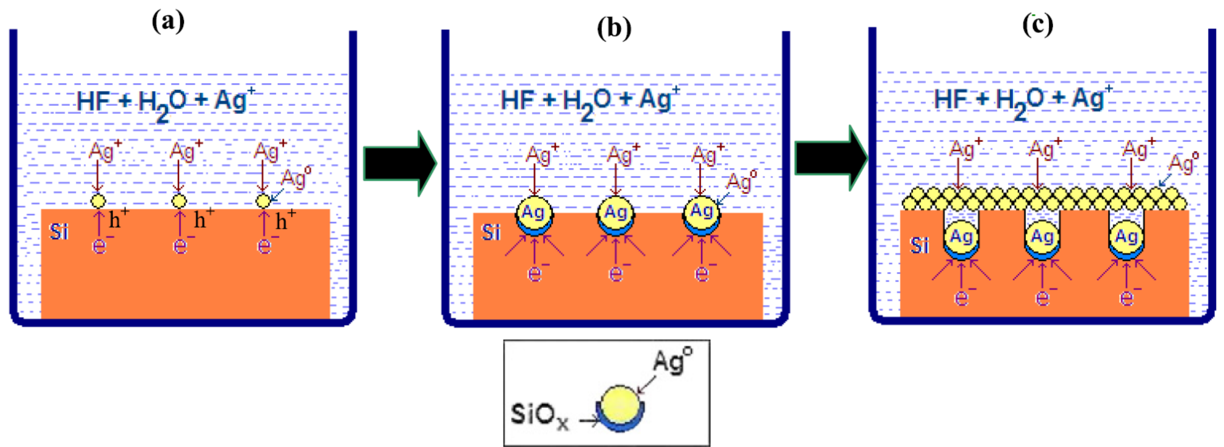

Figure 4.1: The process of MACE [108]. (a) Formation of Ag nuclei at the substrate surface due to redox reactions between Ag^+ ions and Si (b) Growth of the Ag nuclei and consequent sinking into the substrate due to oxidative dissolution of the Si surface (c) Preferential charge transfer leading to vertical propagation of Ag nuclei, with remaining material producing standing NWs and accumulation of Ag dendrites at the surface.

top down approach is favourable because it provides better controllability. In a top down approach, the electrical characteristics of SiNWs are inherited from the wafer from which it was etched; whereas, a bottom up approach would produce SiNWs that are intrinsic and thereby require doping during growth.

4.1 MACE

MACE in particular is a popular NW preparation method for solar cell use, having produced vertically aligned SiNW that are uniform in terms of doping profile, crystal orientation, density, size, and shape [48]. This is a process which begins with nucleation of Ag or Au, and is followed by etching in HF solution with the metal NPs as catalysts [58, 59]. In reference to Fig. 4.1, the process can be summarised as follows:

First Ag^+ ions are reduced to elemental Ag nano-particles ($AgNP$) due to hole injection into the valence band (VB) of Si. This charge transfer occurs as the equilibrium redox potential of the Ag^+/Ag system is situated beneath the edge of the Si VB, see Fig. 4.2. The hole injection into the Si substrate leads to both Ag atoms depositing on the surface as well as SiO_2 formation at the Ag/Si interface.

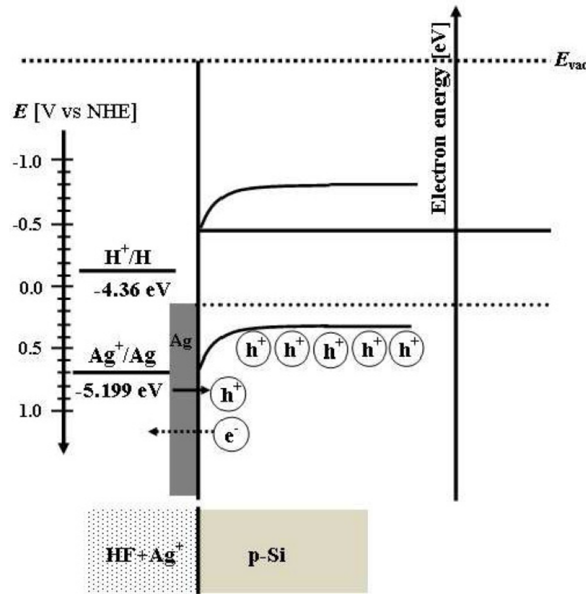

Figure 4.2: Charge transfer between Ag^+/Ag system and valence band of Si [108].

Second Dissolution of oxides by HF and further growth of Ag nuclei into bigger particles. The oxidative dissolution of Si (i.e. removal of SiO_2 at the Ag/Si interface), and the consequent sinking of the Ag particle, leads to the formation of pits.

Third The etch is anisotropic due to preferential charge transfer at the Ag/Si interface, and negligible etch rates in non-Ag regions. This leads to the formation of SiNWs. The roughness in the side walls of the SiNWs is due to the diffusion of excess holes at the Ag/Si interface.

The equations defining this process are:

$$4Ag^+ \rightarrow 4Ag(s) + 4h^+ \tag{4.1}$$

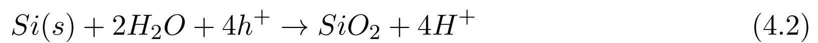

$$Si(s) + 2H_2O + 4h^+ \rightarrow SiO_2 + 4H^+ \tag{4.2}$$

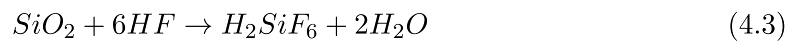

$$SiO_2 + 6HF \rightarrow H_2SiF_6 + 2H_2O \tag{4.3}$$

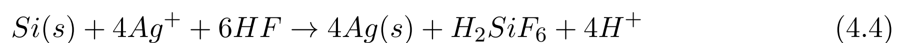

$$Si(s) + 4Ag^+ + 6HF \rightarrow 4Ag(s) + H_2SiF_6 + 4H^+ \tag{4.4}$$

There are many factors which will influence the properties of the SiNWA when fabricated using this process. Fig. 4.3a illustrates a plot of NW etch time (t_{etch}) against SiNW length (L_{NWA}) [108]. It is evident from this figure that L_{NWA} increases with t_{etch}, with a faster etch rate apparent for $t_{etch} < 120min$. The change in etch rate is a result of prolonged reduction of HF and Ag concentration with time. The temperature also directly impacts the etch rate as shown in Fig. 4.3b by changing the kinetics of the redox reactions. This shows an increase in etch rate as a function of temperature. It is also reported that increased temperature can not only impact the height but also the overall morphology, with less controllable lateral etching. Porous structures have been reported for temperatures exceeding 50°C. The composition of the etching solution also impacts the etch rate and the morphology of the SiNWA. Fig 4.3c illustrates the influence of Ag concentration on L_{NWA}. It is shown that an increase in length is observed with increasing Ag conc. upto 50 mM, after which the etch reduces. It is also noted that the morphology of SiNWA becomes more non-uniform as the conc. exceeds this value. Increased Ag conc. lead, to a higher reduction rate from Ag^+ to Ag, thereby increasing the hole injection into the Si VB at the interface. This then results in an increase in oxidative dissolution, producing larger L_{NWA} for the same HF conc., time and temperature. However, increase of the Ag conc. excessively can be detrimental to the height and uniformity because the hole injection rate into silicon interface at the pore, is faster than the hole consumption. The remaining holes will then diffuse to non Ag/Si interfaces away from the pore, towards hole depleted regions such as HF/Si interfaces. Therefore, oxidative dissolution occurs across all Si surfaces uncontrollably and produces non-uniform nanowires. Fig. 4.3d shows that the impact of HF conc. on L_{NWA}. A linear relationship is observed, upto 10 M, whereby L_{NWA} increases with HF conc. This is as a result of increased oxidative dissolution when HF becomes abundant. This dissolution is an exothermic reaction and therefore increases the temperature at the reaction regions, thereby increasing the etch rate further. However, excessive HF conc. can lead to lateral and less controllable etching, similar to the effect manifested by excessive Ag conc. In summary, controlling the L_{NWA} and uniformity is a fine balance between Ag conc., HF conc., time and temperature.

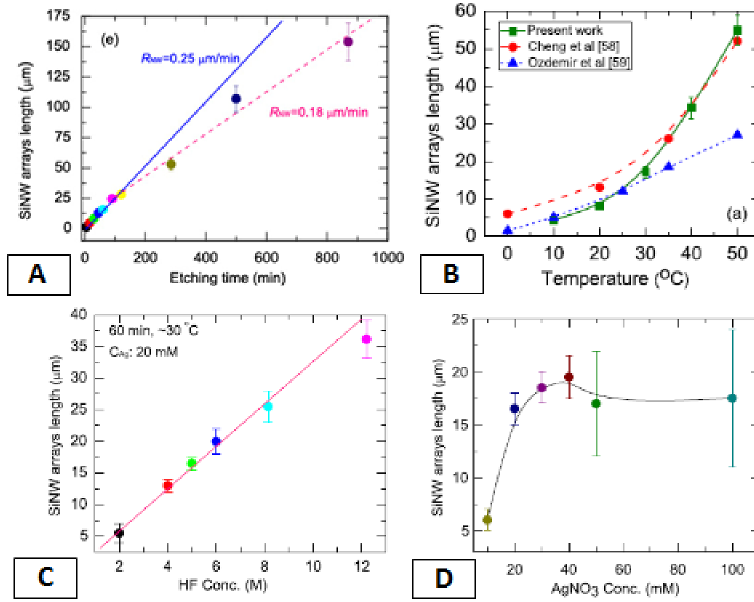

Figure 4.3: This figure illustrates the influence of temperature, etch time, HF conc. and $AgNO_3$ on the etch length of SiNWA for a single etch step process. These graphs were taken from [108]. The graphs illustrate a linear relationship for time and HF conc, whilst a non-linear relationship for temperature. Furthermore, a peak in etch length is found for the case of increasing $AgNO_3$ conc.

4.2 Fabrication

The fabrication of SiNWAs can occur in a single or two-step process. The former is by depositing the Si substrate in a single solution of $AgNO_3$/HF and using temperature as a catalyst. The two-step process deposits the Si substrate firstly into $AgNO_3$/HF and is then followed by H_2O_2/HF. Both processes begin with a rigorous cleaning step and end with a Ag removal step. Additional steps are involved for more complex structures. Whilst an in-house repeatable two step process was established prior to this project [63], due to the need for uniform sub-micron L_{NWA}, a single step etching process was developed for this PV project.

4.2.1 Cleaning

Once the initial Si wafer has been cleaved to the desired size, the first process is to clean.

1. Ultrasonication in isopropyl alcohol (IPA) for several minutes. This is a widely used solvent in microelectronic fabrication to remove dirt and it also replaces water on a Si surface due to its low surface tension. As the sample is taken out of IPA, the

volatile solvent will evaporate almost immediately.

2. The sample is then placed in a piranha etch solution. This is a mixture of hydrogen peroxide and sulfuric acid (3:1, conc. H_2SO_4:30% H_2O_2). This solution dissolves any organic contaminants and in doing so causes vigorous bubbling. The mixing of the solution is an exothermic reaction and as such the temperature can rise 100°C and above. This cleaning step is always undertaken in a glass beaker.

3. A thorough rinse in HPLC[1] grade H_2O. This grade of H_2O is preferred over deionised (DI) water due to its purity. The H_2O is made for use in high performance liquid chromatography, where even the smallest of contaminants can lead to noise in the results. As such, this grade of H_2O is filtered to minimise ions, particles and bacteria. It is packaged in solvent-rinsed amber glass and sealed in inert atmosphere. For the MACE etch process, particularly when etching sub-micron length wires, the use of HPLC water over DI water is critical. It ensures a clean surface for homogeneous Ag nucleation.

4.2.2 Single-step

The single step etch process involves a solution of 3 M HF:0.06M $AgNO_3$ in a 1:1 ratio at a temperature of 50°C. The 60 mM $AgNO_3$ stock solution is made by dissolving 2.55 g of $AgNO_3$, which has a molecular weight of 170 g, in 250 ml of H_2O. 10 ml of this stock solution is added to 10 ml of 3 M HF solution. The total etchant volume of 20 ml is sufficient to etch sample sizes of 2 cm^2. The 3 M HF solution is made by adding 1 ml of 50% conc. HF to 9 ml of water. The measurement and dispensing of HF is undertaken using special PTFE equipment, which minimises spillage. The etching solution is contained within a PTFE beaker, which is placed within a water bath and the temperature set to 50°C. The sample is placed within the etching solution, and the etch time is dependent on desired length. To terminate the etch, the sample is removed from etchant solution and rinsed thoroughly in DI water. The SiNWA is then placed into concentrated HNO_3 (5M) to remove the Ag particles between the wires and the large accumulated dendrites on the surface.

[1]This an industry standard technique known as high pressure liquid chromatography for pharmaceutical analysis [109]

4.2.3 Two-step

For the two step process, an aqueous solution of 0.06 M $AgNO_3$ and 5.6 M HF is used for the formation of Ag particles (i.e. nucleation). The samples are then thoroughly rinsed in DI water such that excess particles are removed, and promotes localised etching. The samples are then immersed into a second solution, 5.6 M HF and 0.3 M H_2O_2, for etching. As is the case for the single step etch, the samples are immersed for an etch time that is dependent on the desired length, and the etch is terminated by removing from solution and rinsing thoroughly in DI water. Finally, the sample is placed in conc. HNO_3 to remove the aforementioned residual Ag.

4.2.4 Single-Side

In order to etch only one side of the substrate, the other must be protected from the etchant. Due to the etching prowess of HF this makes protection a difficult task. The most effective and simple method is to clamp a sacrificial silicon substrate on the back side using PTFE clips. This is a technique that can be applied prior to the etching and after the cleaning steps. Other techniques of using photo-resist and PMMA as both a protective film and as an adhesion layer for a backside Si sacrificial piece can be used; however this was found to be less effective and prone to contaminating the samples.

4.3 Results and Discussion

In this section, the morphology of the in-house fabricated SiNWA is discussed followed by optical measurements and modelling results.

4.3.1 Morphology

Fig. 4.4 illustrates the morphology of a SiNWA fabricated using a two-step etch process, with $L_{NWA} \approx 15\ \mu m$. The nucleation time for this etch was $t_{nucl} = 15$ min and the etch time, $t_{etch} = 20$ min. The SiNWA has etched perpendicular to the bulk surface and therefore incorporates the properties of the bulk material i.e. crystallinty and orientation. The nucleating Ag remaining at the base of the SiNWA pores can be seen in Fig. 4.5, this is the manifestation of metal assisted etching. The diameter of the NWAs (D_{NWA}) are in

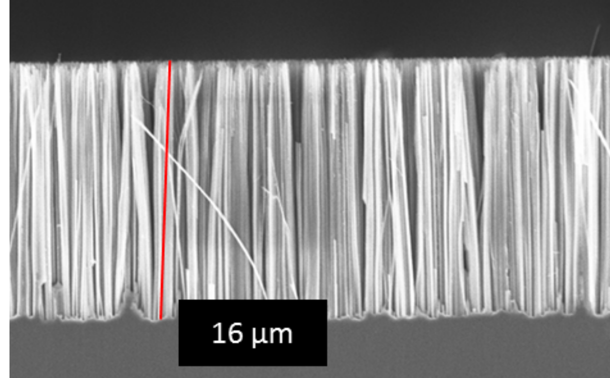

Figure 4.4: SEM showing a SiNWA cross-section fabricated using the two-step etch process at room temperature, with t_{nucl}= 15, t_{etch}= 20, and 0.03 M $AgNO_3$:5.6 M HF solution.

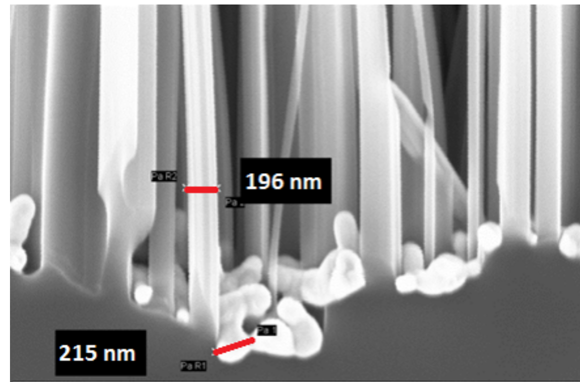

Figure 4.5: Silver nanoparticle size formed from MACE process.

the range of 30 - 250 nm. Fig. 4.4 illustrates how SiNWA of this length can be flexible and tangle towards the top. The bunching occurs as the MACE is a water-based etching process, so during the drying process the NWs agglomerate in order to reduce surface tension, and are held together with van der Waals forces.

Fig.4.6a illustrates the morphology of SiNWA fabricated using a single-step etch process, with $L_nwa \approx 1\mu m$. The etch time for this SiNWA is $\approx 5min$. The SiNWA is well aligned with a uniform skyline, i.e. all of similar height. Similar to the SiNWA etched from the two-step etch process, the SiNWA shows bunching behaviour as shown in Fig.4.6b. Fig.4.6c shows the formation of Ag dendrites on top of the SiNWA during the etching process. This is removed using conc. NHO_3.

A comparison of L_{NWA} for a given HF conc., Ag conc. and etch time is shown in Fig. 4.7. The temperature is set to 50°C. The high concentration of HF represents 5 M, whilst low is 2 M. In the case of Ag conc., the high value is 0.06 M and low is 0.04 M. Similar to

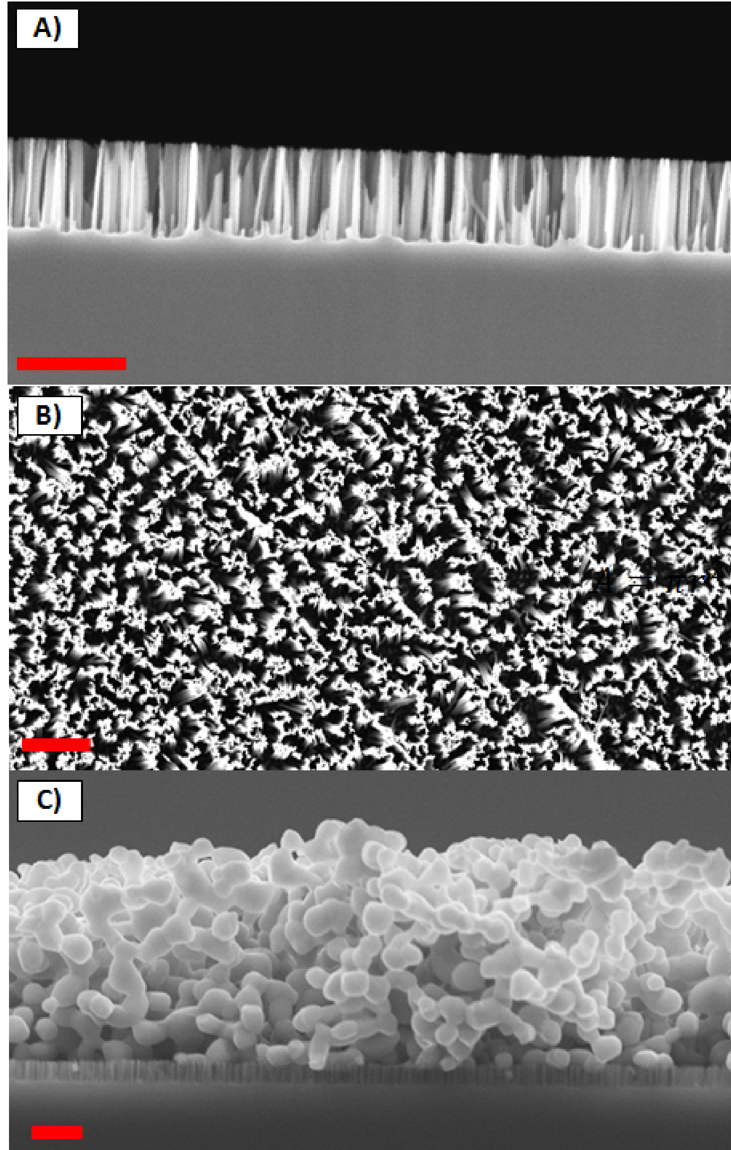

Figure 4.6: SEM images showing SiNWA fabricated using a single step etch process with temperature = 50°C, t_{etch} = 5 min , and 0.06 M $AgNO_3$:2 M HF solution. a) Cross-section view b) Top view c) Image of Ag dendrites during SiNWA formation. The scale bar for images a, b and c is 1 μm, 2 μm, and 3 μm respectively.

.

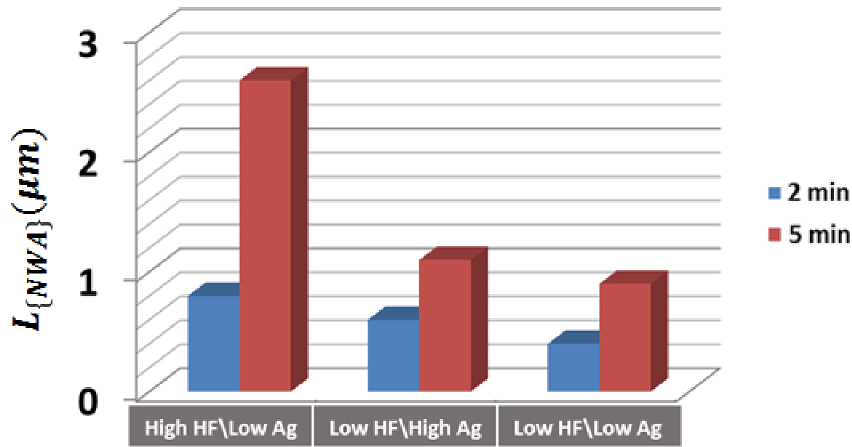

Figure 4.7: Etch length of SiNWA under various etch time, HF conc. and $AgNO_3$ conc. using a single step MACE process at a temperature of 50°C.

the aforementioned literature results, the in-house SiNWA length increases with increasing time, HF conc. and Ag conc. Sub-micron NWs can be controllably achieved (i.e. within a window of 2 - 5 min etch time) when reducing the HF concentration to 2 M. Whilst lower Ag conc. produces shorter SiNWA, it was found less controllable, often producing poorly formed SiNWA (i.e. less repeatable). As such, a recipe of 50°C with 0.06 M $AgNO_3$ and 2 M HF in the range 2 - 5 min was established to form controllable sub-micron SiNWA.

4.3.2 Optical

Fig.4.8 shows the reflectivity measurements for varying lengths of SiNWA and bulk. The set up for measurements can be found in Appendix 1. The measurements show a significant reduction in reflectivity over a broadband spectrum (400 - 950 nm) of SiNWA compared to bulk Si. Furthermore, an increase in L_{NWA} reduces reflectivity further.

To understand the reasons behind the significant reduction in reflectivity, the SiNWA is modelled using Lumerical. The SiNWAs are modelled by placing a cylinder of varying shapes and sizes onto a silicon cuboid block of 200 nm × 200 nm × 1 µm. A plane-wave to model the solar spectrum with wavelength range 300-1000 nm is injected from the top of the simulation domain. Periodic boundary conditions are applied in the x and y direction to replicate our NWs to an array structure, whilst perfectly matched layers have been used in z direction (propagation direction) to absorb any reflected and transmitted fields. This effectively implies that our substrate and free-space are semi-infinite. Symmetric and

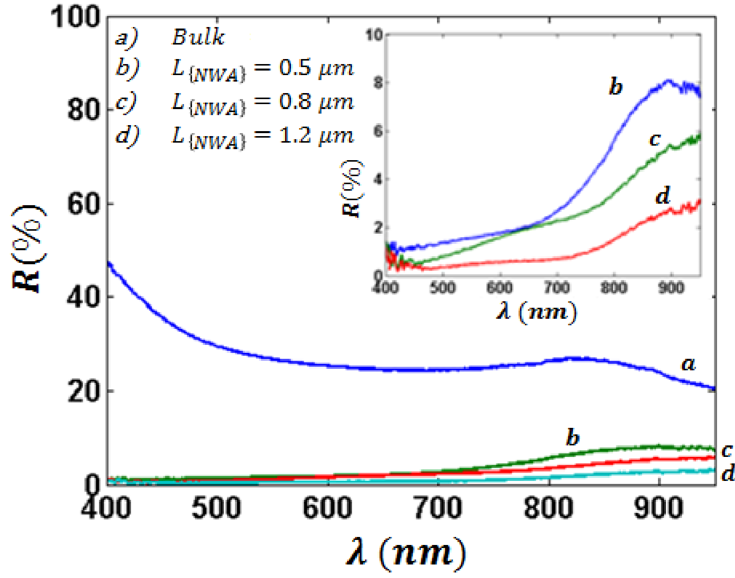

Figure 4.8: Optical measurements for varying length of SiNWA. A kink is observed in the bulk reflectivity between 800 - 900 nm wavelength. This caused by a change in reflectivity of the mirror (see Appendix 1) used as a reference in the measurements and not as a feature of the bulk material.

antisymmetric boundaries have been used to reduce computation time when the unit cell allows it. A meshing algorithm is applied by the solver to form a mesh as a function of the material refractive index and interface structure. After a convergence analysis, the maximum and minimum length of our mesh cell is set to 14 nm and 2.5 nm, respectively. We also use a termination criteria of 1×10^{-5} , to ensure simulations end when the spectral response obtained by the Fourier transformation is valid. We measure the reflection (R) data from a monitor placed at the top of our simulation domain.

Fig. 4.9 and Fig. 4.10 illustrates the reflection (blue), absorption (red) and transmission (green) of varying SiNWA. The results are shown for cylinder NWA with heights of 0.5 and 5 μm and diameters of 50, 100 and 150 nm. Furthermore, results for tapered wires using cones of 0.5 and 5 μm height and base diameter 150 nm are also shown. The features observed in this figure originate from the material properties of Si and the modes supported by the structure. The SiNW behaves like a circular dielectric waveguide whose eigenmodes are well-known [110]. The confined modes can be found by solving Maxwell's equations with relevant boundary conditions. These include leaky modes, Bloch modes and Fabry-Perot resonances [111–113]. The first two are governed primarily by the geometry and

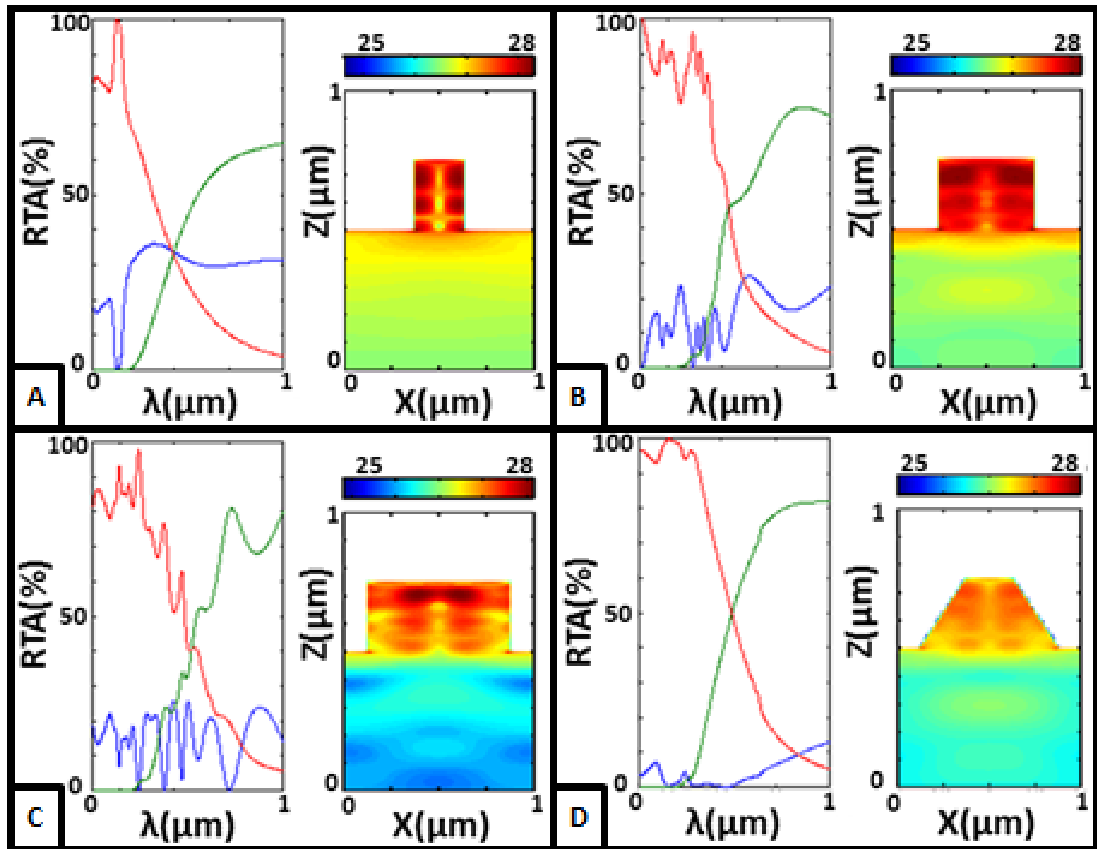

Figure 4.9: This figure illustrates the reflection (blue), transmission (green), and absorption (red) spectra for various SiNWA structures as well as a spatial map of carrier generation rate ($m^{-3} s^{-1}$). The NWA length is 500 nm. a) Diameter = 50 nm b) Diameter = 100 nm c) Diameter = 150 nm d) Tapered wire with top diameter = 50 nm and base diameter = 150 nm. The presence of confined modes can be observed in the carrier generation profile, corresponding to peaks and troughs in the reflection, transmission and absorption(RTA) data. These increase with increasing diameter. The most significant reduction in reflectivity is observed when tapering the wire.

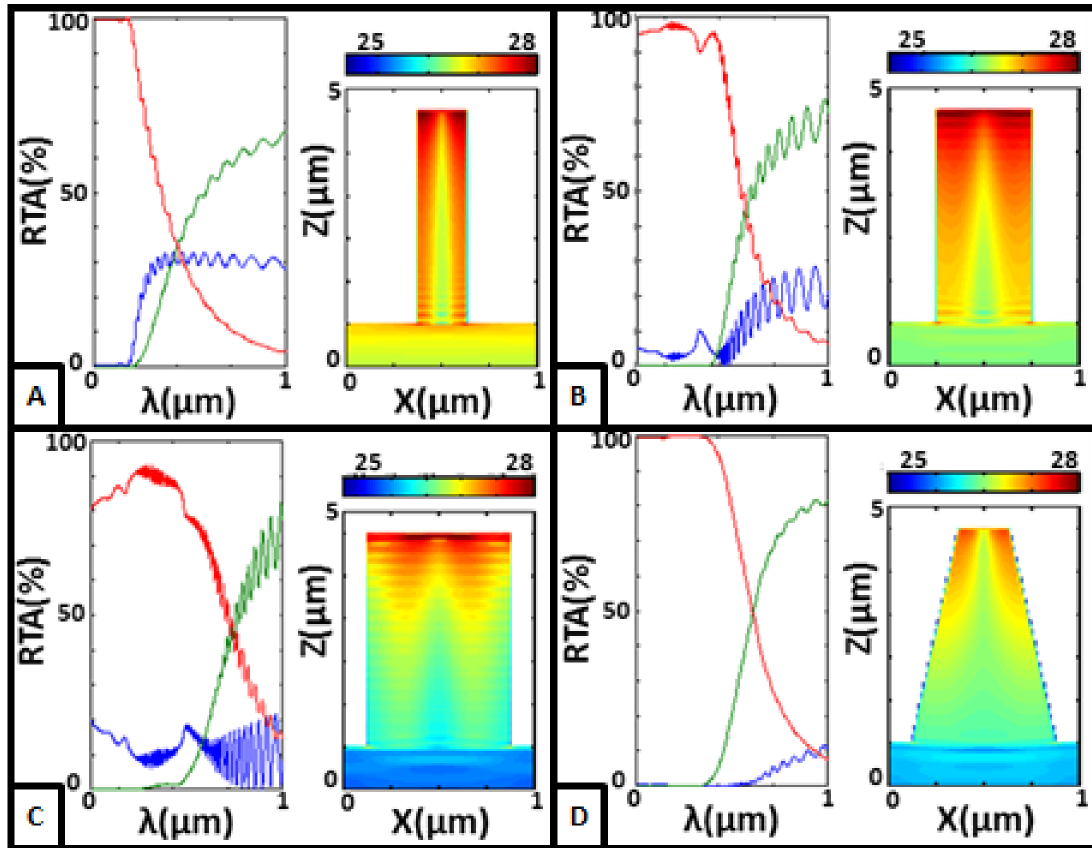

Figure 4.10: This figure illustrates the reflection (blue), transmission (green), and absorption (red) spectra for various SiNWA structures as well as their spatial carrier generation profile. The NWA length is 5 μm. a) Diameter = 50 nm b) Diameter = 100 nm c) Diameter = 150 nm d) Tapered wire with top diameter = 50 nm and base diameter = 150 nm. Fabry-perot resonances are observed due to the interface between top (air/NWA) and bottom (NWA/bulk) of the wire.

periodicity of the NWA. Whilst interfaces of the top (air/NWA) and bottom (NWA/bulk) of the wire result in the Fabry-Perot resonances.

Fig. 4.11 illustrates the reflectivity of a 500 nm long NWA with varying radius from 25 nm to 75 nm. For very small radius and large wavelength, λ, the effect of the SiNW is minimal and the reflection is similar to that of a bulk Si substrate. However, for small λ, the SiNW is no longer insignificant and supports at least its fundamental mode. Hence, the reflectivity drops for $\lambda < 400$ nm, because the excited mode is absorbed at that λ in Si. Furthermore, as the small radius SiNW supports only the fundamental mode, the structure of the spectrum is relatively simple. As the radius increases, absorption is triggered for the whole spectrum. Higher order modes emerge, governed by the radius of the NW, yielding additional structure in the spectrum. Their onset is red-shifted [110], as seen in the red-shift undergone by the dips (Fig. 4.11). The arrival of new modes also modifies the coupling between the incident plane-wave and the already existing modes, which are eventually absorbed. In this analysis we have neglected the interaction between modes of neighbouring SiNWs to give a simple physical insight. However, this assumption is arguably not valid for SiNWs with radius approaching the unit cell size. Hence, the difficulty to describe quantitatively the complex spectrum displayed on the top part of Fig. 4.11.

In Fig. 4.12, the effect of the SiNW surface roughness is investigated as well as the random variance of the NW radius, representative for SiNWs from the MACE process. As a reference, a SiNW of radius 75 nm and length of 500 nm is used (see inset (a) in Fig. 4.12). The roughness is modelled by a root-mean-squared height $\sigma = 5$ and 10 with a correlation length $L_c = 20$ nm in the x, y direction and 170 nm in the z direction, [94] (see inset (b) and (c) in Fig. 4.12). The hypothetical random variance of the radius in the fabricated samples is modelled by a periodic macro-cell with 9 different SiNWs of radius 35 nm, 40 nm, 45 nm, 50 nm, 55 nm, 60 nm, 65 nm, 70 nm and 75 nm (see inset (d) in Fig. 4.12). In the case of the rough and disordered NWAs, symmetric and antisymmetric boundaries are not used. From the comparison of smooth (a) and rough SiNW (b, c), it is evident that the addition of nm-scale roughness to the SiNW surface has a minor effect on the spectrum. There is an overall marginal red-shift of the spectrum as the roughness increases, which accounts for the effective larger diameter of the SiNWs for a specific

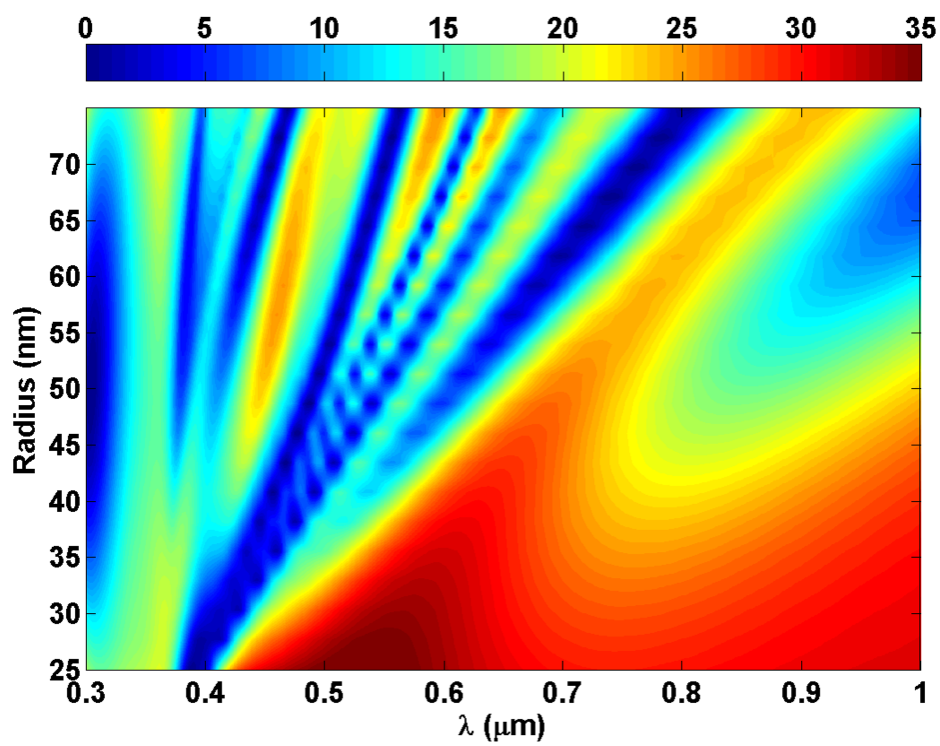

Figure 4.11: Reflectivity (%), represented by the colorbar, of various NWA radius as a function of wavelength for short SiNWA.

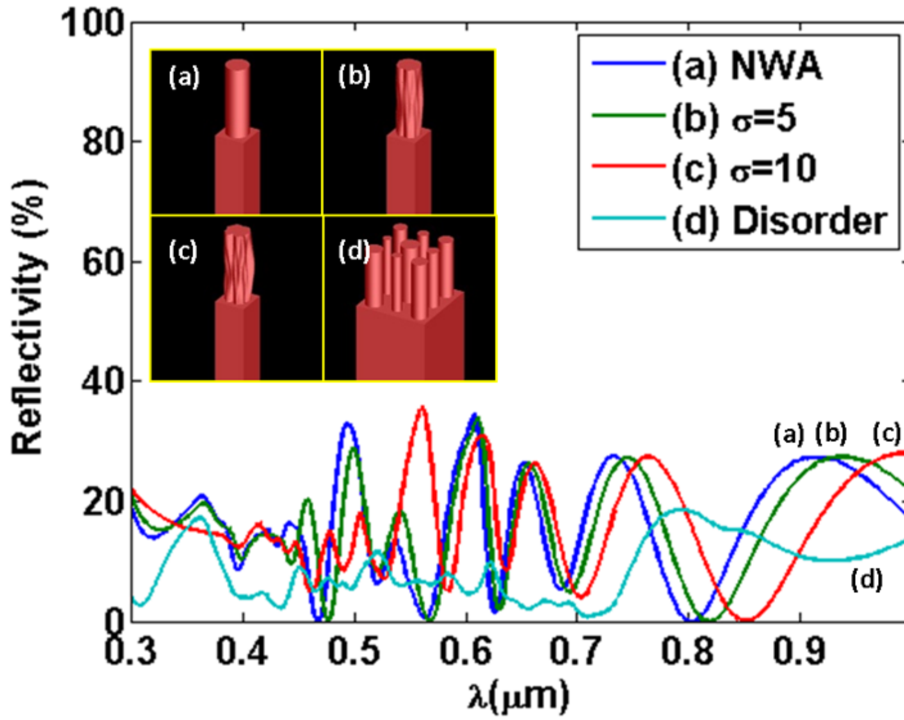

Figure 4.12: Reflectivity of SiNWs with varying roughness or disorder. (a): Perfect SiNWA; (b) and (c): rough SiNWAs and (d) is the pseudo disordered case.

transversal direction in x-y plane. This can be correlated to the red-shift observed in Fig. 4.11 as the radius of the perfect circular cross-section increases. Regarding the reflectivity intensity, there is generally minimal change because the overall volume of Si does not change. In the case of the pseudo disorder (d), which models the disorder observed when producing NWs using the MACE process, a reduction in the overall reflectivity intensity is noticeable. This is an expected consequence of the superposition of the different spectra associated to each radius shown in Fig. 4.11.

4.4 Conclusion

In this chapter we discussed the fabrication process, morphology and optical characterisation of SiNWAs. A single step etch recipe is established to fabricate controllable SiNWAs that are sub-micron in length. An optimised recipe for this found to be 0.06 M $AgNO_3$ and 2 M HF solution at a temperature of 50°C for 2 - 5 min. The cleaning step is also a critical part of the SiNWA etch. The NWAs are shown to be well aligned, with a uni-

form skyline. As the NWs increase in length, they bunch together due to van der waal forces. Optical measurements show a reduction in reflectivity of <5% over a broadband wavelength range (400 - 950 nm). Furthermore, longer NWs are shown to have greater light trapping. Optical modelling is also presented to better understand the reduction in reflectivity observed experimentally. It was found that a pseudo disordered SiNWA shows the greatest reduction in overall reflectivity intensity. This is due to the superposition of the different spectra as a result of confined modes associated to each radius in the array. The results of this work are published in [103].

5 Pyramid structures

At a micro-scale, pyramids have been a well acknowledged light trapping mechanism in silicon solar cells [21–23]. Random array of pyramids are commonly processed by exposing mono-crystalline silicon to an alkaline solution. Many different etchants can be used, including aqueous solutions of TMAH [22], NaOH [31] and KOH [114, 115].

5.1 Background

5.1.1 KOH Etching

Potassium Hydroxide (KOH) performs an anisotropic etch on silicon as it has higher etch rates for certain planes of the crystal structure. The etch rate in the $\langle 100 \rangle$ direction is far greater than the $\langle 111 \rangle$. When this occurs on a $\langle 100 \rangle$ orientated wafer, a random array of pyramids of a large range in size will form. This process is common in silicon micro-fabrication due to its low cost, controllability and repeatability. In order to mask the silicon from etching, common materials used include silicon dioxide and silicon nitride. The etch process is dependent primarily on the temperature, concentration of alkali solution and also the surface quality of the silicon [114]. In this chapter we discuss the in-house recipe established to fabricate an ordered array of pyramids with low density (i.e. 20 μm base size) to high density (i.e. 800 nm base size) by utilizing photo and e-beam lithography. The morphology and optical characterisation of these structures is also shown.

Crystal Planes

The etch rates using KOH solution are strongly dependent on the crystal planes of Si. This material has a lattice structure in tetrahedral arrangement, whereby each atom forms four identical covalent bonds with adjacent atoms. Various crystal planes, represented as Miller

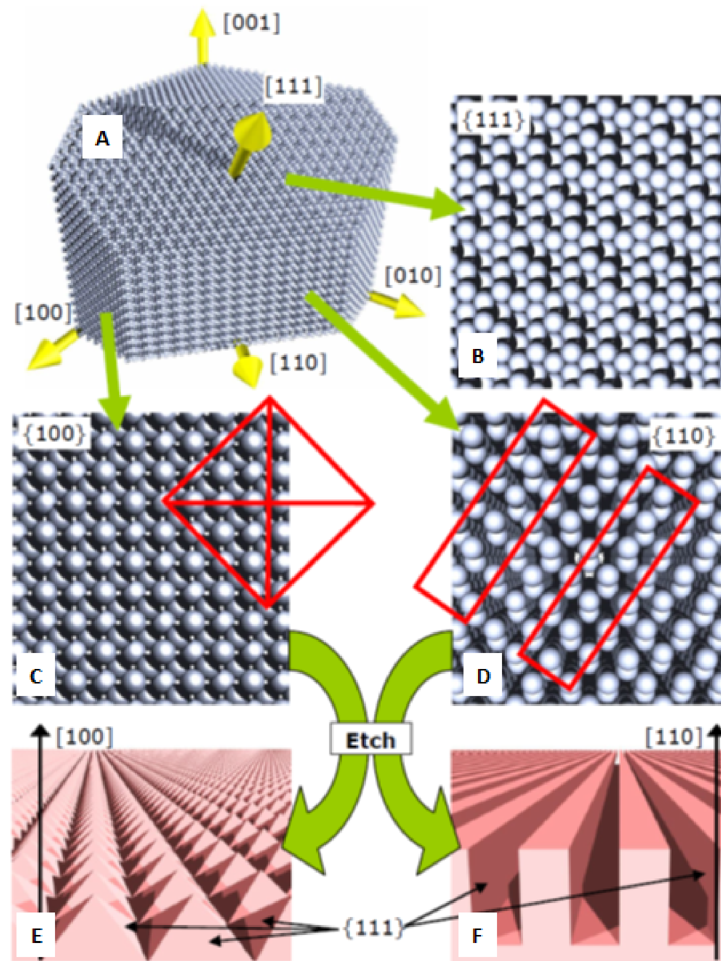

Figure 5.1: a) Si crystal with cubic lattice and the different lattice planes. b-d) Illustrate the density of the packed atoms for planes <111>, <110> and <100>. The densely packed atoms on the <111> direction means it etches much more slowly. e) Pyramid structures formed under crystallographic etching on a <100> substrate. f) Pillar structures formed under crystallographic etching on a <110> substrate [116].

indices, exists in this crystal lattice, shown in Fig. 5.1. As the etch rates are dependent on the crystal orientation, this etching process can result in well defined structures in silicon microfabrication - Fig. 5.1 shows the case for <100> and <110> wafers.

The etching process can be described by the equation

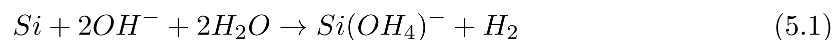

$$Si + 2OH^- + 2H_2O \rightarrow Si(OH_4)^- + H_2 \quad (5.1)$$

This describes firstly the hydroxide ion binding to an unpaired electron (from dangling bonds at the surface). This is then followed by the breakage of Si-Si bonds and the

consequent attachment of hydroxide ions, an endothermic process. The production of the H_2 bubbles is a drawback of this process, as the bubbles can act as a pseudo mask and cause roughness in the etching.

Table 5.1 summarises the etch rates for various crystal orientation. This shows that <110> etches faster than <100>, and <111> is by far the slowest of all the planes (negligible etch rates). The variance in etch rate is attributed to the surface of the planes, whereby <110> has a more uneven surface (i.e. greater number of dangling bonds per atom) than <100>, whilst <111> is atomically flat (i.e. tightly packed with only a single dangling bond per atom).

Table 5.1: A table summarising the etch rates on different planes at KOH conc. of 40%. The unit is $\mu m/min$ [117].

Crystallographic Orientation	Etch Rate
<100>	0.599
<110>	1.294
<111>	0.009

Concentration and Temperature

As the reaction is endothermic, the addition of temperature will increase the etch rate. However, an increased etch rate comes at the risk of rougher surfaces. Alongside temperature, a balance also needs to be found in the concentration of KOH. Whilst more silicon bonds will break with stronger KOH conc. , it will also consume more water (and release hydrogen gas), as seen in the aforementioned reaction process. As the amount of water reduces, the reaction is limited. Fig. 5.2 illustrates the impact of concentration and temperature upon the etch rates.

IPA

The addition of IPA has shown to enhance the smoothness of the etched surface, as well as improve the selectivity of the <100> direction. The use of IPA adds complexity to the etch recipe due its volatility. Long etches need much greater care to keep consistency, as the IPA will need to be refilled as it evaporates. The IPA also impacts on the etch rate.

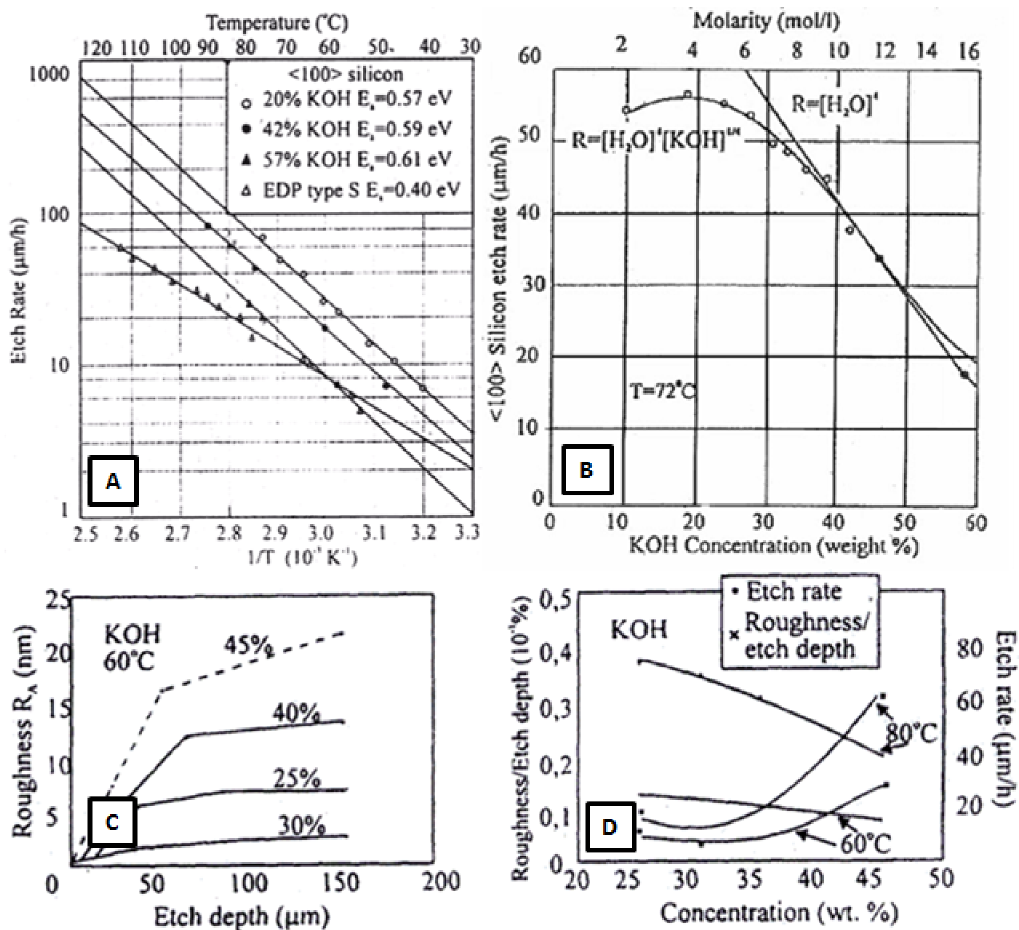

Figure 5.2: The impact of KOH conc. and solution temperature on etch rates and surface roughness of the pyramids formed. The graphs are taken from [118]. a) Etch rates increase with increasing temperature b)Increasing KOH conc. leads to a maximum etch rate. c) Increase in KOH conc. leads to increase in roughness. d) Increase in solution temperature leads to increase in roughness.

Masking

Two common masking materials are silicon dioxide and silicon nitride, the latter having the lower etch rate but at a higher cost. Another masking option is to highly dope the silicon wafer with boron, as a boron rich layer will reduce etch rates (although not to the extent of oxides and nitrides).

A common technique in silicon microfabrication is to form V grooves by aligninging rectangular openings with the <110> direction on a <100> oriented wafer. As the exposed <100> direction etch much faster than <111> direction, a resulting V groove arises. At this point, <111> planes have met and its 54.7 angle relative to the <100> plane is revealed - see Fig. 5.1. Since the <111> has a small etch rate, some under-etching occurs during fabrication.

5.1.2 Lithography

In order to fabricate the etch mask to form structures and patterns on the Si substrate, lithography processes are utilised. The aim of this process is to imprint a pattern written from a mask onto a light sensitive material. This can occur in several ways, the most common of which is photo-lithography which deals with feature sizes down to 2 μm. Imprinting at a nano-scale commonly occurs using EBL. Both these processes are tried in this project. The process for photo lithography is as follows.

The first step is to ensure that the surface of the substrate is suitable for processing. This includes ensuring a clean surface that the depositing materials can adhere to. The cleaning steps can be undertaken using the piranha etch process described in Chapter 4. In order to improve adhesion, the first method is to heat the substrate to ensure water is removed. The addition of primers can be used to produce a polar surface on the substrate. This can be of particular use when applying photo-lithography on SiO_2 surfaces (i.e. hydrophilic). Once the surface is prepared, photoresist is coated uniformly onto the substrate using spin coating. The parameters determining the thickness and uniformity of the coating are spin speed, acceleration and time of the spin. After the resist is deposited, the solvent is evaporated. This can be achieved using either a convection oven or a hot plate. The latter is preferred as it heats much faster and the heat transfer begins at the bottom of

the resist layer and work its way upwards, thereby thoroughly evaporating the solvent. The resist will thin during the bake and therefore will reduce the development time. The mask is positioned above the resist deposited substrate using a mask aligner. The type of mask used is dependent on the minimum feature size of the structures. Chrome masks provide better resolution over acetate masks, and the use of quartz glass over soda lime is justified when requiring better transparency for exposure. The mask can be placed into direct contact with the substrate or within proximity. The former projects a better image during exposure however this also risks more damage on the mask over time. The dose (time and intensity) of the exposure will determine the uniformity of the photo-activated resist. Photo-resist contains a photo active compound (PAC) in the group diazonaphtho-quinone-sulphonates (DNQ). When exposed to UV, the DNQ transforms into a carboxylic acid, accompanied by the release of nitrogen and the absorption of water. This increases its solubility in developer by several magnitudes. In order to optimise the lithography a balance should be found between exposure dose and development time. A low dose will require a large development time which can lead to erosion of unexposed resist. If the dose is too high, it can lead to undesired exposure of masked resist by scattering, diffraction and reflection.

E-Beam

The concept of EBL is similar to that of photo-lithography. Rather than UV light and a reticle, a focused electron beam is used to write the desired pattern on an electron sensitive material. The exposure by an electron beam will change the solubility of the resist and therefore selective removal will occur once immersed in a suitable solvent/developer. The use of a focused electron beam for direct-write lithography means that custom nano-scale patterns are achievable. However, the high resolution comes at the cost of low throughput.

5.2 Fabrication of Low Density Pyramids

5.2.1 Recipe

1. Clean the Si wafer (⟨100⟩, 1-10 Ω-cm, phosphorous) by first ultrasonicating in IPA for 2 min. This is then followed by a piranha etch (3:1, conc. H_2SO_4:30% H_20_2

solution) step for 15 min to remove small organic contamination.

2. Oxidation: Growth of approx. 330 nm thick SiO_2 (1100 °C, 1 h ramp, 4 h dwell time, 1 l h^{-1} O_2)

3. Lithography:

   a) Deposit a 1.7 µm thick film of S1813.

   b) Bake in oven for 30 min at 90 °C.

   c) Expose for 40 s at 7 mJ cm^{-2}.

   d) Develop in MF319 for 15 s - 30 s.

   e) Descum if needed.

   f) Oxide removal by plasma etch for 20 min (25 sccm Ar, 25 sccm CHF_3, 30 mTor, 20 °C, 200 W) .

   g) Remove resist using acetone.

4. KOH etching: Heat water bath to 80 °C. Mix 200 g KOH in 200 ml HPLC water, then add 20 ml IPA into beaker and place in water bath. 40% KOH + 10% IPA. Once KOH solution is at 80 °C place sample in etchant for desired time. Finally, rinse in H_2O.

5.2.2 Results

Fig. 5.3 illustrates the resist mask produced from the lithography steps described. These masks are used to etch the array of oxide squares and can be defined by their width (W_{ox}) and gap (W_{gap}). This figure illustrates $W_{ox} = 20\ \mu m$ with $W_{gap} = 20\ \mu m$, $W_{ox} = 10\ \mu m$ with $W_{gap} = 10\ \mu m$, $W_{ox} = 10\ \mu m$ with $W_{gap} = 5\ \mu m$ and $W_{ox} = 5\ \mu m$ with $W_{gap} = 5\ \mu m$. It can be seen that for this recipe the corners in the photoresist are rather rounded than sharp and as such the oxide masks formed for the case of $W_{ox} = 5\ \mu m$ is more circular than square. The rounding is due to over-development of the resist. All the square array sizes are fabricated from one reticle and produced on the same wafer. Therefore, to maximise the yield, a trade off in development time is needed. Under-development will lead to poor formation of squares and gaps for all sizes, whilst over-development leads to a greater yield

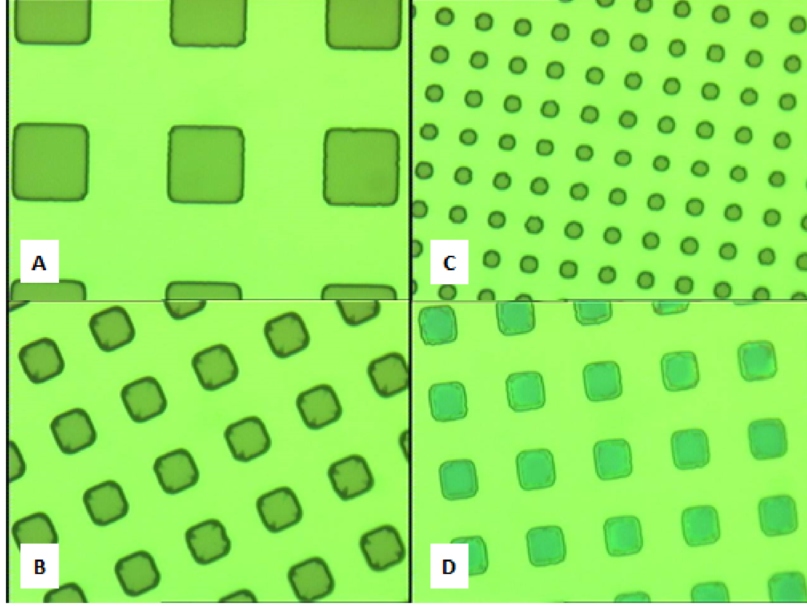

Figure 5.3: Resist mask on the substrate post-lithography. a) $W_{ox} = 20\mu m$ b) $W_{ox} = 10$ μm c) $W_{ox} = 5\mu m$. d) oxide mesa for the case of $W_{ox} = 10$ μm, once the resist is removed.

of squares but with rounded corners. It is also possible to improve the yield by under-developing and then using a descum recipe to remove small amounts of resist to sharpen edges. The latter is used with a descum recipe of: 60 sccm O_2, 50 mTor, 20 °C, 100 W) for 2 minutes. Low pressure is used to maintain straight particle paths ensuring features remain consistent.

Once the oxide is etched, the resist mask can be removed. This is generally achievable by placing the wafer in acetone. However, if the resist still remains then heating the wafer in a 1165 solution is the next step. The final step is to use an asher whereby plasma etching is used. Fig. 5.3 shows the mask with resist and the resulting oxide mesas.

Fig. 5.4 shows SEM images of pyramids formed from $W_{ox} = 20$ μm, $W_{ox} = 10$ μm and $W_{ox} = 5$ μm. The parameters which define these pyramids are the KOH etch time (t_e), the resulting length (L_p), base width (W_b) and top-face width (W_t). The parameters of the different pyramid array are summarised in Table 5.2.

The pyramids in Fig. 5.4 confirm the presence of crystallographic etching in KOH solution. The higher etch rate in the <100> direction has etched material away perpendicular to the flat bulk surface. However, the lower etch rate of <111> direction has acted as an etch stop and consequently formed pyramidal structures with its various planes observable.

Table 5.2: Parameters defining the pyramid geometry for a given oxide mask size and etch time for the low density mask.

W_{ox}(µm)	t_e(min)	W_b(µm)	W_t(µm)	L_p(µm)
20	10	27.8	11.5	9
10	10	18.7	3.9	10.1
5	5	6.9	1.1	3.8

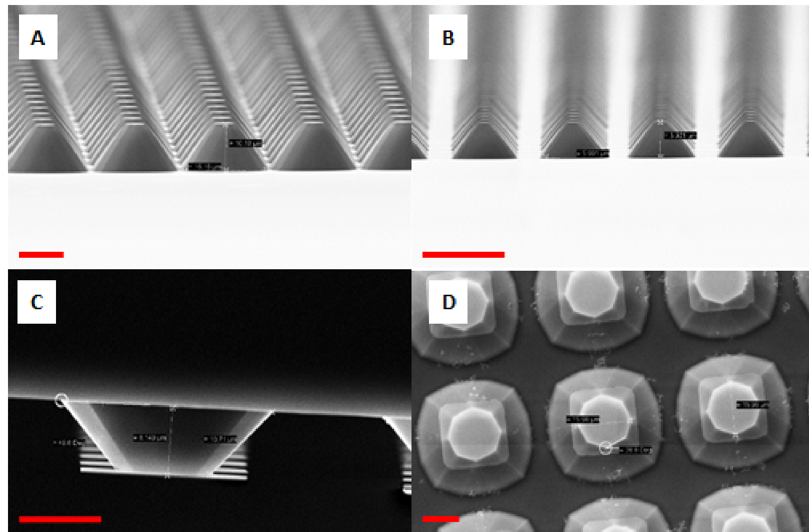

Figure 5.4: SEM image of the pyramids formed after crystallographic etching, whereby $W_{ox} = 10\ \mu m$ has the most dense array. a) $W_{ox} = 10\ \mu m$ b) $W_{ox} = 5\ \mu m$ c) $W_{ox} = 20\ \mu m$ including the remaining oxide masks post etch. d) Top view of $W_{ox} = 20\ \mu m$.

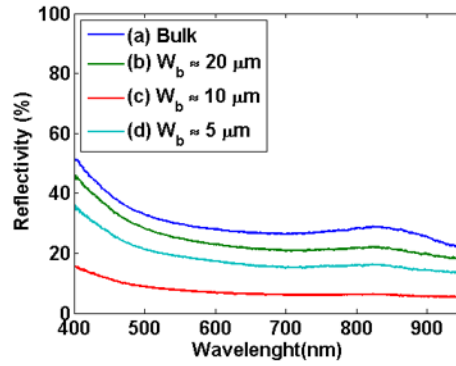

Figure 5.5: Optical measurements for varying low density pyramid arrays.

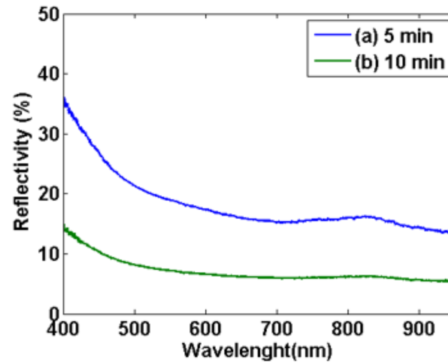

Figure 5.6: Optical measurements for different depths of a pyramid formed with W_{ox} = 5 μm.

The pyramids are uniform in size and form a periodic array due to the oxide masks. From this figure the oxide mask can be seen and a clear under-cut is present. The under-etch equates to 2 μm for the case of W_{ox} = 20 μm.

Fig. 5.5 shows the optical measurements for the fabricated pyramids. The presence of pyramids reduces the reflectivity compared to that of bulk Si. A significant reduction is observed for W_{ox} = 10 μm, however for the case of W_{ox} = 20 μm and W_{ox} = 5 μm it is surprisingly large. This can be explained when referring to Fig. 5.4. This shows that whilst an etch time of 10 mins produces a compact array of pyramids for the case of W_{ox} = 10 μm, it produces larger gaps for the case of W_{ox} = 20 μm. A similar case is observed for W_{ox} = 5 μm pyramids etched for 5 mins.

Fig. 5.6 shows the optical results W_{ox} = 5 μm pyramids etched for 5 mins and 10 mins. Achieving a deeper etch and producing a more compact pyramid array considerably reduces reflectivity.

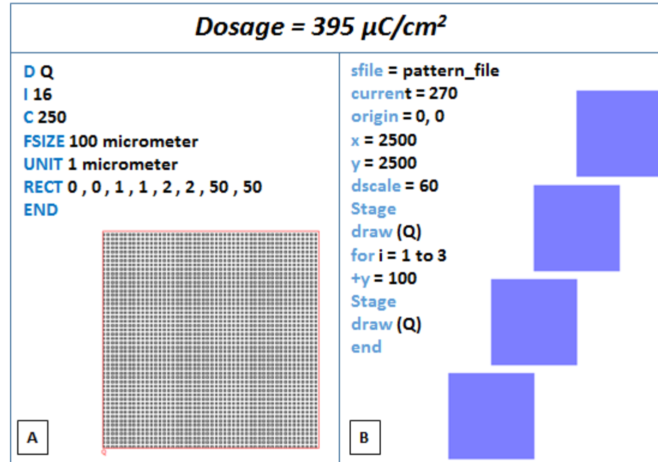

Figure 5.7: a) Example pattern file b) Example control file. The overall dosage used to write the fields is determined by the dwell time, C, and incrementation, I, in the pattern file, and the beam current in the control file.

5.3 Fabrication using E-Beam Lithography

To increase the density of pyramids with the aim of producing lower reflectivity and increase junction area, an EBL approach was also tested. The first step is to use an exposure control program for designing the mask and expose with a XENOS pattern generator. This is achieved with two files, a control file and a pattern file. The pattern file consist of the field data (i.e. shapes and geometry) as well as the dwell time (i.e. the time in *ns* for which a single point is exposed) and incrementation (i.e. determines how many points are exposed). This pattern file is then used in a control statement to write onto an electron sensitive material. The control file will determine the positioning of each pattern file and the value of current used (calibrated with measurements taken from the SEM using a Faraday cup and pA meter). An example pattern and control file with its output is shown in Fig. 5.7. The exposure dosage, which along with the development time of the resist, will determine the quality of pattern. This dosage value is a function of dwell time, incrementation and the beam current. The dwell time and incrementation will also determine the exposure time.

5.3.1 Recipe

The recipe for implementing the EBL is as follows:

1. Grow SiO_2 (1050 °C , 1 hr ramp, 4 hr dwell , 1 L hr^{-1} O_2, approx. 200 nm thick)

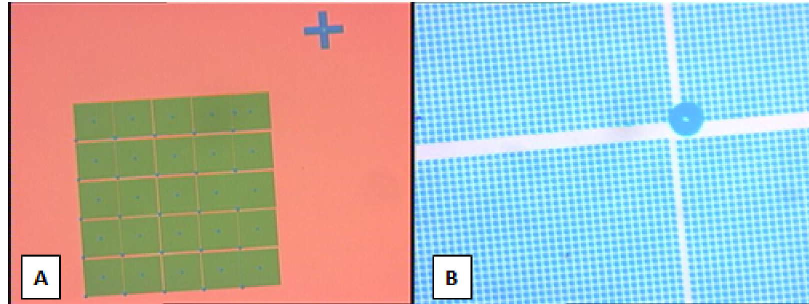

Figure 5.8: a) Oxide mask , with $W_{ox} = 1\ \mu m$, fabricated after e-beam lithography. b) Gaps occur between the writing fields, as well as unwanted spots in the corner and centre of the fields.

2. Deposit thin film PMMA layer

   a) Clean substrate using IPA sonication followed my oxygen plasma in system 80 (100 sccm O_2 100W, 5 sccm Ar, 200W)

   b) Dehydrate in oven at 150 °C for 5 mins

   c) Spin-coat PMMA (approx. 100nm): 500 rpm, 500 rpm s^{-1}, 10 s followed by 5000 rpm, 500 rpm s^-1, 50 s

   d) Bake on hotplate for 30 mins at 170 °C

3. E-beam exposure (dosage approx 300 Ccm^-2)

4. Develop in MIBK/IPA in a ratio of 1:3 for 2 mins

5. Evaporate 40 nm thickness of Al onto sample

6. Lift off using:

   a) Soak in acetone over 24 hrs

   b) Sonication until lift off complete (approx. 20mins)

7. Oxide etch in system 80 (25 sccm CHF_3, 25 sccm Ar, 2 sccm O_2, 200 W for 10 mins)

8. Al etch (use HCL to strip off any remaining Al)

5.3.2 Results

Fig. 5.8 shows the oxide pattern, for $W_{ox} = 1\ \mu m$, for post lithography steps. From this we can see the array of squares, with distinct dots at the centre and corner of each field.

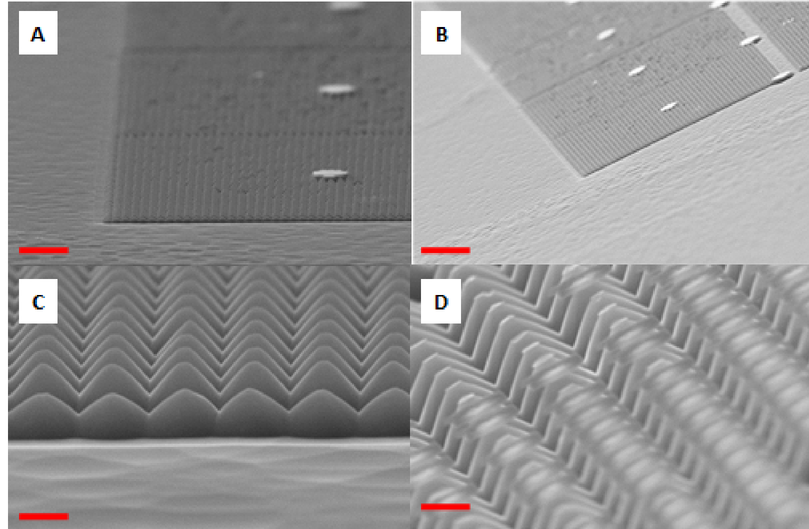

Figure 5.9: SEM image of pyramid array ($W_{ox} = 1$ μm, $t_{etch} = 2$ min) using oxide masks from e-beam lithography. a) Array of densely ordered pyramids and mesas formed from over exposed resist b) The gaps between the writing fields are observed in the pyramid array c) Close up of densely ordered pyramids d) Oxide masks on pyramid array. The scale bar is 10 μm for a and b, and 1 μm c and d.

Clear gaps are also apparent between the fields. Fig. 5.9 shows the formation of pyramids using this oxide pattern and the presence of the oxide masks after etch with $t_{etch} = 2$ min. The gaps present are due to mechanical stability of the stage when writing a new field. It should be noted that this error is constant and therefore the gap size between fields is the same. In order to reduce this error an offset, Y_δ, can be added to the control file such that alignment between the fields improve. Fig 5.10 illustrates the pattern produced from 6 different control files. It is shown that by inserting an $Y_\delta = 6$ μm, for a field size of 100 μm^2, the gaps are removed.

The dots observable in the above figures are as a result of over exposure by the e-beam during writing. The beam begins its writing of the field at the centre and ends at the corner. The excessive dwell time at these points lead to over-exposure and poor lithography. This is an issue usually solved using a beam blanker that can prevent exposure during these steps. In the absence of a beam blanker, an attempt at reducing the dot size was made by lowering the effective exposure dosage. Fig. 5.11 shows the results of this. As can be seen, the centre dot has now been removed however the corner dot remains. This suggests the dwell time is longer at these positions.

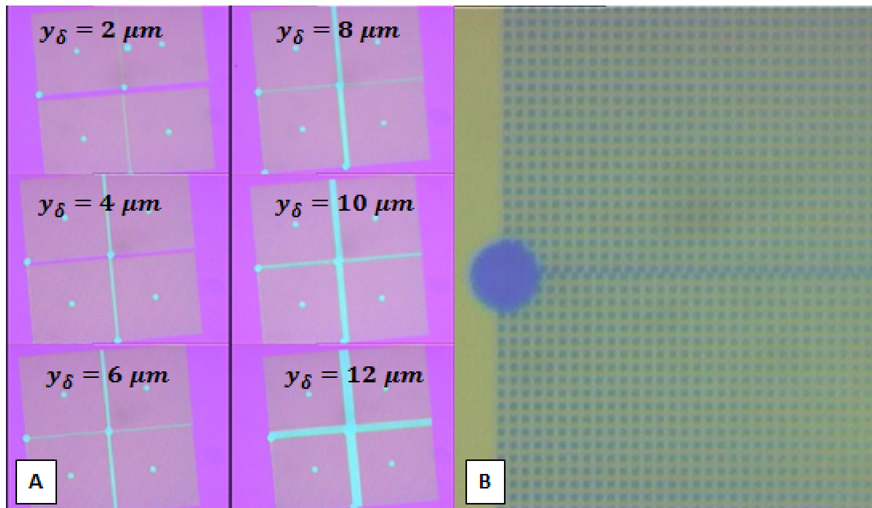

Figure 5.10: a) 6 different oxide mask arrays, whereby the writing fields are shifted (by incorporating offsets, Y_δ, in the control file) to counter stage movement error. b) Successful stitching of the writing fields achieved by an $Y_\delta = 6\ \mu m$.

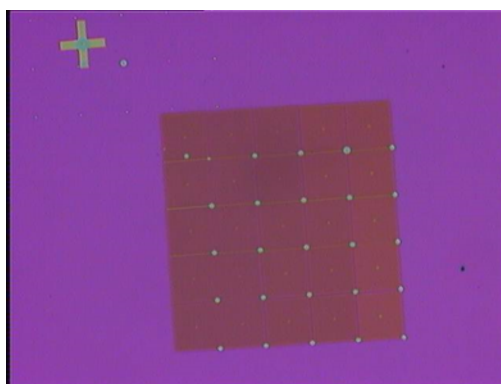

Figure 5.11: Oxide masks under e-beam lithography with the unwanted centre spot of the array removed. This was achieved by lowering the beam dosage.

The exposure time to write the pattern observed in Fig. 5.11 is approx 2 hrs. This results in a very low throughput. Furthermore, with the minimum area needed for optical measurements being at a cm scale, EBL is inappropriate and optical lithography will be applied.

5.4 Fabrication of High Density Pyramids

Due to the low throughput of e-beam lithography as well as the inability to remove dwell spots in the array in our equipment, photolithography is used to produce the high density pyramids. The differences in this lithography process compared to the production of low density pyramids are the reticle type, contact type, and the addition of a lift off process. The use of a quartz mask and a vacuum contact reduces the light scattering, critical for smaller feature sizes. Positive resist is used in-conjunction with a lift-off process. This reduces errors seen with development as less surface area needs to be developed.

5.4.1 Recipe

The method we use for defining the periodic hybrid structures is as follows (see Fig. 5.12):

1. Clean the Si wafer (<100>, 1-10 Ω-cm, phosphorous) by first ultrasonicating in IPA for 2 min. This is then followed by a piranha etch (3:1, conc. H_2SO_4:30% H_20_2 solution) step for 15 min to remove small organic contamination.

2. Oxidation: Growth of approx. 150 nm thick SiO_2 (1050 °C, 1 hr ramp, 4 hr dwell time, 1 L hr^{-1} O_2)

3. Lithography: Deposit a 500 nm thin film of S1813 layer. Bake on hotplate for 1 min at 115 °C. Expose for 9 s at 7.2 mJ cm^{-2}. Develop in MF319 for 25 s. Evaporate 80 nm thickness of Cr onto sample. Lift off the photoresist by soaking in acetone and then sonication for 10 min. Plasma etch for 3 min (25 sccm Ar, 25 sccm CHF_3, 30 mTor, 20 °C, 200 W) and then buffered oxide etch (BOE) (6:1 , 40% NH_4F:49% HF) for approx. 20 s to produce the oxide mask. Use Cr etchant (1:1:8, $H_8N_8CeO_{18}$, HNO_3, H_2O) to remove the chrome mask.

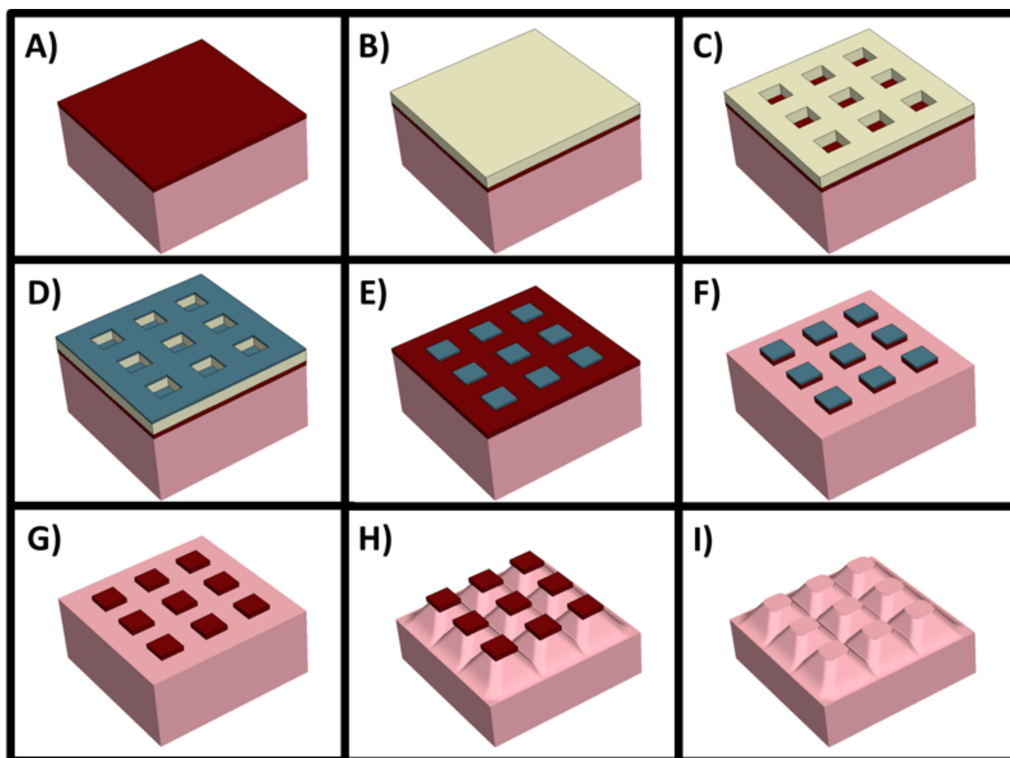

Figure 5.12: Schematic diagram of the process flow used to fabricate the dense array of pyramids. A) oxidation, B) deposit resist, C) expose and develop using mask, D) deposit Cr, E) strip resist, F) etch oxide, G) remove Cr, H) KOH etch of Si, I) BOE of oxide layer.

4. KOH etching: Heat water bath to 80 °C. Mix 200 g KOH in 200 ml HPLC water, then add 20 ml IPA into beaker and place in water bath (40% KOH + 10% IPA). Once KOH solution is at 80 °C, dip sample into BOE for 3 s and then place sample in etchant for desired time. Finally, rinse in water.

5.4.2 Results

Morphology

Figure 5.14 shows the SEM of the pyramid arrays formed from 3 different oxide masks of varying density. The parameters of the different pyramid array is summarised in Table 5.3.

In all cases the oxide mask is under-etched, resulting in multi-faceted pyramids. The effect of the under-etch is larger for the denser pyramid array, resulting in sharp tips rather than flat-faced tops. The quality of the pyramid formation is dependent on the quality of

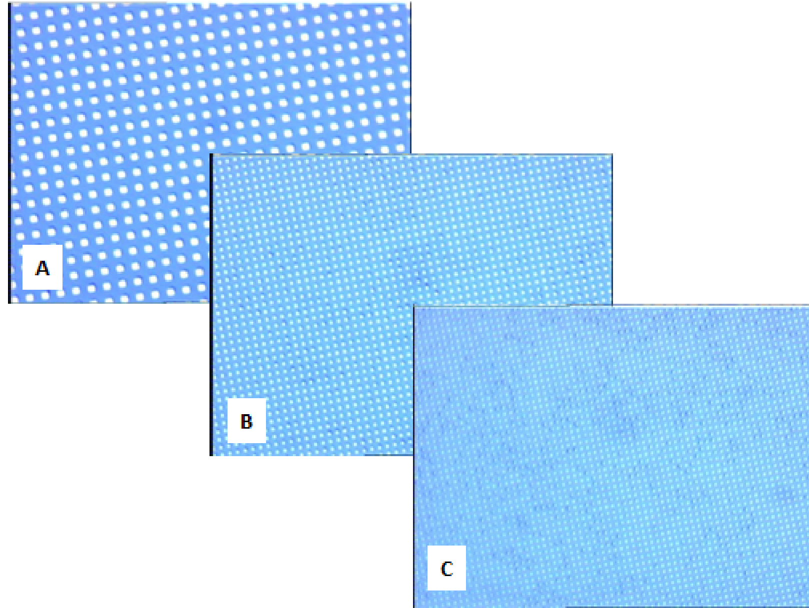

Figure 5.13: Oxide mask after lithography of high density array. a) W_{ox} = 2 μm b) W_{ox} = 1 μm c) W_{ox} = 0.8 μm.

Table 5.3: Parameters defining the pyramid geometry for a given oxide mask size and etch time for the high density mask.

W_{ox}(µm)	t_e(min)	W_b(µm)	W_t(µm)	L_p(µm)
2	2	3.7	1.1	2.15
1	2	2	0.1	1.6
0.8	1	1.5	0.3	0.9

the surface prior to etching. The crucial steps included a buffered HF dip prior to etching as well as the presence of IPA in the alkaline solution.

Fig. 5.15 shows the optical measurements for the fabricated pyramids. The presence of pyramids reduces the reflectivity compared to that of bulk Si. A significant reduction is observed in all cases, whereby increasing density and compacting the pyramids reduces reflectivity further.

5.5 Conclusion

In this chapter we discussed the fabrication of silicon pyramids arrays using KOH etching. Oxide mesas are used to mask from KOH etch, and are implemented through both photolithography and EBL. The quality of the pyramid surface is improved via the addition IPA in the KOH solution, as well as a quick buffered HF dip prior to etching. An under-cut of the oxide mask is observed in the morphology of the pyramids. Optical measurements showed the pyramids reducing reflectivity compared to bulk Si. It is shown in both the cases for low and high density pyramid arrays that increasing density and compacting the pyramids reduces reflectivity further. Whilst sub-micron pyramid arrays were achieved through both EBL and photolithography, the latter proved more successful due to better throughput.

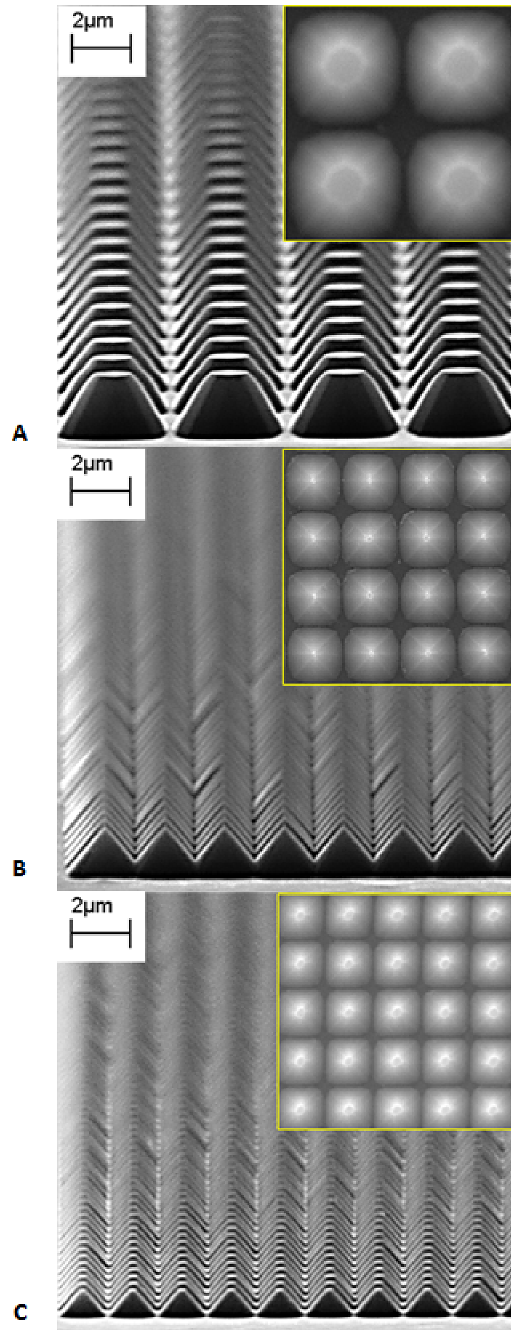

Figure 5.14: SEM image of high density pyramid arrays. a) W_{ox} = 2 µm b) W_{ox} = 1 µm c) W_{ox} = 0.8 µm

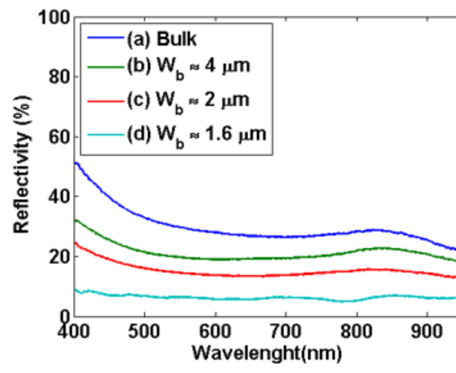

Figure 5.15: Optical Measurements for varying high density pyramid arrays.

6 Hybrid structures

A combination of periodic pyramids and nanowires is used to form a hybrid structure that will have the two fold benefit of increased light absorption and junction area. Instead of using pyramids randomly organised via alkaline etching of bulk silicon, we fabricate a denser and periodic array using oxide masks and optical lithography. In this work, the pyramids periodicity varies from 4 μm down to 1.6 μm, using an array of square oxide masks with widths of 2 μm down to 800 nm. Vertical NWAs are then etched onto these pyramids using MACE to reduce the reflectivity further. The fabrication process of the hybrid structure is scalable and can be cost effective.

The fabrication of the hybrid structure consists of first, fabricating an array of pyramids using a combination of photo-lithography and alkaline etching, followed by a MACE process to fabricate a NWA on top. Successful hybrid textured silicon surfaces have been fabricated using a combination of an alkaline etch to form a random pyramid array, followed by RIE to form the NWA [119] as well as using MACE etching [26, 120–122]. Reflectivity of less than 3% in the wavelength range of 300 - 1000 nm have been reported from this texture. In this work, photo lithography and an oxide mask is used for the alkaline etching of a periodic, dense array of pyramids with a single step MACE etched NWA on top.

6.1 Simulated Optical results

Fig. 6.1 compares the reflectivity of (a) bulk, (b) rough, quasi random SiNWAs, (c) periodic pyramid, and (d) hybrid structure. The pyramids used in these structures have a base width of 2 μm and a height of 1.6 μm. The reflectivity of the SiNWA is lower than the pyramid array, in accordance with literature [119,120]. The pyramid structure behaves like a standard broadband absorber [123] as the pyramid geometry provides a continuous

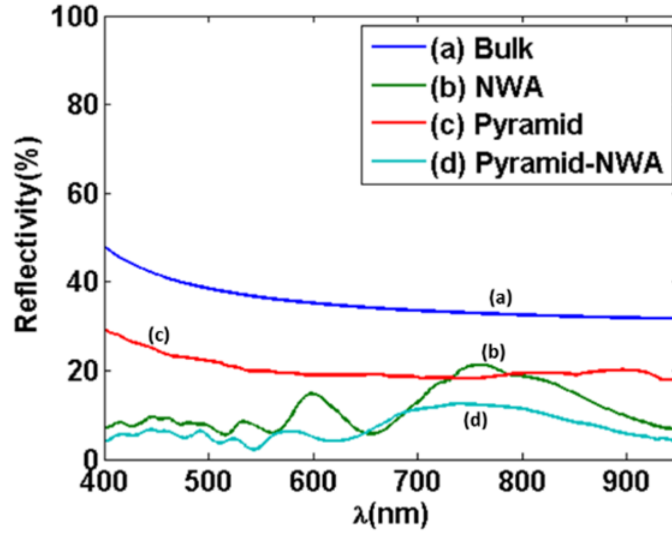

Figure 6.1: Reflectivity of bulk, pyramids, NWA and pyramids-NWA.

change in effective permittivity, and thus, tapers the impedance from that of free-space to bulk Si. In comparison, the impedance of the SiNWAs can be understood as a single step converter, which provides an intermediate impedance between that of free-space and bulk Si. In the hybrid structure an additional drop of the reflectivity is observed due to the combined impedance matching effect.

In Fig. 6.2 the total carrier generation rate at the middle cross-section plane for bulk, SiNWA, pyramids and hybrid structures is given. This is an integration of the power absorption due to an AM1.5 solar spectrum illumination. For a bare Si substrate, the absorption profile is uniform along x, has a maximum at the air-Si interface and decays along z, the propagation direction. When SiNWAs are introduced, most of the absorption happens in the SiNWAs because of the waveguide modes, but still significant absorption occurs in the Si substrate. For the pyramid case, in addition to the high carrier generation at the air-Si interface, an absorption hot spot arises at the centre of the pyramid. This absorption profile can be explained by the lens effect of the pyramid. The convex profile of the pyramid emulates a lens, concentrating the incoming rays into a focal region. Finally, for the hybrid structure, a superposition of the absorption profiles displayed by the SiNWAs and pyramids alone is observed. The high concentration of absorption in the SiNWAs should be seen as beneficial for solar cells, as the carrier generation will be high near the

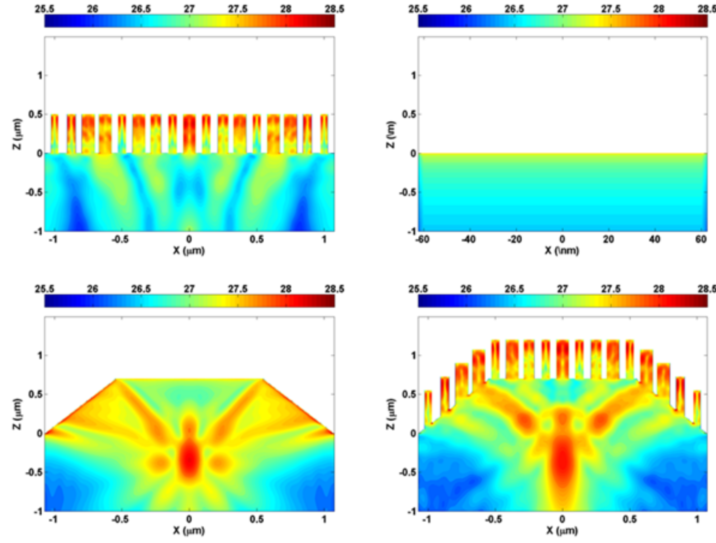

Figure 6.2: Spatial map of carrier generation rate ($m^{-3}s^{-1}$), in logarithmic scale, of (a) rough, quasi random NWA, (b) bulk, (c) pyramids and (d) pyramids-NWA.

junction area.

6.2 Morphology

Fig. 6.3 shows the results of NWA etching for 5 mins on pyramids with W_{ox} = 20 μm. It shows that the pyramid shape is sustained with NWA formation on the surface. The NWA etching appears uniform on the top face however the height is varying on the sides of the pyramid with minimal etching at the edges of the base. Furthermore, the bunching of NWA is prevalent throughout.

Fig. 6.4 shows a cross-sectional view of hybrid structures with W_{ox} = 2 μm. The NWs etch into all faces of the pyramids and thereby creates a NWA surface whilst pushing the pyramid geometry deeper into the substrate. This is due to NWs etching perpendicular to the <100> direction. The overall size of the hybrid structure is the same as the pyramid prior to MACE. The NWAs etch with a uniform skyline and are well aligned. However, the length of the NWA differs on the hybrid structure and the bulk region despite having the same etch time. The length of NWA on bulk is $L_{NWA} \approx 1$ μm, whilst on the hybrid structures only $L_{NWA} \approx 500$ nm.

Fig. 6.4, 6.6 and 6.7 show the top view of the hybrid structures for W_{ox} = 2 μm, W_{ox} = 1 μm and W_{ox} = 0.8 μm respectively.

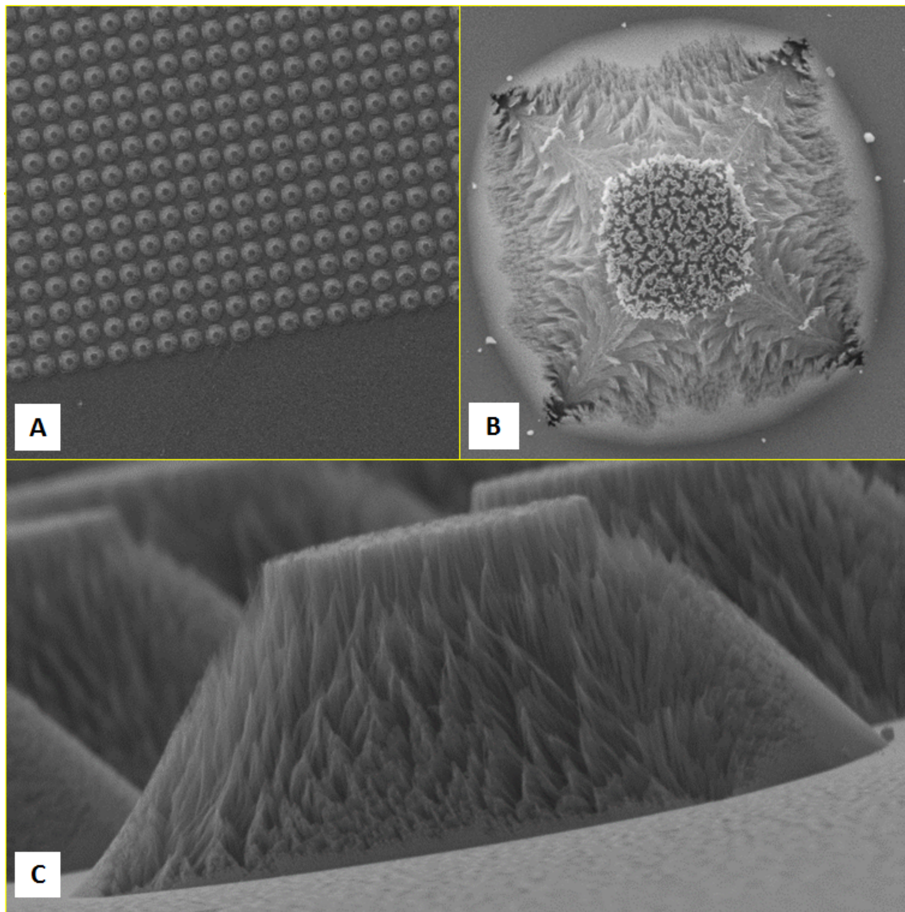

Figure 6.3: SEM image of a NWA on $W_{ox} = 20$ μm pyramids. a) Top view of array b)Top view close up of pyramid c) Side view close up of pyramid.

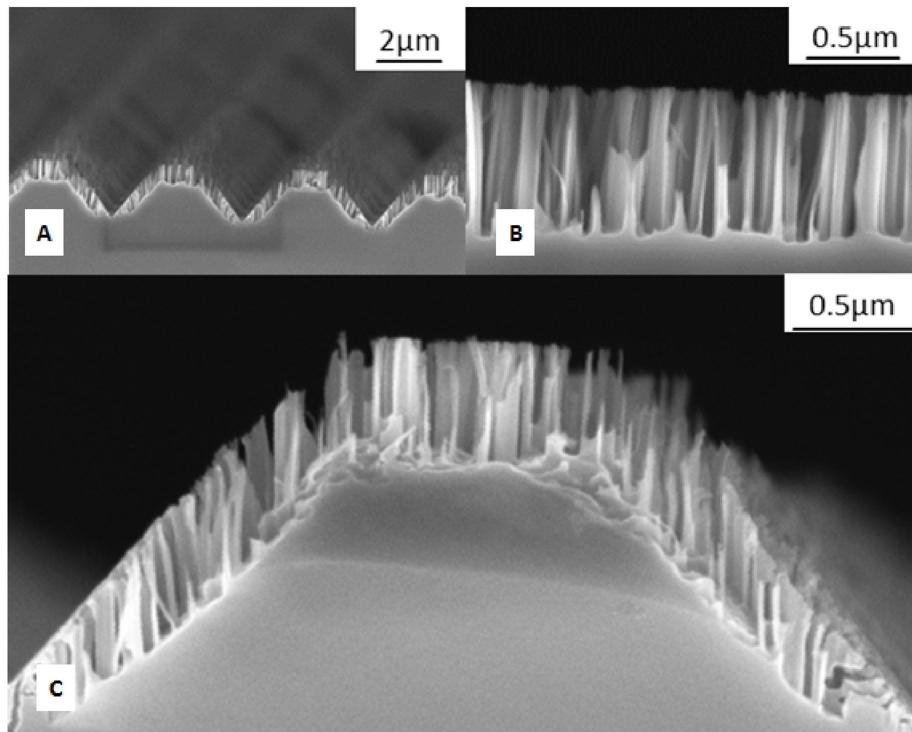

Figure 6.4: SEM image of a NWA on pyramids, with $W_{ox} = 2\ \mu m$, and NWA on bulk. a) Cross-section view of pyramid-NWA b) Cross-section view of NWA on bulk Si c) Close up cross-section view of pyramid-NWA. The NWAs etch with a uniform skyline and are well aligned.

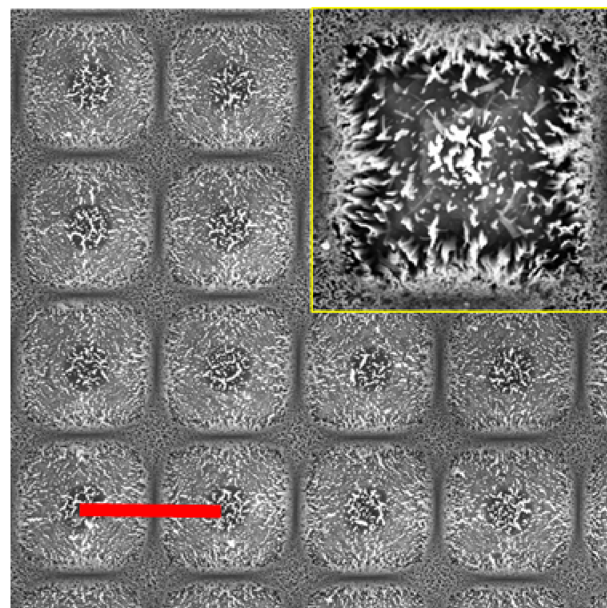

Figure 6.5: SEM images illustrating NWA formation on $W_{ox} = 2\ \mu m$ pyramids, the scale bar is $4 \mu m$. Inset: close-up view of singular pyramid-NWA.

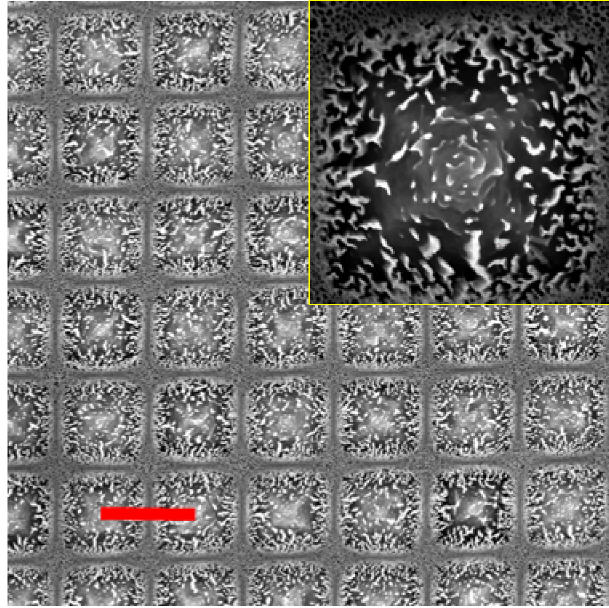

Figure 6.6: SEM images illustrating NWA formation on $W_{ox} = 1\ \mu m$ pyramids, the scale bar is $2 \mu m$. Inset: close-up view of singular pyramid-NWA.

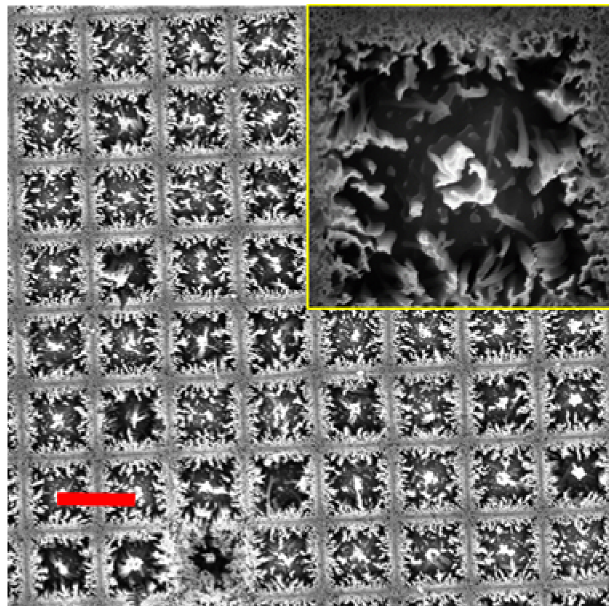

Figure 6.7: SEM images illustrating NWA formation on $W_{ox} = 0.8\ \mu m$ pyramids, the scale bar is $1.6 \mu m$. Inset: close-up view of singular pyramid-NWA.

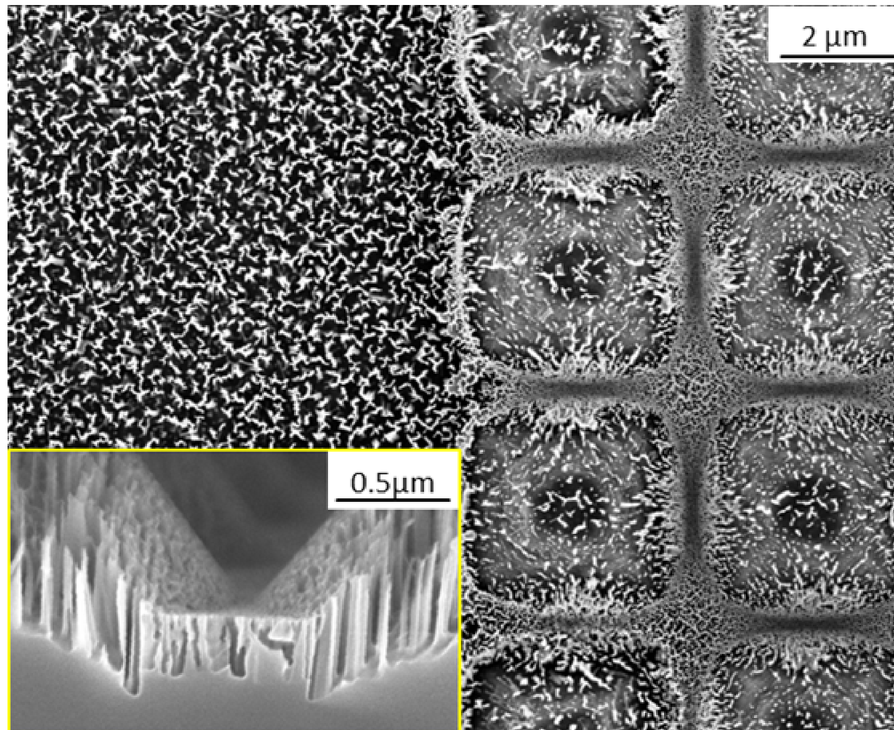

Figure 6.8: SEM image comapring NWA fomration on bulk, pyramids, and a close up view inbetween pyramids (inset). This shows that the valleys in-between the pyramids are more porous Si than NWAs.

Fig. 6.8 shows the top view of the NWA formation on the hybrid and bulk region. It also illustrates the side view at which two hybrid structures intersect. This shows that the valleys in-between the pyramids are more porous Si than NWAs. This indicates a different Ag nucleation dynamics in the presence of surface structuring.

Fig. 6.9 shows the formation of hybrid structures fabricated via 1 min MACE process, thereby observing the predominant effects of nucleation. We increase the area in-between the hybrid structures by applying a short KOH etch time to our least dense pyramid array. Whilst the bulk region contains dendrites of a large variety of sizes, the valleys in-between the hybrid structures contain minimal dendrites. The predominant dendrite formation in the hybrid region occurs on the top face of the pyramids, and the larger dendrites are formed by emerging with other dendrites formed on the top of adjacent pyramids. The reduced dendrite formation means less nucleation is occurring in the valleys and thus explains the formation of porous Si rather than NWA. Furthermore, the reduction in dendrites is also suggested as the cause for reduced etch rates in the hybrid structures. It has been reported that a lower surface area of dendrites results in inefficient capturing of

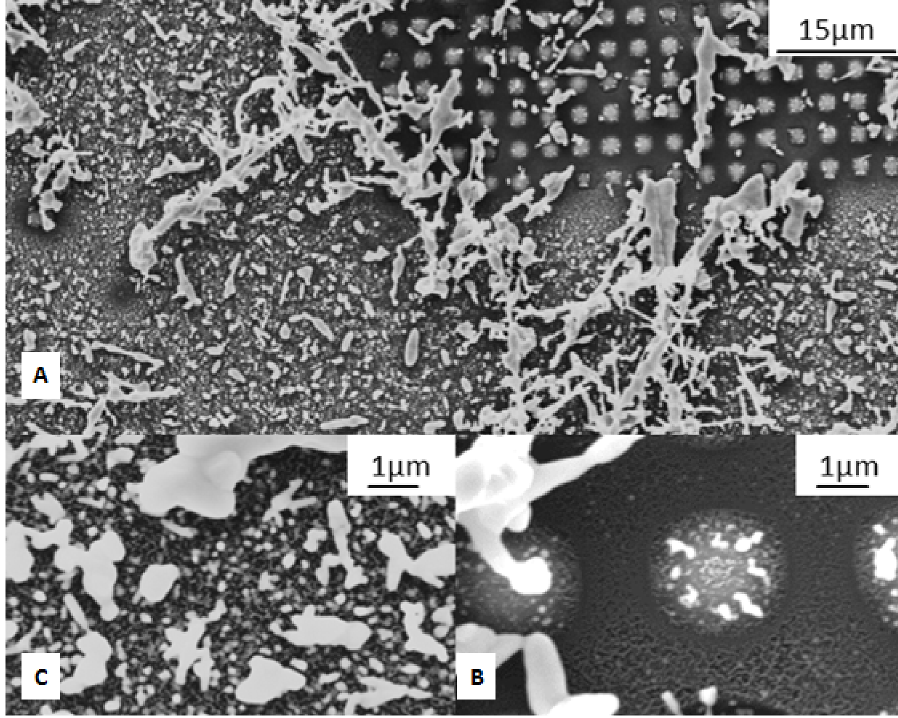

Figure 6.9: SEM images comparing dendrite formation on bulk-NWA array and pyramid-NWA array. Whilst the bulk region contains dendrites of a large variety of sizes, the valleys in-between the hybrid structures contain minimal dendrites. a) Top view of dendrites on bulk-NWA array and pyramid-NWA array b) Close up of dendrites on bulk-NWA c) Close up of dendrites on Pyramid-NWA.

silver ions for the redox reaction [124].

6.3 Experimental Optical Measurements

Optical measurements were taken on pyramids of $W_b \approx 4\,\mu m$ and $L_p \approx 2\,\mu m$, $W_b \approx 2\,\mu m$ and $L_p \approx 1.5\,\mu m$ and $W_b \approx 1.6\,\mu m$ and $L_p \approx 1\,\mu m$, and also their hybrid structures with $L_{NWA} \approx 500\,nm$.

Fig. 6.10 shows the experimental reflection spectrum for the four cases discussed in section 6.1, namely (a) bulk Si, (b) SiNWAs, (c) pyramid array, and the (d) hybrid structure. By comparison against the numerical results shown in Fig. 6.1, the agreement is excellent. As predicted, the lowest reflectivity is exhibited by the hybrid structure, whose benefit compared to SiNWAs is conspicuous for larger wavelengths. The lower reflectivity observed experimentally for SiNWAs and the hybrid structure stems from the larger heterogeneity of the fabricated samples in terms of radius size, which cannot be fully modelled

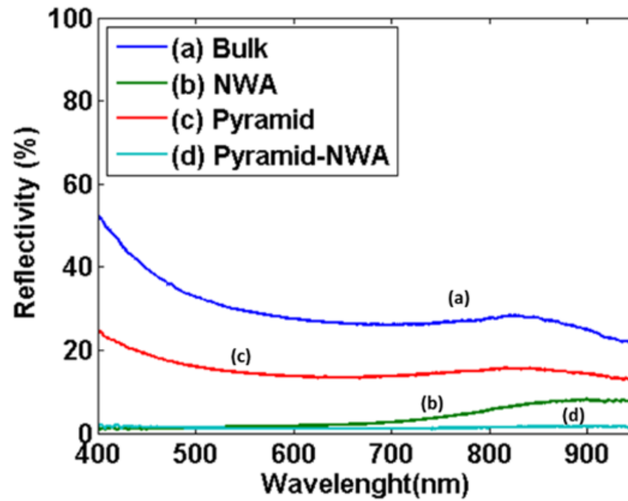

Figure 6.10: Experimental reflectivity of (a) bulk, (b) NWA, (c) pyramids and (d) pyramid-NWA structures.

because of computational limitations [125].

Finally, Fig. 6.11 shows the reflection spectrum for (a) SiNWAs and (b, c, d) hybrid structures with varying pyramid size, showing that increased density leads to reduced reflectivity. In accordance with Fig. 6.10 and the simulations, Fig. 6.1, all hybrid structures outperform SiNWAs by repressing reflection in the higher wavelength range. Notice that the higher density hybrid structures have a shallower profile. This makes them more attractive for PV as the junction depth is more optimal. The better performance of the 2 μm and 1.6 μm periodic hybrid structures with respect to the 4 μm periodicity is a result of the improved tapered impedance matching. The 4 μm periodic hybrid array fails to change the impedance smoothly, from that of free-space as a result of its flat rather than pointed top.

6.4 Electrical response

The photovoltaic characteristics of the different designs are modelled using the TCAD package, Synopsys Sentaurus[1] [100, 126–128]. The structure is generated by simulating the silicon fabrication processes that include isotropic/anisotropic deposition and etching. The initial substrate is a ⟨100⟩ silicon slab, 20 µm thick and boron doping concentration

[1]See chapter 2 for more details on this software package

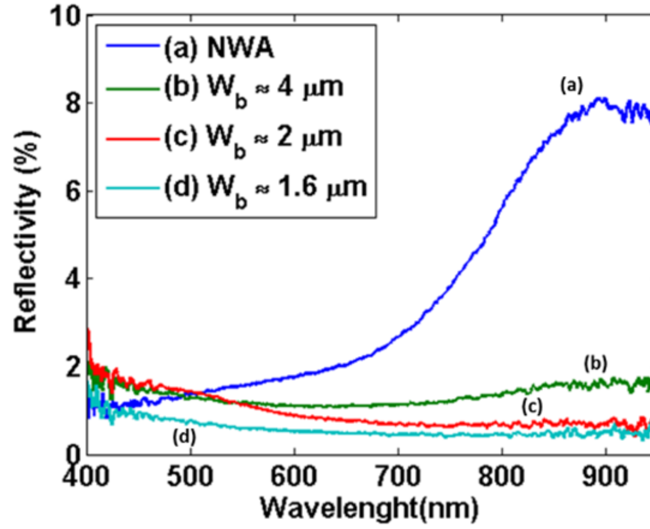

Figure 6.11: Experimental reflectivity of NWA and different density of hybrid structure.

(conc.) of $1 \times 10^{15}\,\mathrm{cm}^{-3}$. The pyramid size formed after the etch has $W_{base} = 1.6\,\mathrm{\mu m}$ and different NW radii 50 - 100 nm to simulate the random character of real NWAs. The SOD process is simulated by depositing a layer of P dopant with a conc. of $5 \times 10^{21}\,\mathrm{cm}^{-3}$. P drive in is done by annealing at 900 °C for 1 min. The oxide formed is removed by an anisotropic etch. The doping profiles of the various structures are given in Fig. 6.12.

The junction depth is approximately 40 nm, which leaves the NWs with a core-shell structure. The carrier generation profile is solved using Lumerical, and integrated into Synopsys Sentaurus to perform the electrical simulation under illumination. Due to the fabrication process, dangling bonds can exists at the surface, causing interface trap states (IFS) which are implicitly used in the SRH equation (2.8).

In this work, we evaluate the influence of recombination and traps on the electrical performance of the proposed structures. Passivation of nanotextured silicon, via thermally grown oxide, PECVD SiN_x deposition or atomic layer deposition (ALD) of Al_2O_3 is well documented [26,129–133]. Data obtained from these processing steps provide a lower and upper bound for SRV[2] and IFS[3] in these simulations. It is reported that SRV can reach as high as $1 \times 10^{5}\,\mathrm{cm\,s}^{-1}$ in unpassivated surfaces whilst values as low as $10\,\mathrm{cm\,s}^{-1}$ have been achieved with passivation [26,129,131–133]. Furthermore, for SiNWs, trap states of donor type have been identified [134]. These are positively charged when empty and are

[2] Surface recombination velocity
[3] Interface trap state density

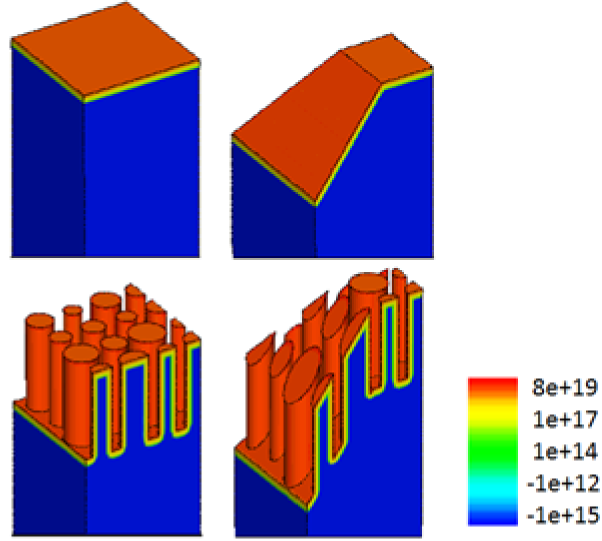

Figure 6.12: Net Active (cm^{-3}) doping profile of the four different structures.

neutral when filled with electrons, with a trapping cross-sectional of $1 \times 10^{-14}\,cm^2$ [134]. The upper and lower bound for the concentration of these traps are $1 \times 10^{11}\,cm^{-2}$ for passivated and $1 \times 10^{13}\,cm^{-2}$ for unpassivated NWs, respectively [130].

The electrical characteristics for the passivated case are given in Fig. 6.13. This shows an increase in J_{sc} with respect to bulk for pyramid, NWA and hybrid structures. Furthermore, the hybrid structure has the highest J_{sc}, whilst the V_{oc} is similar for all. Table 6.1 summarises the photovoltaic parameters for passivated (SRV = $10\,cm\,s^{-1}$, IFS = $1 \times 10^{11}\,cm^{-2}$) and unpassivated (SRV = $1 \times 10^{5}\,cm\,s^{-1}$, IFS = $1 \times 10^{13}\,cm^{-2}$) structures. Minimal change is observed for pyramid and bulk structures, however the NWA structures are influenced by the passivation process. For the passivated case, an efficiency increase of 56 % is observed from bulk to hybrid, whilst 8.5 % increase is observed from NWA to hybrid. There is only a small increase between the pyramid to NWA case. This minimal increase is attributed to a trade off between lower recombination in the pyramid case and higher carrier generation observed in the NWA case.

Figure 6.14 shows J_{sc} for the full range of SRV and IFS concentrations. This shows the significant influence of passivation on J_{sc} in the hybrid structures, with J_{sc} gradually increasing as both IFS and SRV reduce. There is an acceleration in J_{sc} reduction as the SRV increases above $1 \times 10^{4}\,cm\,s^{-1}$ and IFS conc. above $5 \times 10^{11}\,cm^{-2}$.

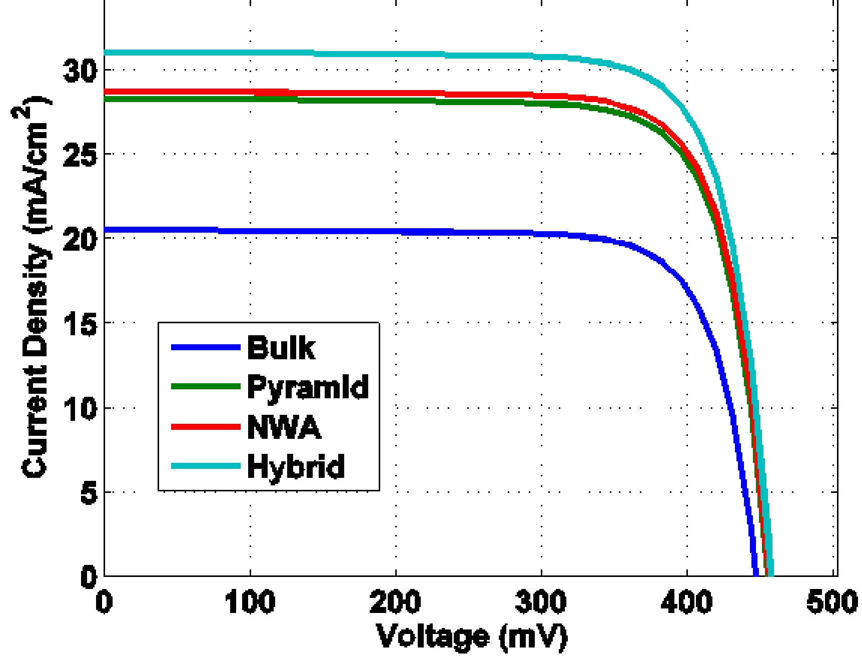

Figure 6.13: Simulated current-voltage characteristics of the various structures under AM1.5 illumination.

Table 6.1: The short-circuit current (J_{sc}), open-cricuit voltage (V_{oc}) and efficiency (η) of various structures, for both passivated (PS) and unpassivated (UPS).

	J_{sc} (mA cm^{-2})		V_{oc} (mV)		η (%)	
	UPS	PS	UPS	PS	UPS	PS
Bulk	20.47	20.50	447.0	447.3	7.12	7.14
Pyramid	28.23	28.27	454.5	455.2	10.03	10.06
NWA	25.12	28.72	450.1	456.4	8.80	10.25
Hybrid	28.00	31.04	452.1	457.5	9.88	11.12

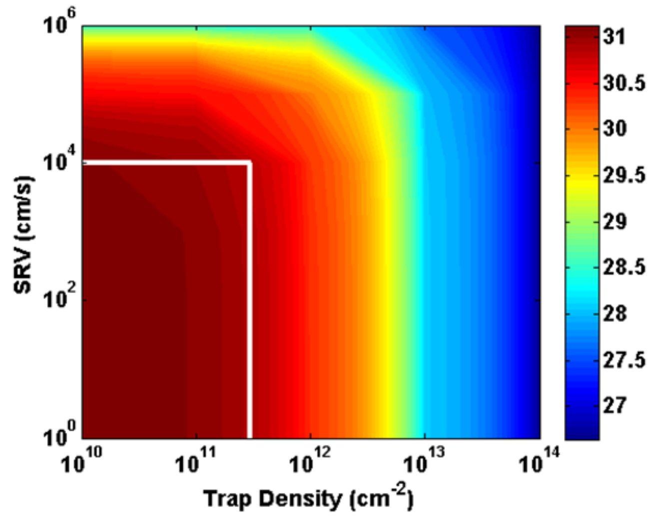

Figure 6.14: Influence of the surface recombination velocity (SRV) and the interface trap state density (IFS) on the short circuit current density $J_{sc}(mA/cm^2)$. The white line represents the threshold below which SRV and IFS are required to observe benefits in hybrid structures.

6.5 Conclusion

In this chapter we discussed the fabrication process, morphology, optical characterisation and electrical modelling of pyramid-NWA structures. The fabrication steps include photo lithography to form a periodic, dense array of oxide masks, followed by alkaline etching for pyramid formation. This is then followed by a single step MACE process to etch NWA on top. The NWs etch perpendicular to the <100> direction. Thus, the pyramidal shape is maintained whereby the hybrid structure is the same size as the pyramid prior to MACE. The NWAs etch with a uniform skyline and are well aligned. However, the length of the NWA on the pyramid array is $\approx 50\%$ shorter than the NWA on the pyramid structures, despite having the same etch time. Furthermore, the valleys in-between the pyramids form porous Si than well defined NWAs. This is due different Ag nucleation dynamics when applying MACE to a dense pyramid array compared to bulk. Optical modelling showed the hybrid structures to have an increased carrier generation rate profile compared to that of bulk, SiNWA and pyramids alone. This is due to the superposition of the lens-effect of the pyramid and the impedance matching by the NWA. Optical measurements agreed with the modelled results, whereby the lowest reflectivity is exhibited by the hybrid structure. Electrical modelling results show that once passivated, a benefit from the addition of

NWAs to Si PV devices is observed. The results of this work is published in [103].

7 Conclusion and Outlook

7.1 Key Findings

This thesis has presented work focused on light trapping structures for use in Si photovoltaics. It has covered opto-electronic modelling, clean-room fabrication and optical characterisation of SiNWA, pyramids and hybrid structures (a combination of both technologies). The key outcomes of the project can be summarised as follows:

Opto-electronic modelling In this work an efficient tool flow is developed in-order to integrate Lumerical, an efficient FDTD optics solver, into TCAD Sentaurus, an industry standard for electrical simulation. When combined, a complete package exists for broadband optoelectronic modelling (ideal for PV). This allows the benefits of material processing chemistry to form structures, followed by accurate and computationally efficient FDTD modelling, and finally electrical characterisation using a comprehensive database of device physics models. In order to integrate the two packages, the ability for Sentaurus to read previously solved optical generation data is manipulated. An electrical solve is undertaken with no illumination, this will output a carrier generation file with zero data. This file is used for two purposes, firstly to form the structure on Lumerical, and secondly to transfer the output data back into Sentaurus. The interface between the two packages is achieved with a combination of tool command language and Matlab script, both of which can be used in open-source platforms.

Light trapping structures In this work we have simulated and measured the optical properties of hybrid micro-nano structures that consists of a dense array of Si pyramids with MACE SiNWAs. The NWA on the pyramids etch perpendicular to the <100>

plane and at 45° to the <111> plane, maintaining a uniform skyline and are well aligned. A reduced etch rate is observed in the hybrid region, due to the geometry limiting the Ag nucleation and thus dendrite formation. The hybrid structures with a pseudo-disordered NWA are modelled using a FDTD method. The results show that the combined pyramid-NWA structures outperform that of NWA and pyramid alone. The disordered NWA shows the lowest reflectivity by accumulating the absorption of the different modes present in a NWA with NWs of varying radius. The hybrid structures also show an increase in carrier generation profile. This is due to the superposition of the lens-effect of the pyramid and the impedance matching via the NWA between free-space and bulk Si. Reflectivity is measured for bulk, NWA, pyramids and the hybrid structures. The results of our simulation agree well with the experimental data whereby the hybrid structures outperform both pyramids and NWA alone, reducing reflectivity below 1% for the case of 1.6 µm pyramid periodicity. Furthermore, reflectivity reduces with increased array density. The photovoltaic parameters of these structures are modelled using a commercial TCAD package. The results show a strong dependency on surface recombination whereby unpassivated structures do not translate an increase in carrier generation to a noticeable increase in efficiency. However, given surface passivation, the hybrid structure shows a significantly improved efficiency of 56% over bulk, 11% over pyramid array and 8.5% over NWA.

These outcomes contribute to the field of PV due to the on-going need for light trapping structures to further improve efficiencies. They can be utilised in not only a core-shell formation but is also relevant to improving back contact silicon solar cells as its core-benefit is focused on front surface optical enhancement. In order to translate the optical benefits to improved efficiency, more work needs to be undertaken in effectively passivated these surfaces. However, given recent advances in passivation techniques (e.g. atomic layer deposition of alumina), the use of the high surface area structures presented in this thesis is an achievable task. The use of more nano-scale light trapping structures requires also the need for better optimization tools in order to model the optical enhancement designs and observe its benefits on devices. As such, the efficient tool flow developed here helps

the integration of different FDTD optical modelling to electrical device modelling.

7.2 Outlook

In order to further the impact of this work, the next step should be to fabricate a working solar cell using the SiNWA and hybrid texturing. Further concepts can be investigated from the results observed in this work, and this is the focus of this section.

7.2.1 Working solar cell

To transfer this anti-reflective technology onto a working solar cell and emulate the modelled results, studies on doping and contact formation on SiNWA and hybrid structures should be performed. Furthermore, to move towards wafer scale devices the approach to form the pyramid array should utilise polymer bead technology rather than expensive reticle masks. An interesting future study would be to show the influence of the pitch, pyramid density (and eventually nanowire size) on the photovoltaic characteristics.

One of the main issues with forming efficient solar cells is ensuring it has good ohmic contacts; otherwise, the structure may create a back to back p-n junction. Initial experiments were undertaken on Al to n-type Si and Cr/Au to p-type Si to establish some preliminary work on device fabrication. The quality of the semiconductor-metal contacts can normally be improved via thermal annealing processes and therefore the quality is investigated under different anneal conditions. Forming gas was used to anneal all samples, and the anneal time was changed between 1 min and 10 min, whilst the anneal temperature was varied between 400°C and 475°C. Each metal is evaporated on to 3 differently doped 2 cm^2 Si pieces. This included low doped, high doped and SOD (P for n-type and B for p-type) samples. The junctions formed for n-type will therefore be Al-nSi-Al; Al-n^+Si-Al; and Al-n^+Si-nSi-n^+Si-Al; likewise for p-type Cr-Au-pSi-Cr-Au, Cr-Au-p^+Si-Cr-Au and Cr-Au-p^+Si-pSi-p^+Si-Cr-Au. The SOD samples were fabricated by first spinning the relevant dopant onto both sides of the respective Si pieces. After which they were placed in a tube furnace for 60 mins at 900°C. After diffusion of the dopants, a HF dip was used to strip the glass layer. The respective metals were then evaporated, 400 nm thickness for Al and 150 nm for Cr-Au. Before the second side is evaporated, a 2 min buffered HF

dip is undertaken to remove the native oxide. The first side is protected by spinning on a layer of photoresist, which is then removed by acetone after the dip. As buffered HF has a controlled rate of etching, the photoresist remains and does not strip off within the dip time. Some of the results from the experiment are shown in Fig. 7.1 and Fig. 7.2. It was found that neither n-type nor p-type form Ohmic contacts without any further treatment.

As expected, by increasing the doping, better contacts are formed. However, the different annealing treatments for the Al-Si samples lead to contact degradation. A possible cause for this is poor purging of the RTA chamber with forming gas, whereby the sample is no longer annealed in an inert atmosphere. Another possibility is that the anneal temperature is too high. Although the eutectic temperature for Al-Si is 577°C, 0.5-1% Al can absorb into Si between 450-500°C. This can lead to spiking behaviour. In future, this experiment should be repeated with lower temperatures, longer purge time and the use of a different inert gas such as Ar should be tested.

The annealing did improve the contacts between Cr-Au and p-type Si - the most favourable condition being 475°C for 1 min. The information gathered from this experiment can be used for future work. The best means to prevent multiple junctions forming when fabricating but still maintain good contacts, would be to first dope a p-type wafer with P. After which Cr-Au should be evaporated and then annealed to form good contacts. Then Al can be evaporated on the diffused n^+ side, which has shown to form good contacts.

The use of a transparent conductive layer is a key part to current PV technologies, as it allows the solar cell to harness all incident light whilst being able to collect carriers with relative efficiency. The use of indium tin oxide (ITO) can be implemented by sputtering onto the structure. Different recipes for sputtering ITO using glass as a substrate are investigated. The varying parameter was the ratio of Ar to O_2 in the plasma. The optical transmission of the samples was compared to the surface conductivity. The results are shown in Fig. 7.3.

From the optics results it can be seen that there is low transmission when no O_2 is supplied. Unsurprisingly this is also the most conductive. This suggests that without any O_2 supply, the ITO granules break but reform on glass as metal rather than metal oxide. By introducing O_2 gas flow we replenish oxygen lost by the ITO granules. The results

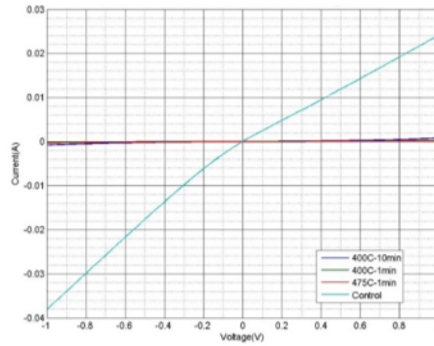

Figure 7.1: IV characteristics of Al contact on n-type Si substrate with varying annealing treatments.

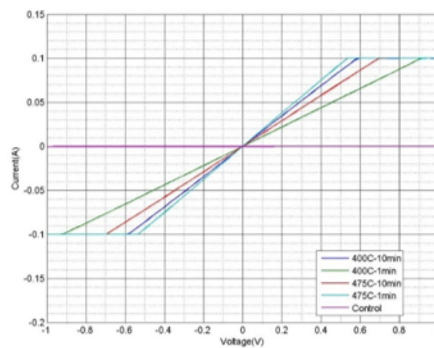

Figure 7.2: IV characteristics of Cu-Au contact on p-type Si substrate with varying annealing treatments

suggest that minimal amount of O_2 gas flow is needed in order to replenish the ITO. The four probe measurements show a large increase in resistivity when the amount of O_2 is increased from 0.5% to 1%. However, there is no benefit observed in the transmission spectrum from this jump. Although 10% O_2 has a relatively high resistivity, it surprisingly showed a lower transmission spectrum than 0.1%-1% of O_2. This suggests that there is a proportional relationship between increasing oxygen flow and resistivity but not with transparency. The transmission result of 0.25%-1% of O_2 seems to show an overlap behaviour and therefore it is difficult to judge which is most transparent. One suggestion for this behaviour is a non-uniform layer of ITO forming on the glass. The non-uniformity arises due to the use of ITO granules as a target. The results show that 0.25 - 0.5% of O_2 will provide the most suitable ITO layer for PV device.

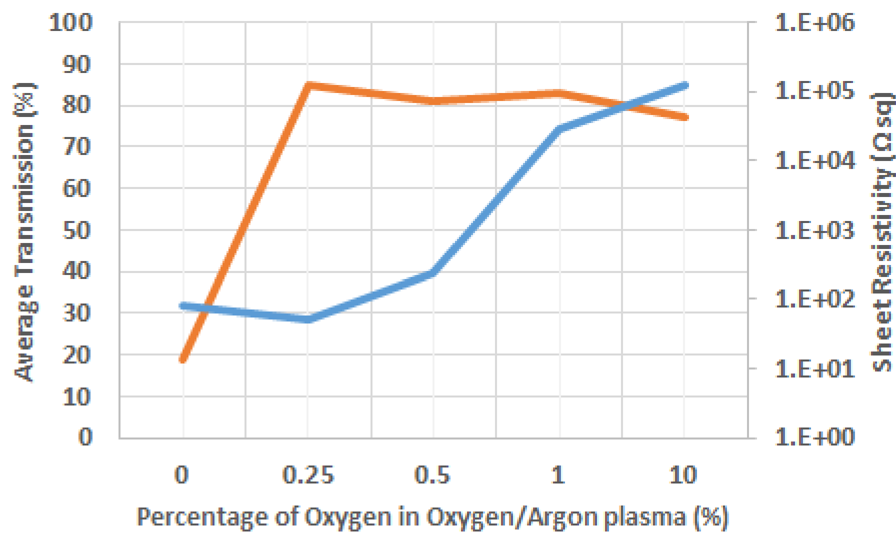

Figure 7.3: This figure illustrates the impact of O_2 composition in an ITO layer on its resistivity (right axis) and transparency (left axis).

7.2.2 NWA transfer

One of the disadvantages of top-down fabrication processes such as MACE, is that the SiNWA is on bulk Si material which can mask the inherent optical and electrical properties of the arrays [135]. By removing this material we can greatly reduce the cost of the final PV device. Organic polymers have been demonstrated to be suitable substrates for transfer of these Si NW arrays [136]. These embedded wires in polymer can be utilised as hybrid solar cells of inoragnic-organic materials. This has the benefit of low-cost fabrication processes compared to commercially available c-Si solar cells, whilst enhancing the performance of the organic solar cells which suffer from the short diffusion length of excitons (about 10nm) and low carrier mobility [137]. In this work we investigate the transfer process of the SiNWA to form the compound material of SiNWA-PDMS. This involves adapting the MACE process to form cracks within the NWA for ease of separation during the transfer.

Poly(dimethylsiloxane), or PDMS, is optically clear and generally considered to be inert, non-flammable and non-toxic [138]. It is widely used for its viscosity properties. It is a suitable substrate for transferring vertical arrays of Si NWs, due to its electrically inert, optically transparent and strong mechanical properties [138]. At low temperatures, the PDMS layer will behave as a film of viscous liquid, allowing Si NWs to be easily embedded within. Once the Si NWs are embedded, the PDMS can be thermally annealed to become

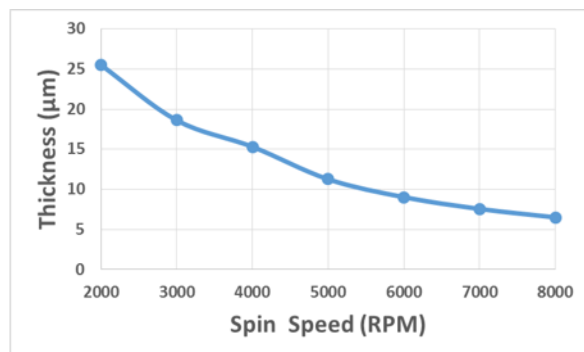

Figure 7.4: PDMS thickness measurements for various spin speeds.

an elastic solid, which holds the array of Si NWs firmly in place while a physical shear force is applied to remove the Si bulk at the cracks of the Si NW array.

The PDMS formula is a mixture of base agent, curing agent and hexane in the proportions of 5:0.5:10 (ml). The base agent contains a proprietary platinum-based catalyst that catalyzes the crosslinking reaction for curing the PDMS [138]. As the ratio of base agent:curing agent is increased, a harder (more cross-linked) PDMS elastomer forms. The hexane acts as a solvent to dissolve the liquid PDMS thereby lowering the viscosity such that uniform spin-coating of thin layers can be achieved. Such a formula results in PDMS films of thickness ranging from 5-25 μm based on different spin speeds, sufficient for the transfer of Si NW arrays - see Fig. 7.4.

The transfer process involves embedding the SiNWAs with cracks into a PDMS layer on glass - see Fig. 7.5. The liquid layer is cured to harden and lock in the SiNWS. A lateral shear force is then provided to separate the Si NWs from the bulk at the cracks. The set-up involved in this process utilises a weighing scale to measure the real-time clamp force. Furthermore a vacuum pump system as illustrated in Fig. 7.5 is used to hold the sample before embedding. The top chuck is designed to be self-levelling such that SiNWs make contact with liquid PDMS vertically. The heating element to cure the liquid PDMS is a peltier device.

In order to form cracks within the SiNWA, such that they can be removed from the substrate with ease, the etch direction must move from vertical to lateral. This occurs through redistribution of AgNPs from the base of the SiNWAs to its side walls. Therefore, once one etch cycle is complete, rather than immersing in nitric acid to remove the AgNPs, the sample is placed in DI water at a temperature of 75°C for several hours. This is known

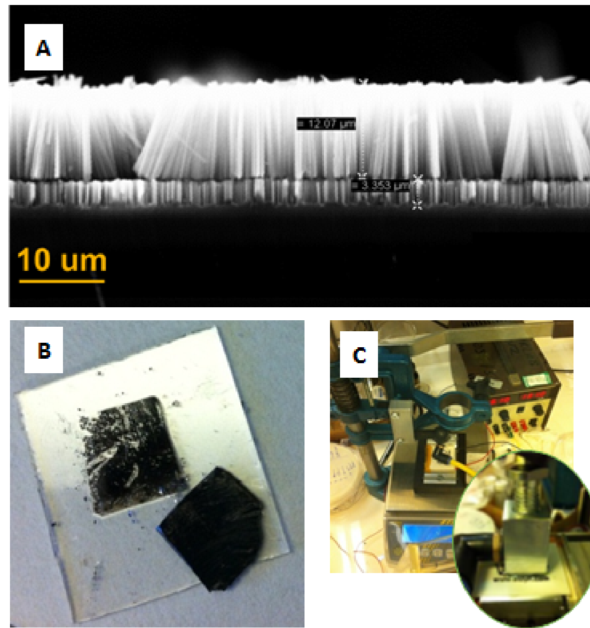

Figure 7.5: a) SEM image of SiNWA with cracks using a two step etching MACE process and a delamination step. b) An image of transferred SiNWA onto a layer of PDMS on glass substrate. c) The mechanical set up used for the transfer process. A Peltier element is used to apply heat for curing the PDMS whilst a self-levelling vacuum chuck is used to transfer the NW substrate. This work was undertaken with Mr Roger Liew and Dr Chuanbo Li.

as delamination [136]. The sample is then placed into a second etch cycle to form the cracks.

7.2.3 Metal-Sulphides

Incorporation of metal sulphide nano-structures (MSN) within a SiNWA modifies the surface properties of SiNWs and can be useful to tune optical properties of the resulting device [139]. Previously, ZnS NPs have been incorporated in Si nano-tips, nano-pillars and nano-wires for various optical applications [139]. Metal sulphide NPs are prepared by a variety of techniques such as sol gel, microwave irradiation, hydrothermal, thermal and chemical deposition [139]. Preliminary work has been undertaken to highlight the potential of PbS NPS. Simulated results in Fig. 7.6 show a clear influence of PbS. A gradual increase in reflectivity is observed as film thickness increases on the bulk. However, when the metal sulphide is in particle form a reduction in reflectivity, proportional to the density of particles, is observed. Furthermore the reduction is more prominent for shorter

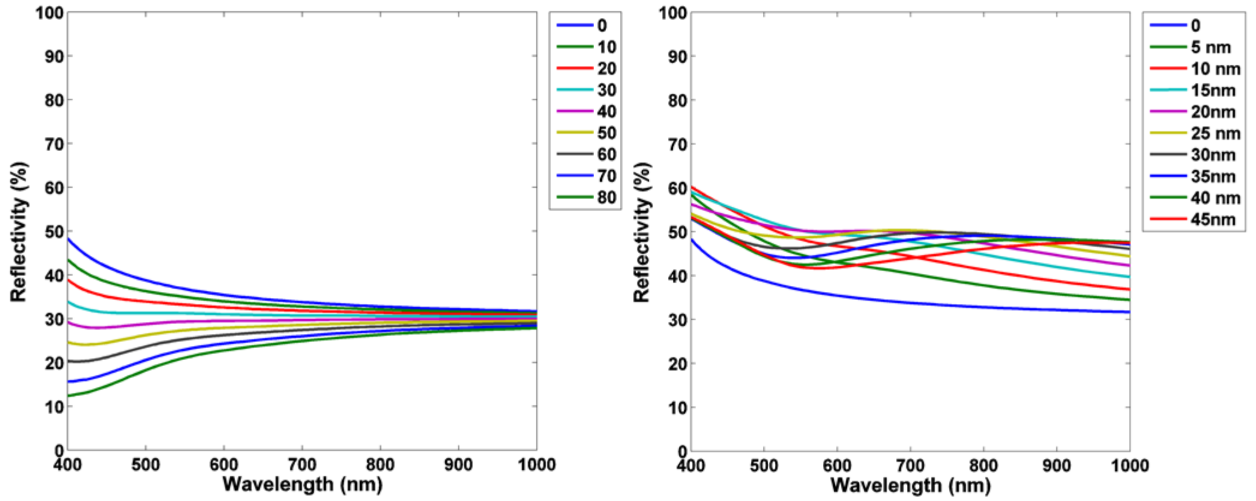

Figure 7.6: Modelled reflection measurements of PbS film (left) and PbS NPs (right) on bulk Si.

wavelengths as compared to that at longer wavelengths.

In the case of a NWA, as seen in the simulations of Fig. 7.7, the deposition of particles along the NWs results in an overall decrease in reflectivity. However, when the MSN are concentrated on the top, an increase in reflectivity is observed. Within these, some overlap occurs due to the variance in position and size of the NWA and MSN, resulting in different modes. This overlap is more prevalent at smaller wavelengths.

Fig. 7.8 shows the simulated power absorption profile of a NWA section at varying wavelengths for different density and position of MSN. In this figure, the power absorption is plotted for NW of 100 nm diameter. From this, a clear influence of MSN is observed. Firstly, there is strong power absorption within MSN for the broad range of wavelengths. In the case when a low density of NPs is distributed along the wire, new modes appear resulting in an increase in power absorption. When the density is increased, the power absorption is high within MSN but a reduction in the bulk and NWA is observed. This reduction is more prominent for shorter wavelengths. Likewise, concentrating the particles at the top of the wires significantly reduces the absorption within NWA and bulk, with a greater prominence for shorter wavelengths.

A cross-section of the fabricated sample whereby PbS NPs are spun into SiNWA is shown in Fig. 7.9. The penetration of larger PbS particles, is observed in the left image, whilst the right image shows the penetration of much smaller particles, sub-30 nm. These images

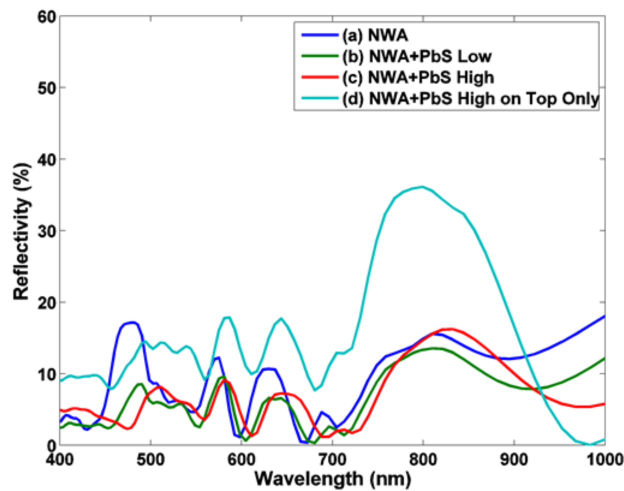

Figure 7.7: Modelled reflection measurements of randomly distributed PbS NPs embedded in SiNWA

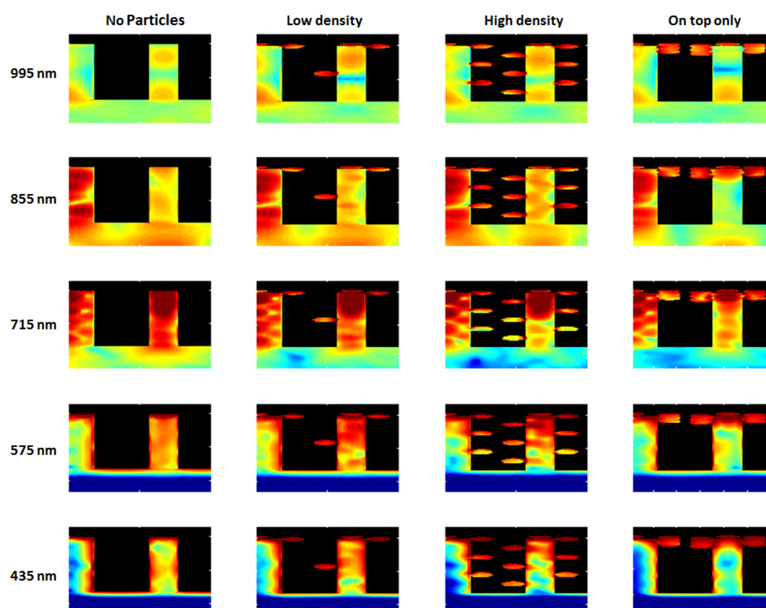

Figure 7.8: Modelled power absorption profile of randomly distributed PbS NPs embedded in SiNWA under varying wavelengths of incident light.

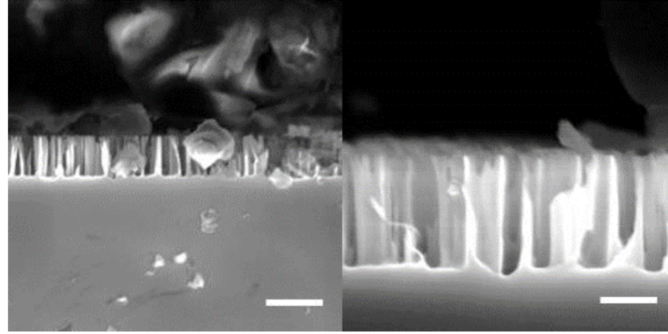

Figure 7.9: SEM image of PbS NPs deposited onto SiNWA. The scale bar is 200 nm.

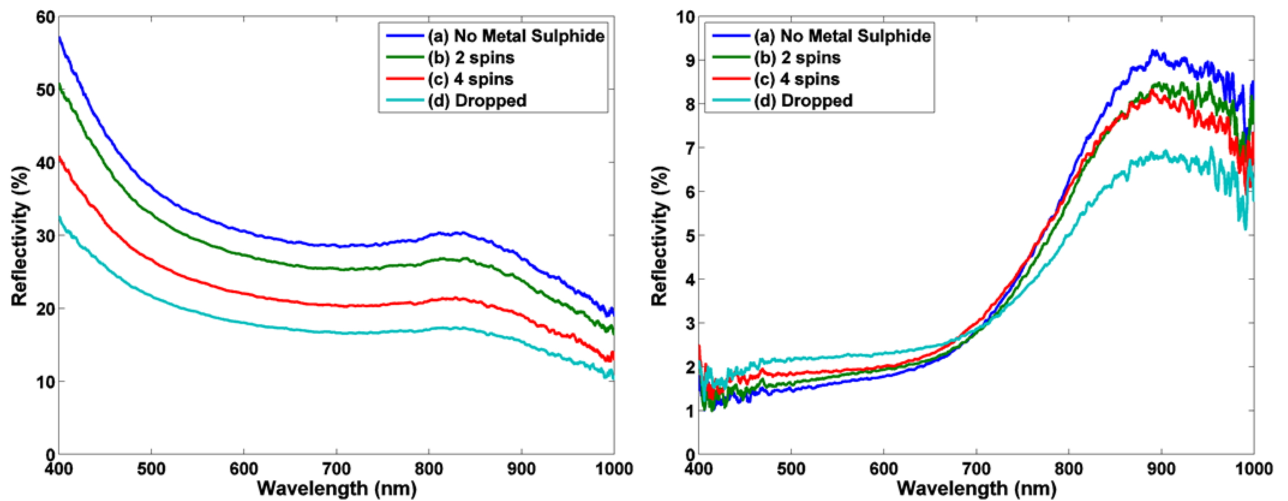

Figure 7.10: Optical measurements of PbS NPs on bulk Si (left) and in SiNWA (right)

were taken off-centre from point of deposition and measurement focus as the concentration is lower and easier to observe. Therefore, the density represented in the measurements is much higher.

Fig. 7.10 shows the optical measurement of PbS NPs deposited on bulk-Si (left) and in a SiNWA (right). For the bulk case it is shown that an increase in density reduces the reflectivity, with a greater influence on shorter wavelengths. For the case of PbS NP in SiNWA, a cross-over is observed, whereby reflectivity increases with density whilst at longer wavelengths, there is a reduction.

7.2.4 Tandem PV with perovskites

Tandem solar cells are hetero-junctions with precisely stacked materials of different bandgap that absorb in different wavelength ranges such that a larger portion of the solar spectrum

can be harnessed. These systems are popular in concentrated PV that uses expensive materials such as III-Vs and Ge. A similar concept can be applied to Si-based PV to increase the percentage of the absorbed spectrum by stacking a perovskite PV on top of a Si cell texturised via the processes established in this work. Perovskites are a novel type of semiconductor which have shown encouraging results for renewable energy applications [140]. This material has shown rapid efficiency, η, improvements in the past two years, with $\eta \approx 20$ in recent reports [141]. The benefits of perovskites are their relatively simple fabrication technique, strong absorption of the solar spectrum, relatively low non-radiative recombination rates, and relatively high carrier mobility. The main drawbacks are the use of lead-based perovskites, degradation by moisture and UV radiation, and hysteresis. Many of these drawbacks are similar to organic PV but intense material research in this field promises development of more stable Pb-free perovskites. What sets perovskites apart from organic PV is that when light is absorbed, free electrons and holes are generated rather than excitons. The generated carriers have a large diffusion length and are extracted using electron and hole transporting layers.

The wafer thickness of most commercial Si PV is in the hundreds of microns. Only half of this is effectively used in the energy conversion process. Therefore, with Si substrates seizing a large fraction of the module price, a thinner wafer constitutes leverage in cost reduction. As such, an assertive plan to decrease wafer thickness to sub-100 μm within the next decade is apparent in industrial road maps [142]. In addition, it has been reported that using sub-100 μm substrates has the advantage of improving open-circuit voltage (Voc) and potentially cell efficiency, see Fig. 7.11.

The enhancement in V_{oc} is attributed to a reduction in the bulk recombination since the thickness falls below the minority-carrier diffusion length (100 μm to 300 μm). However, this gain in Voc from a reduced substrate thickness is counter balanced by a fall in short-circuit current (I_{sc}) due to optical losses in the visible (Vis) and near-infrared (NIR) spectrum. A Si substrate with a thickness greater than 100 μm will absorb most of the spectral range. However, when reducing the thickness below this, significant transmission occurs in the Vis and NIR range, thus causing a drop in the number of photo-generated electron-hole pairs. To tackle this thin Si film problem, the absorption depth can be increased by implementing geometrical light trapping mechanisms, both at the front and

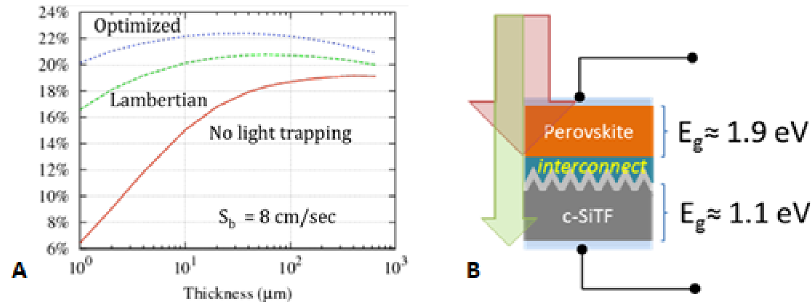

Figure 7.11: a) The modelled efficiency against cell thickness for different light trapping schemes under low surface recombination velocity. This shows that with passivation and very good light trapping, thinner cells can offer a performance advantage [143]. b) The tandem structure of the proposed device.

back surface. In addition to geometrical light trapping enhancements, tandem cells can also increase the absorbed spectrum.

The fabrication and development of a tandem perovskite - Si thin film solar cell can be a high impact implementation of the processes developed in this project. The Si substrate will be thin, crystalline and patterned with hybrid texture to optimise light trapping. It can then be covered with a perovskite film for further optimisation of the absorbed spectral bandwidth. Efficiency boosts over the archetypal solar cell will be offered both by the use of thinner Si films with adequate light trapping and passivation structures and the addition of a perovskite top cell that, due to its bandgap, causes absorption in a larger spectral range. A net cost benefit will result from increased efficiency and thus total module power per area, together with the cost benefit of reduced material required.

Bibliography

[1] IEA Tracking Clean Energy Progress. Energy technology perspectives 2012 excerpt as iea input to the clean energy ministerial. http://www.iea.org/etp/tracking2015/, 2012.

[2] Richard Perez and Marc Perez. A fundamental look at energy reserves for the planet. *The IEA SHC Solar Update*, 50:2–3, 2009.

[3] Department of Energy and Climate Change. Renewable energy statistics. https://www.gov.uk/government/uploads/system/uploads/attachment_data/file/415998/renewables.pdf.

[4] NREL. Research cell efficiency records. http://www.nrel.gov/ncpv/images/efficiency_chart.jpg.

[5] L El Chaar, N El Zein, et al. Review of photovoltaic technologies. *Renewable and Sustainable Energy Reviews*, 15(5):2165–2175, 2011.

[6] Daryl M Chapin, CS Fuller, and GL Pearson. A new silicon p-n junction photocell for converting solar radiation into electrical power. *Journal of Applied Physics*, (25):676–677, 1954.

[7] Georg Pucker, Enrico Serra, and Yoann Jestin. Silicon quantum dots for photovoltaics: A review. 2012.

[8] Brian O'regan and Michael Grätzel. A low-cost, high-efficiency solar cell based on dye-sensitized colloidal tio2 films. *nature*, 353(6346):737–740, 1991.

[9] Vaclav Smil. *General energetics: energy in the biosphere and civilization.* John Wiley & Sons, 1991.

[10] Tony Hayward. Bp statistical review of world energy. *London, England*, 285, 2009.

[11] Max J Riedl. Optical design fundamentals for infrared systems second edition. *Tutorial texts in optical engineering*, 48, 2001.

[12] `http://www.globalwarmingart.com/wiki/File:Solar_Spectrum_png`. Accessed 4 November, 2014.

[13] J Nelson. *The Physics of Solar Cells*. Series on Properties of Semiconductor Materials. Imperial College Press, 2003.

[14] Giancarlo Barbarino, Carlos Maximiliano Mollo, Daniele Vivolo, Gianfranca De Rosa, Riccardo de Asmundis, and Stefano Russo. *Silicon photo multipliers detectors operating in geiger regime: an unlimited device for future applications*. INTECH Open Access Publisher, 2011.

[15] Simon M Sze and Kwok K Ng. *Physics of semiconductor devices*. John Wiley & Sons, 2006.

[16] Fredrik Lindholm, Jerry G Fossum, Edward L Burgess, et al. Application of the superposition principle to solar-cell analysis. *Electron Devices, IEEE Transactions on*, 26(3):165–171, 1979.

[17] Michael Grätzel. Dye-sensitized solar cells. *Journal of Photochemistry and Photobiology C: Photochemistry Reviews*, 4(2):145–153, 2003.

[18] Frank Dimroth, Matthias Grave, Paul Beutel, Ulrich Fiedeler, Christian Karcher, Thomas ND Tibbits, Eduard Oliva, Gerald Siefer, Michael Schachtner, Alexander Wekkeli, et al. Wafer bonded four-junction gainp/gaas//gainasp/gainas concentrator solar cells with 44.7% efficiency. *Progress in Photovoltaics: Research and Applications*, 22(3):277–282, 2014.

[19] Martin A Green, Keith Emery, Yoshihiro Hishikawa, Wilhelm Warta, and Ewan D Dunlop. Solar cell efficiency tables (version 45). *Progress in photovoltaics: research and applications*, 23(1):1–9, 2015.

[20] William Shockley and Hans J Queisser. Detailed balance limit of efficiency of p-n junction solar cells. *Journal of applied physics*, 32(3):510–519, 1961.

[21] Andrew W Blakers, Aihua Wang, Adele M Milne, Jianhua Zhao, and Martin A Green. 22.8% efficient silicon solar cell. *Applied Physics Letters*, 55(13):1363–1365, 1989.

[22] P Papet, O Nichiporuk, A Kaminski, Y Rozier, J Kraiem, J-F Lelievre, A Chaumartin, A Fave, and M Lemiti. Pyramidal texturing of silicon solar cell with tmah chemical anisotropic etching. *Solar Energy Materials and Solar Cells*, 90(15):2319–2328, 2006.

[23] Rahul Dewan, Ivaylo Vasilev, Vladislav Jovanov, and Dietmar Knipp. Optical enhancement and losses of pyramid textured thin-film silicon solar cells. *Journal of Applied Physics*, 110(1):013101, 2011.

[24] Hui Fang, Xudong Li, Shuang Song, Ying Xu, and Jing Zhu. Fabrication of slantingly-aligned silicon nanowire arrays for solar cell applications. *Nanotechnology*, 19(25):255703, 2008.

[25] Fute Zhang, Tao Song, and Baoquan Sun. Conjugated polymer–silicon nanowire array hybrid schottky diode for solar cell application. *Nanotechnology*, 23(19):194006, 2012.

[26] XX Lin, X Hua, ZG Huang, and WZ Shen. Realization of high performance silicon nanowire based solar cells with large size. *Nanotechnology*, 24(23):235402, 2013.

[27] Th Stelzner, M Pietsch, G Andrä, F Falk, E Ose, and S Christiansen. Silicon nanowire-based solar cells. *Nanotechnology*, 19(29):295203, 2008.

[28] Hemant Kumar Raut, V Anand Ganesh, A Sreekumaran Nair, and Seeram Ramakrishna. Anti-reflective coatings: A critical, in-depth review. *Energy & Environmental Science*, 4(10):3779–3804, 2011.

[29] Eugene Hecht and A Zajac. Optics, chapter 9, 2002.

[30] Jianhua Zhao, Martin Green, et al. Optimized antireflection coatings for high-efficiency silicon solar cells. *Electron Devices, IEEE Transactions on*, 38(8):1925–1934, 1991.

[31] PK Singh, R Kumar, M Lal, SN Singh, and BK Das. Effectiveness of anisotropic etching of silicon in aqueous alkaline solutions. *Solar Energy Materials and Solar Cells*, 70(1):103–113, 2001.

[32] Martin A Green. Lambertian light trapping in textured solar cells and light-emitting diodes: analytical solutions. *Progress in Photovoltaics: Research and Applications*, 10(4):235–241, 2002.

[33] Eli Yablonovitch and George D Cody. Intensity enhancement in textured optical sheets for solar cells. *Electron Devices, IEEE Transactions on*, 29(2):300–305, 1982.

[34] Helmuth Horvath. Gustav mie and the scattering and absorption of light by particles: Historic developments and basics. *Journal of Quantitative Spectroscopy and Radiative Transfer*, 110(11):787–799, 2009.

[35] David W Hahn. Light scattering theory. *Department of Mechanical and Aerospace Engineering, Florida*, 2006.

[36] Peter Krogstrup, Henrik Ingerslev Jørgensen, Martin Heiss, Olivier Demichel, Jeppe V Holm, Martin Aagesen, Jesper Nygard, and Anna Fontcuberta i Morral. Single-nanowire solar cells beyond the shockley-queisser limit. *Nature Photonics*, 7(4):306–310, 2013.

[37] Linyou Cao, Justin S White, Joon-Shik Park, Jon A Schuller, Bruce M Clemens, and Mark L Brongersma. Engineering light absorption in semiconductor nanowire devices. *Nature materials*, 8(8):643–647, 2009.

[38] Linyou Cao, Pengyu Fan, Alok P Vasudev, Justin S White, Zongfu Yu, Wenshan Cai, Jon A Schuller, Shanhui Fan, and Mark L Brongersma. Semiconductor nanowire optical antenna solar absorbers. *Nano letters*, 10(2):439–445, 2010.

[39] Bahaa EA Saleh, Malvin Carl Teich, and Bahaa E Saleh. *Fundamentals of photonics*, volume 22. Wiley New York, 1991.

[40] Erik C Garnett, Mark L Brongersma, Yi Cui, and Michael D McGehee. Nanowire solar cells. *Annual Review of Materials Research*, 41:269–295, 2011.

[41] Maoqing Yao, Ningfeng Huang, Sen Cong, Chun-Yung Chi, M Ashkan Seyedi, Yen-Ting Lin, Yu Cao, Michelle L Povinelli, P Daniel Dapkus, and Chongwu Zhou. Gaas nanowire array solar cells with axial p–i–n junctions. *Nano letters*, 14(6):3293–3303, 2014.

[42] Giacomo Mariani, Ping-Show Wong, Aaron M Katzenmeyer, Francois Léonard, Joshua Shapiro, and Diana L Huffaker. Patterned radial gaas nanopillar solar cells. *Nano letters*, 11(6):2490–2494, 2011.

[43] Josef A Czaban, David A Thompson, and Ray R LaPierre. Gaas core- shell nanowires for photovoltaic applications. *Nano letters*, 9(1):148–154, 2008.

[44] Q Gao, L Fu, F Wang, Y Guo, ZY Li, K Peng, Li Li, Z Li, Y Wenas, S Mokkapati, et al. Selective area epitaxial growth of inp nanowire array for solar cell applications. In *Optoelectronic and Microelectronic Materials & Devices (COMMAD), 2014 Conference on*, pages 252–253. IEEE, 2014.

[45] Jesper Wallentin, Nicklas Anttu, Damir Asoli, Maria Huffman, Ingvar Åberg, Martin H Magnusson, Gerald Siefer, Peter Fuss-Kailuweit, Frank Dimroth, Bernd Witzigmann, et al. Inp nanowire array solar cells achieving 13.8% efficiency by exceeding the ray optics limit. *Science*, 339(6123):1057–1060, 2013.

[46] Youngjo Tak, Suk Joon Hong, Jae Sung Lee, and Kijung Yong. Fabrication of zno/cds core/shell nanowire arrays for efficient solar energy conversion. *Journal of Materials Chemistry*, 19(33):5945–5951, 2009.

[47] BL Williams, AA Taylor, BG Mendis, L Phillips, L Bowen, JD Major, and K Durose. Core-shell ito/zno/cds/cdte nanowire solar cells. *Applied Physics Letters*, 104(5):053907, 2014.

[48] Kui-Qing Peng and Shuit-Tong Lee. Silicon nanowires for photovoltaic solar energy conversion. *Advanced Materials*, 23(2):198–215, 2011.

[49] Chito E Kendrick, Heayong P Yoon, Yu A Yuwen, Greg D Barber, Haoting Shen, Thomas E Mallouk, Elizabeth C Dickey, Theresa S Mayer, and Joan M Redwing. Radial junction silicon wire array solar cells fabricated by gold-catalyzed vapor-liquid-solid growth. *Applied Physics Letters*, 97(14):143108, 2010.

[50] Ching-Mei Hsu, Stephen T Connor, Mary X Tang, and Yi Cui. Wafer-scale silicon nanopillars and nanocones by langmuir–blodgett assembly and etching. *Applied Physics Letters*, 93(13):133109, 2008.

[51] Keith J Morton, Gregory Nieberg, Shufeng Bai, and Stephen Y Chou. Wafer-scale patterning of sub-40 nm diameter and high aspect ratio ($> 50:1$) silicon pillar arrays by nanoimprint and etching. *Nanotechnology*, 19(34):345301, 2008.

[52] Yuerui Lu and Amit Lal. High-efficiency ordered silicon nano-conical-frustum array solar cells by self-powered parallel electron lithography. *Nano letters*, 10(11):4651–4656, 2010.

[53] Mengyan Shen, James E Carey, Catherine H Crouch, Maria Kandyla, Howard A Stone, and Eric Mazur. High-density regular arrays of nanometer-scale rods formed on silicon surfaces via femtosecond laser irradiation in water. *Nano letters*, 8(7):2087–2091, 2008.

[54] AY Vorobyev and Chunlei Guo. Direct creation of black silicon using femtosecond laser pulses. *Applied Surface Science*, 257(16):7291–7294, 2011.

[55] Mathieu Halbwax, Thierry Sarnet, Ph Delaporte, Marc Sentis, H Etienne, F Torregrosa, V Vervisch, I Perichaud, and S Martinuzzi. Micro and nano-structuration of silicon by femtosecond laser: application to silicon photovoltaic cells fabrication. *Thin solid films*, 516(20):6791–6795, 2008.

[56] T Sarnet, M Halbwax, R Torres, P Delaporte, M Sentis, S Martinuzzi, V Vervisch, F Torregrosa, H Etienne, L Roux, et al. Femtosecond laser for black silicon and photovoltaic cells. In *Lasers and Applications in Science and Engineering*, pages 688119–688119. International Society for Optics and Photonics, 2008.

[57] Benjamin G Lee, Yu-Ting Lin, Meng-Ju Sher, Eric Mazur, and Howard M Branz. Light trapping for thin silicon solar cells by femtosecond laser texturing. In *Photovoltaic Specialists Conference (PVSC), 2012 38th IEEE*, pages 001606–001608. IEEE, 2012.

[58] X Li and PW Bohn. Metal-assisted chemical etching in hf/h {sub 2} o {sub 2} produces porous silicon. *Applied Physics Letters*, 77(16), 2000.

[59] VA Sivakov, G Bronstrup, B Pecz, A Berger, GZ Radnoczi, M Krause, and SH Christiansen. Realization of vertical and zigzag single crystalline silicon nanowire architectures. *The Journal of Physical Chemistry C*, 114(9):3798–3803, 2010.

[60] Ming-Liang Zhang, Kui-Qing Peng, Xia Fan, Jian-Sheng Jie, Rui-Qin Zhang, Shuit-Tong Lee, and Ning-Bew Wong. Preparation of large-area uniform silicon nanowires arrays through metal-assisted chemical etching. *The Journal of Physical Chemistry C*, 112(12):4444–4450, 2008.

[61] Xing Zhong, Yongquan Qu, Yung-Chen Lin, Lei Liao, and Xiangfeng Duan. Unveiling the formation pathway of single crystalline porous silicon nanowires. *ACS applied materials & interfaces*, 3(2):261–270, 2011.

[62] Yongquan Qu, Lei Liao, Yujing Li, Hua Zhang, Yu Huang, and Xiangfeng Duan. Electrically conductive and optically active porous silicon nanowires. *Nano letters*, 9(12):4539–4543, 2009.

[63] Chuan Bo Li, Kristel Fobelets, and Zahid AK Durrani. Study of two-step electroless etched si nanowire arrays. In *Applied Mechanics and Materials*, volume 110, pages 3284–3288. Trans Tech Publ, 2012.

[64] Jiansheng Jie, Wenjun Zhang, Kuiqing Peng, Guodong Yuan, Chun Sing Lee, and Shuit-Tong Lee. Surface-dominated transport properties of silicon nanowires. *Advanced Functional Materials*, 18(20):3251–3257, 2008.

[65] Gary Goncher, Lori Noice, and Raj Solanki. Bulk heterojunction organic-inorganic photovoltaic cells based on doped silicon nanowires. *Journal of Experimental Nanoscience*, 3(1):77–86, 2008.

[66] Michael D Kelzenberg, Shannon W Boettcher, Jan A Petykiewicz, Daniel B Turner-Evans, Morgan C Putnam, Emily L Warren, Joshua M Spurgeon, Ryan M Briggs, Nathan S Lewis, and Harry A Atwater. Enhanced absorption and carrier collection in si wire arrays for photovoltaic applications. *Nature materials*, 9(3):239–244, 2010.

[67] TL Temple, GDK Mahanama, HS Reehal, and DM Bagnall. Influence of localized surface plasmon excitation in silver nanoparticles on the performance of silicon solar cells. *Solar Energy Materials and Solar Cells*, 93(11):1978–1985, 2009.

[68] S Pillai, KR Catchpole, T Trupke, and MA Green. Surface plasmon enhanced silicon solar cells. *Journal of applied physics*, 101(9):093105, 2007.

[69] Chuan Bo Li, Kristel Fobelets, and Zahid AK Durrani. Study of two-step electroless etched si nanowire arrays. 110:3284–3288, 2012.

[70] Sander A Mann, Mariska J Wild-Scholten, Vasilis M Fthenakis, Wilfried GJHM Sark, and Wim C Sinke. The energy payback time of advanced crystalline silicon pv modules in 2020: a prospective study. *Progress in Photovoltaics: Research and Applications*, 22(11):1180–1194, 2014.

[71] Synopsys. Tcad sentaurus overview. `http://nanolab.gu-unpk.ru/regional/1/TCAD_Overview_March09.pdf`.

[72] Qin Zhang, Wei Zhao, and Alan Seabaugh. Low-subthreshold-swing tunnel transistors. *Electron Device Letters, IEEE*, 27(4):297–300, 2006.

[73] Michele De Marchi, Davide Sacchetto, Stefano Frache, Juyong Zhang, Pierre-Emmanuel Gaillardon, Yusuf Leblebici, and Giovanni De Micheli. Polarity control in double-gate, gate-all-around vertically stacked silicon nanowire fets. In *Electron Devices Meeting (IEDM), 2012 IEEE International*, pages 8–4. IEEE, 2012.

[74] Anne Vandooren, D Leonelli, R Rooyackers, Andriy Hikavyy, Katia Devriendt, Marc Demand, Roger Loo, Guido Groeseneken, and Cedric Huyghebaert. Analysis of trap-assisted tunneling in vertical si homo-junction and sige hetero-junction tunnel-fets. *Solid-State Electronics*, 83:50–55, 2013.

[75] Qin Zhang, Surajit Sutar, Thomas Kosel, and Alan Seabaugh. Fully-depleted ge interband tunnel transistor: Modeling and junction formation. *Solid-State Electronics*, 53(1):30–35, 2009.

[76] Amit Ranjan Trivedi, Sergio Carlo, and Saibal Mukhopadhyay. Exploring tunnel-fet for ultra low power analog applications: a case study on operational transconductance amplifier. In *Proceedings of the 50th Annual Design Automation Conference*, page 109. ACM, 2013.

[77] Martin Hermle, G Letay, SP Philipps, and Andreas W Bett. Numerical simulation of tunnel diodes for multi-junction solar cells. *Progress in Photovoltaics: Research and Applications*, 16(5):409–418, 2008.

[78] Jeffrey F Wheeldon, Christopher E Valdivia, Alexandre W Walker, Gitanjali Kolhatkar, Abdelatif Jaouad, Artur Turala, Bruno Riel, Denis Masson, Norbert Puetz, Simon Fafard, et al. Performance comparison of algaas, gaas and ingap tunnel junctions for concentrated multijunction solar cells. *Progress in Photovoltaics: Research and Applications*, 19(4):442–452, 2011.

[79] Sabina Abdul Hadi, Pouya Hashemi, Ammar Nayfeh, and Judy Hoyt. Thin film a-si/c-si1-xgex/c-si heterojunction solar cells: Design and material quality requirements. *ECS Transactions*, 41(4):3–14, 2011.

[80] Meijun Lu, Ujjwal Das, Stuart Bowden, Steven Hegedus, and Robert Birkmire. Optimization of interdigitated back contact silicon heterojunction solar cells by two-dimensional numerical simulation. In *Photovoltaic Specialists Conference (PVSC), 2009 34th IEEE*, pages 001475–001480. IEEE, 2009.

[81] MD Kelzenberg, MC Putnam, DB Turner-Evans, NS Lewis, and HA Atwater. Predicted efficiency of si wire array solar cells. In *Photovoltaic Specialists Conference (PVSC), 2009 34th IEEE*, pages 001948–001953. IEEE, 2009.

[82] Marc Rüdiger, Christian Schmiga, Michael Rauer, Martin Hermle, and Stefan W Glunz. Optimisation of industrial n-type silicon solar cells with aluminium-alloyed

rear emitter by means of 2d numerical simulation. *Proc. 25th EU PVSEC, Valencia, Spain*, pages 2280–2286, 2010.

[83] Ana Kanevce and Timothy A Gessert. Optimizing cdte solar cell performance: impact of variations in minority-carrier lifetime and carrier density profile. *Photovoltaics, IEEE Journal of*, 1(1):99–103, 2011.

[84] Pietro P Altermatt. Models for numerical device simulations of crystalline silicon solar cellsâĂŤa review. *Journal of computational electronics*, 10(3):314–330, 2011.

[85] Synopsys, Mountain View, CA 94043. *Sentaurus Process User Guide*, j-2014.09 edition, December 2014.

[86] Tasmiat Rahman and Kristel Fobelets. Simulation of rough silicon nanowire array for use in spin-on-doped pn core-shell solar cells. In *Modelling Symposium (EMS), 2013 European*, pages 725–729. IEEE, 2013.

[87] Der-Tsai Lee and Bruce J Schachter. Two algorithms for constructing a delaunay triangulation. *International Journal of Computer & Information Sciences*, 9(3):219–242, 1980.

[88] Justin Lanier. Math munch. `http://mathmunch.org/2013/05/08/circling-squaring-and-triangulating`.

[89] Synopsys, Mountain View, CA 94043. *Sentaurus Device User Guide*, j-2014.09 edition, December 2014.

[90] Zhenhua Li, Jian Wang, Navab Singh, and Sungjoo Lee. Optical and electrical study of core-shell silicon nanowires for solar applications. *Optics express*, 19(105):A1057–A1066, 2011.

[91] Yupeng Xing, Peide Han, Shuai Wang, Yujie Fan, Peng Liang, Zhou Ye, Xinyi Li, Shaoxu Hu, Shishu Lou, Chunhua Zhao, et al. Performance analysis of vertical multi-junction solar cell with front surface diffusion for high concentration. *Solar Energy*, 94:8–18, 2013.

[92] Michael G Deceglie, Vivian E Ferry, A Paul Alivisatos, and Harry A Atwater. Accounting for localized defects in the optoelectronic design of thin-film solar cells. *Photovoltaics, IEEE Journal of*, 3(2):599–604, 2013.

[93] Ningfeng Huang and Michelle L Povinelli. Design of passivation layers on axial junction gaas nanowire solar cells. *Photovoltaics, IEEE Journal of*, 4(6), 2014.

[94] `https://www.lumerical.com/`. Accessed 1 June, 2014.

[95] Ardavan F Oskooi, David Roundy, Mihai Ibanescu, Peter Bermel, JD Joannopoulos, and Steven G Johnson. Meep: A flexible free-software package for electromagnetic simulations by the fdtd method. *Computer Physics Communications*, 181(3):687–702, 2010.

[96] Michael David Kelzenberg. *Silicon microwire photovoltaics, Appendix B*. PhD thesis, California Institute of Technology, 2010.

[97] John B Schneider. Understanding the finite-difference time-domain method. *School of electrical engineering and computer science Washington State University.–URL: http://www. Eecs. Wsu. Edu/˜ schneidj/ufdtd/(request data: 29.11. 2012)*, 2010.

[98] Somada141. Fdtd wiki. `http://fdtd.wikispaces.com/The+Yee+Cell`.

[99] Tasmiat Rahman and Kristel Fobelets. Efficient tool flow for 3d photovoltaic modelling. *Computer Physics Communications*, 2015.

[100] `http://www.synopsys.com/Tools/TCAD/Pages/default.aspx`. Accessed 6 September, 2014.

[101] Synopsys, Mountain View, CA 94043. *Sentaurus Device Electromagnetic Wave Solver User Guide*, j-2014.09 edition, December 2014.

[102] `https://solvnet.synopsys.com/`. Accessed 4 November, 2014.

[103] Tasmiat Rahman, Miguel Navarro-Cía, and Kristel Fobelets. High density micro-pyramids with silicon nanowire array for photovoltaic applications. *Nanotechnology*, 25(48):485202, 2014.

[104] Brendan M Kayes, Harry A Atwater, and Nathan S Lewis. Comparison of the device physics principles of planar and radial pn junction nanorod solar cells. *Journal of applied physics*, 97(11):114302, 2005.

[105] Mahendra K Sunkara, S Sharma, R Miranda, G Lian, and EC Dickey. Bulk synthesis of silicon nanowires using a low-temperature vapor–liquid–solid method. *Applied Physics Letters*, 79(10):1546–1548, 2001.

[106] Yung Hung Jr, San-Liang Lee, Brian J Thibeault, Larry Coldren, et al. Fabrication of highly ordered silicon nanowire arrays with controllable sidewall profiles for achieving low-surface reflection. *Selected Topics in Quantum Electronics, IEEE Journal of*, 17(4):869–877, 2011.

[107] R-Q Zhang, Yeshayahu Lifshitz, and S-T Lee. Oxide-assisted growth of semiconducting nanowires. *Advanced Materials*, 15(7-8):635–640, 2003.

[108] Sanjay K Srivastava, Dinesh Kumar, SW Schmitt, KN Sood, SH Christiansen, and PK Singh. Large area fabrication of vertical silicon nanowire arrays by silver-assisted single-step chemical etching and their formation kinetics. *Nanotechnology*, 25(17):175601, 2014.

[109] Satinder Ahuja and Michael Dong. *Handbook of pharmaceutical analysis by HPLC*, volume 6. Elsevier, 2005.

[110] Constantine A Balanis. *Advanced engineering electromagnetics*, volume 111. Wiley Online Library, 2012.

[111] Alexei Deinega and Sajeev John. Effective optical response of silicon to sunlight in the finite-difference time-domain method. *Optics letters*, 37(1):112–114, 2012.

[112] Björn CP Sturmberg, Kokou B Dossou, Lindsay C Botten, Ara A Asatryan, Christopher G Poulton, C Martijn de Sterke, and Ross C McPhedran. Modal analysis of enhanced absorption in silicon nanowire arrays. *Optics express*, 19(105):A1067–A1081, 2011.

[113] Hadiseh Alaeian, Ashwin C Atre, and Jennifer A Dionne. Optimized light absorption in si wire array solar cells. *Journal of Optics*, 14(2):024006, 2012.

[114] ED Palik, OJ Glembocki, I Heard Jr, PS Burno, and L Tenerz. Etching roughness for (100) silicon surfaces in aqueous koh. *Journal of Applied Physics*, 70(6):3291–3300, 1991.

[115] David L King and M Elaine Buck. Experimental optimization of an anisotropic etching process for random texturization of silicon solar cells. pages 303–308, 1991.

[116] Microchemicals. Wet chemical etching of silicon. `http://www.microchemicals.de/secret/etching.pdf`.

[117] Kazuo Sato, Mitsuhiro Shikida, Yoshihiro Matsushima, Takashi Yamashiro, Kazuo Asaumi, Yasuroh Iriye, and Masaharu Yamamoto. Characterization of orientation-dependent etching properties of single-crystal silicon: effects of koh concentration. *Sensors and Actuators A: Physical*, 64(1):87–93, 1998.

[118] Marc Madou. Fundamentals of microfabrication. 1997. *CRC Press LLC. Capítulo*, 1:1–50, 2003.

[119] Xiaosheng Zhang, Qianli Di, Fuyun Zhu, Guangyi Sun, and Haixia Zhang. Superhydrophobic micro/nano dual-scale structures. *Journal of nanoscience and nanotechnology*, 13(2):1539–1542, 2013.

[120] Hsi-Chien Liu and Gou-Jen Wang. Superior antireflection coating for a silicon cell with a micronanohybrid structure. *International Journal of Photoenergy*, 2014, 2014.

[121] Lining He, Donny Lai, Hao Wang, Changyun Jiang, et al. High-efficiency si/polymer hybrid solar cells based on synergistic surface texturing of si nanowires on pyramids. *Small*, 8(11):1664–1668, 2012.

[122] Hsin-Ping Wang, Tzu-Yin Lin, Chia-Wei Hsu, Meng-Lin Tsai, Chih-Hsiung Huang, Wan-Rou Wei, Ming-Yi Huang, Yi-Jiunn Chien, Po-Chuan Yang, Chee-Wee Liu, et al. Realizing high-efficiency omnidirectional n-type si solar cells via the hierarchical architecture concept with radial junctions. *ACS nano*, 7(10):9325–9335, 2013.

[123] Leland H. Hemming. *Electromagnetic Anechoic Chambers: A Fundamental Design and Specification Guide*. Wiley-IEEE Press, 2003.

[124] Qixun Wee, Jian-Wei Ho, and Soo-Jin Chua. Optimized silicon nanostructures formed by one-step metal-assisted chemical etching of si (111) wafers for gan deposition. *ECS Journal of Solid State Science and Technology*, 3(6):P192–P197, 2014.

[125] Chenxi Lin, Ningfeng Huang, and Michelle L Povinelli. Effect of aperiodicity on the broadband reflection of silicon nanorod structures for photovoltaics. *Optics express*, 20(101):A125–A132, 2012.

[126] Michael D Kelzenberg, Daniel B Turner-Evans, Morgan C Putnam, Shannon W Boettcher, Ryan M Briggs, Jae Yeon Baek, Nathan S Lewis, and Harry A Atwater. High-performance si microwire photovoltaics. *Energy & Environmental Science*, 4(3):866–871, 2011.

[127] Jonathan Grandidier, Michael G Deceglie, Dennis M Callahan, and Harry A Atwater. Simulations of solar cell absorption enhancement using resonant modes of a nanosphere array. *Journal of Photonics for Energy*, 2(1):024502–1, 2012.

[128] Michael G Deceglie, Vivian E Ferry, A Paul Alivisatos, and Harry A Atwater. Design of nanostructured solar cells using coupled optical and electrical modeling. *Nano letters*, 12(6):2894–2900, 2012.

[129] Jihun Oh, Hao-Chih Yuan, and Howard M Branz. An 18.2%-efficient black-silicon solar cell achieved through control of carrier recombination in nanostructures. *Nature nanotechnology*, 7(11):743–748, 2012.

[130] Kang-ill Seo, Shashank Sharma, Amir A Yasseri, Duncan R Stewart, and Theodore I Kamins. Surface charge density of unpassivated and passivated metal-catalyzed silicon nanowires. *Electrochemical and solid-state letters*, 9(3):G69–G72, 2006.

[131] Yaping Dan, Kwanyong Seo, Kuniharu Takei, Jhim H Meza, Ali Javey, and Kenneth B Crozier. Dramatic reduction of surface recombination by in situ surface passivation of silicon nanowires. *Nano letters*, 11(6):2527–2532, 2011.

[132] Zengguang Huang, Sihua Zhong, Xia Hua, Xingxing Lin, Xiangyang Kong, Ning Dai, and Wenzhong Shen. An effective way to simultaneous realization of excellent

optical and electrical performance in large-scale si nano/microstructures. *Progress in Photovoltaics: Research and Applications*, 2014.

[133] Anna Dalmau Mallorquí, Esther Alarcón-Lladó, Ignasi Canales Mundet, Amirreza Kiani, Bénédicte Demaurex, Stefaan De Wolf, Andreas Menzel, Margrit Zacharias, and Anna Fontcuberta i Morral. Field-effect passivation on silicon nanowire solar cells. *Nano Research*, 8(2):673–681, 2015.

[134] K Fobelets, M Meghani, and Cong Li. Influence of minority carrier gas donors on low-frequency noise in silicon nanowires. *Nanotechnology, IEEE Transactions on*, 13(6):1176–1180, 2014.

[135] Jeffrey M Weisse, Dong Rip Kim, Chi Hwan Lee, and Xiaolin Zheng. Vertical transfer of uniform silicon nanowire arrays via crack formation. *Nano letters*, 11(3):1300–1305, 2011.

[136] Chuanbo Li, Kristel Fobelets, Chang Liu, Chunlai Xue, Buwen Cheng, and Qiming Wang. Ag-assisted lateral etching of si nanowires and its application to nanowire transfer. *Applied Physics Letters*, 103(18):183102, 2013.

[137] Lambert Jan Anton Koster et al. *Device physics of donor/acceptor-blend solar cells.* University Library Groningen][Host], 2007.

[138] Alvaro Mata, Aaron J Fleischman, and Shuvo Roy. Characterization of polydimethylsiloxane (pdms) properties for biomedical micro/nanosystems. *Biomedical microdevices*, 7(4):281–293, 2005.

[139] Chen-Ho Lai, Ming-Yen Lu, and Lih-Juann Chen. Metal sulfide nanostructures: synthesis, properties and applications in energy conversion and storage. *Journal of Materials Chemistry*, 22(1):19–30, 2012.

[140] Colin D Bailie, M Greyson Christoforo, Jonathan P Mailoa, Andrea R Bowring, Eva L Unger, William H Nguyen, Julian Burschka, Norman Pellet, Jungwoo Z Lee, Michael Grätzel, et al. Semi-transparent perovskite solar cells for tandems with silicon and cigs. *Energy & Environmental Science*, 8(3):956–963, 2015.

[141] Martin A Green, Anita Ho-Baillie, and Henry J Snaith. The emergence of perovskite solar cells. *Nature Photonics*, 8(7):506–514, 2014.

[142] SEMI Europe. International technology roadmap for photovoltaic results 2013. `http://www.itrpv.net/Reports/Downloads`.

[143] Christopher Petti, Bonna Newman, Robert Brainard, and Jian Li. Optimal thickness for crystalline silicon solar cells. *Twin Creek Technologies, Inc.*

[144] D.K. Schroder. *Semiconductor Material and Device Characterization.* John Wiley, 2nd edition edition, 1998.

8 Appendix 1

8.1 Tools

The main processing tools used thus far include:

Spinner for spinning photoresist and SOD onto various substrates
Evaporator for Evaporating Au/Cr and Al contacts
Sputtering machine for sputtering ITO contacts
Plasma etching for surface cleaning of substrates as well as SiO_2 etch
Wet etching for fabricating SiNWA
Furnace for diffusing SOD and growth of thermal oxide
Rapid thermal anneal for annealing metal contacts
Mask aligner for lithography

Spin coating is the process used for the application of thin films; it consists of depositing drops of the chosen fluid onto the centre of a substrate and then spinning it at high speed. Due to the centripetal acceleration, the deposited fluid will ideally spread to the edges of the substrate before launching off and consequently leaving a thin film on the surface. The thickness and uniformity of the film will depend on the properties of the fluid such as viscosity, surface tension, drying rate etc. and the parameters of the spinner, most notably, speed and acceleration. A spinner offers a thin film coating process that is repeatable, but care should be taken as experiments have shown that small changes in parameters can result in large variation in the coated film.

A common method of depositing a thin metal contact on a substrate is to evaporate the metal source in a vacuum. The vapour particles are able to travel directly to the target substrate due to the vacuum; at which point they return to a solid state, through condensation, on the cooler substrate surface. The vacuum, with pressures of approx. 1×10^{-6} T, provide the vapour atoms with a mean free path equivalent to the dimensions of the vacuum chamber, therefore they are able to travel in a straight line from the source

of evaporation to the target substrate without collision and reaction to the atmosphere. The evaporation of the metal source occurs through resistance heating which, as the name suggests, consists of driving a large current through a filament container with a finite electrical resistance. Although thermal evaporation provides a simple and relatively cheap means to deposit metal contacts with minimal substrate surface damage, it is very wasteful of the metal and can often leave contacts with poor adhesion.

Annealing is a heat treatment of a material causing changes in its properties such as electrical conductivity, strength, hardness, thermal conductivity etc. During the annealing process, the temperature is maintained constant at a suitable level in order establish equilibrium conditions; which is then followed by very slow cooling. One of the common uses of annealing, as used in this project, is for solid state diffusion. This incorporates dopants into the crystal lattice, which can be used to control the electrical properties of the material. Heating the wafer to high temperatures excess of 800°C will cause dopant atoms on the surface to diffuse into the silicon lattice. The diffusion is slow and thus initially most of the atoms will be concentrated at the surface. Increasing the temperature and allowing for long diffusion time will cause increased diffusion into the lattice. Along with slow annealing, which uses tube furnaces, RTA can be achieved by using lamp based heating. In both cases, annealing occurs in the presence of an inert gas; which for this project is Ar.

RIE uses chemically reactive plasma to remove material that has been deposited on the substrate. The plasma is generated within a vacuum (very low pressure) by an electromagnetic field. High energy ions from the plasma attack the substrate. Although the plasma machine can etch silicon, its use in this project is to mainly clean, as it eliminates handling of dangerous acids and solvents. It has also been used to etch SiO_2.

8.2 Surface Profiling

In this project, a scanning electron microscope (SEM) is primarily used to observe the morphology of the SiNWAs. The basic principle of a SEM is to bombard a high energy electron beam onto the sample and detect the secondary electrons that are consequently emitted from the surface. The primary electron beam follows a raster scan pattern, result-

ing in an SEM image formed from the secondary electrons. The primary electron beam is thermionically emitted from an electron gun, which is a tungsten filament cathode. The beam is then focused using condenser lenses and deflected using scatter coils to such that it scans in a raster manner. Although it has many uses, the SEM is most commonly used for visualizing morphology; the strength of this technique laying in its ability to analyse a broad range of scales and also its superior lateral resolution.

8.3 Optics

To make Optical measurements we have made a setup consisting of a spectrometer, light source, collimating lenses, fibre optic cables, a reflection Probe, reflective mirror and various mechanical parts to hold everything in place - see Fig 8.1. The spectrometer is an Ocean Optics USB2000+ VIS-NIR-ES. This works on a 2048 element CCD array detection range of 350 - 1000 nm with an integration time range between 1 ms and 65 s. The spectrometer connects to PC via USB and outputs a spectrum of counts against Wavelength. The sensitivity of the spectrometer means that one count equates to 75 photons. Furthermore, for a 1 s integration time this is estimated by the manufacturer to be 2.9×10^{-17} watts/count. The light source is a HL-2000-FHSA. This has a wavelength range of 360 - 1700 nm and color temperature of 2960K. This comes with a shutter and an attenuator. The first is useful as it allows us to take dark and light measurements with ease, without having to switch the light source off (it usually takes 5 - 10 min to stabilize when switched on). The second is also very useful, as the light intensity has to be changed depending on the sample in place such that we do not saturate the spectrometer. Furthermore, by varying the integration time in the spectrometer we can measure samples which are more sensitive or highly absorbent. Initial measurements have shown that the spectrometer has a thermal noise level of approx 1000 counts.

8.3.1 Relflection

For reflection measurements we make use of the reflection probe. This probe emits light from an outer shell of 6 cores, and collects the reflected light from a larger inner core. At the other end of the probe are two cables, one which connects to the light source and

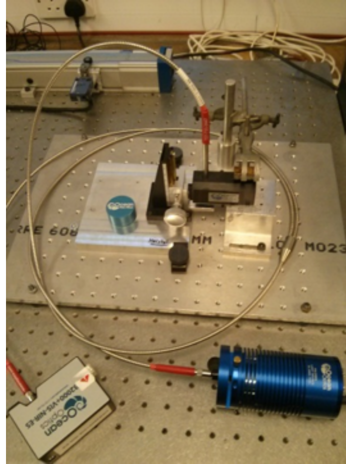

Figure 8.1: An image illustrating the optical setup used to undertake the reflection measurements. The key items are the reflection probe, spectrometer and the halogen light source

the other to the spectrometer. In this case, the light will travel from the light source and be emitted by the outer cores of the probe onto the sample; then the reflected light will be collected by the inner core and which will guide it to the spectrometer. In order to obtain a reference spectrum to normalize our results, we use a high-reflectivity specular reflectance standard. This mirror provides an 85 - 90% reflectance across 250 - 800 nm range, and 85 - 98% reflectance across the 800 - 2500 nm range.

8.3.2 Transmission

For transmission measurements, we connect one fibre optic cable to a spectrometer and another to a light source. The ends of the cables (all SMA connections) are then attached to a collimating lens. These collimating lens are adjoined either side of the transmission stage The sample is placed between the two pillars of this stage such that it sits perpendicular to the collimated beam. The light will therefore travel from the light source and be collimated by the first collimating lens. This beam will then hit the sample, and the transmitted light will fall on the second collimating lens which will direct the light to the spectrometer.

8.4 Current-Voltage Measurments

The current voltage measurements were undertaken using a kiethley sourcemeter interfaced to LabView. Surface conductivity was implemented using a four probe test. This consists

of four probes that are equally spaced, with the outer two probes used to sweep a current, whilst the inner two probes are used to measure the voltage. Each probe has a probe resistance, a probe contact resistance and a spreading resistance. However, the use of a high impedance voltmeter means that these parasitic resistances can be neglected for the two voltage probes. Moreover, the voltage reading from the voltmeter will be approximately equal to the voltage drop across the surface resistance of the sample. The resistivity is given by [144]

$$\rho = \frac{V}{I} \times W \times CF \tag{8.1}$$

where V is the voltage reading from the voltmeter, I is the current carried by the two outer probes, CF is a correction factor and W is the thickness of the material. Assuming that the edges of the sample are far away from the four probes, such that $D \gg S$, where S is the distance between the probes and D is the width of the sample, then [144]

$$CF = \frac{\pi}{\ln 2} \tag{8.2}$$

9 Appendix 2

9.1 Introduction

This appendix provides the full code used to achieve the opto-electronic modelling results of the hybrid structures. It is the supporting material for chapter 3, whereby the interface between Lumerical and Sentaurus is described. It should be noted that Lumerical FDTD and Synopsys TCAD are commercial packages and both require annual licenses. The files presented here have been used on Lumerical FDTD Solutions Version 8.7.3 and TCAD Sentaurus version j-2014.09. A multi-core , high ram workstation is recommended. The scripts provided here were run with the following spec: HP Z820 workstation

- 2 X Intel Xeon E5-2680 2.70Ghz processors
- 128 GB DDR3-1600 RAM.

To test the code run in the following order:

1. Open the workbench for Synopsys Sentaurus.
2. Run 'SProcess file' using the SProcess tool. This will output sprocess.TDR file.
3. Run 'SDevice Dark' file using the SDevice tool. This will output OGO.TDR file.
4. Run 'TDR check' file using the TDX tool. This will output data on the GUI of how many regions and states the structure has. This step is not necessary to test the code for my structure, but it is useful for those who wish to edit the 'TDR to Coordinate List' file for their own structure as they need to be aware of this data. The 'TDR check' is taken from Synopsys so it should be accredited to them [102].
5. Run 'TDR to Coordinate List' file using the TDX tool. This will output OGO_COORDINATES.txt file.

6. Run 'Coordinate List to Binary List' using Matlab. This will output binary.txt file.

7. Open Lumerical. Import the binary.txt file to load the structure. Run an optical simulation. Export the output monitor data to multiple GX.mat files ($X = 1, 2, 3$âĂę).

8. Run 'Map Carrier Generation Data' file to output OGI.txt file.

9. Run 'Carrier Generation Data to TDR' file to output OGI.TDR file.

10. Run 'SDevice Light' file to attain the IV characteristics under light and view the transferred carrier generation data on plot_data.tdr.

9.2 TCAD

9.2.1 SProcess

```
line y loc=0 spa=0.1 tag=left
line y loc=1.6 spa=0.1 tag=right
line x loc=0 spa=0.1 tag=top
line x loc=5 tag=bottom
line z loc=0 spa=0.2 tag=front
line z loc=1.6 spa=0.2 tag=back

#Initialise Silicon structure
math numThreads=Maximum
region Silicon xlo=top xhi=bottom ylo=left yhi=right zlo=front zhi=back
    name=slab
init concentration=1e15 field=Boron wafer.orient=100

#Etch Pyramid
deposit material= {Oxide} type=isotropic time=1.0 rate= {0.2}
diffuse temperature=900<C> time=10.0<min>  O2
mask layoutfile=nwamwa.lyt
mask name=MWA negative
photo mask=MWA thickness=0.5
etch material= {Oxide} type=anisotropic thickness=1
strip Photoresist
etch material=silicon type=crystal crystal_rate= {"<100>" =1 "<110>" =0 "
    <111>" =0} time=1
```

```
22 etch material= {Oxide} type=isotropic thickness=1
23
24 #Etch Nanowires
25 mask layoutfile=nwamwa.lyt
26 mask name=NWACIRCLE negative
27 photo mask=NWACIRCLE thickness=0.1
28 etch material= {Silicon} type=anisotropic thickness=0.5
29 strip Photoresist
30
31 #Apply Mesh algorithm
32 refinebox silicon min = {0 0 0} max = {1.3 0.8 0.8} xrefine = 0.02 \
33 yrefine = 0.02 zrefine = 0.02
34 refinebox interface.mat.pairs= {Silicon Aluminum} min.normal.size= 0.005
    normal.growth.ratio= 2.0
35
36 #Dope structure
37 deposit material = {oxide} type = isotropic thickness=0.1  Phosphorus conc
    =5e21
38 temp_ramp name=tempramp_1 time=5 temp=900
39 diffuse temp_ramp=tempramp_1
40 etch material = {Oxide} type=anisotropic rate = {10.0} time=1.1
41
42 #-Define Contacts
43 contact box  bottom name=bottomcontact Silicon
44 contact box  xlo=-0.1 xhi=-0.1 ylo=0 yhi=0.8 zlo=0.0 zhi=0.8 name=
    topcontact aluminum
45
46 grid remesh
47 struct smesh=sprocess.tdr gas
```

9.2.2 SDevice Dark

```
1 File {
2 * set input files:
3 Grid= "sprocess.tdr"
4 OpticalGenerationOutput = "OGO.tdr"
5 * set output files:
6 Plot= "data_plot.tdr"
7 Current = "IV.plt"
```

```
8  Output = "log_file"
9  Parameter= "@parameter@"
10 }
11
12 *Set data fields to plot
13 Plot {
14 *- Doping Profiles
15         Doping DonorConcentration AcceptorConcentration
16 *- Band structure
17         BandGap BandGapNarrowing ElectronAffinity
18         ConductionBandEnergy ValenceBandEnergy
19         eQuasiFermiEnergy hQuasiFermiEnergy
20 *- Carrier Densities:
21         eDensity hDensity
22         EffectiveIntrinsicDensity IntrinsicDensity
23 *- Fields, Potentials and Charge distributions
24         ElectricField/Vector
25         Potential
26         SpaceCharge
27         }
28
29
30 *Define Electrodes
31 Electrode {
32 { Name="topcontact" Voltage=0.0}
33 { Name="bottomcontact" Voltage=0.0}
34 }
35
36 *Define Physics models
37 Physics {
38   Recombination(   SRH   Auger   Radiative   SurfaceSRH     )
39   Mobility( DopingDependence HighFieldSat Enormal  )
40   EffectiveIntrinsicDensity(  BandGapNarrowing (delAlamo) )
41  } * end physics
42
43
44 *Set Iterative method and power
45 Math{-CheckUndefinedModels}
```

```
46 Math {
47 Number_of_Threads=Maximum
48 ParallelLicense (Abort)
49 StackSize=2000000
50 Method= ILS
51 WallClock
52 CurrentPlot (IntegrationUnit = um)
53 }
54
55 *Apply electrical solve
56 Solve{
57 Poisson
58 }
```

9.2.3 SDevice Light

```
1 File {
2 * input files:
3 Grid= "sprocess.tdr"
4 OpticalGenerationInput = "OGI.tdr"
5 * output files:
6 Plot= "plot_data.tdr"
7 Current = "IV.plt"
8 Output = "log_file"
9 Parameter= "@parameter@"
10 }
11
12 *Set data fields to plot
13 Plot {
14 *- Doping Profiles
15         Doping DonorConcentration AcceptorConcentration
16 *- Band structure
17         BandGap BandGapNarrowing ElectronAffinity
18         ConductionBandEnergy ValenceBandEnergy
19         eQuasiFermiEnergy hQuasiFermiEnergy
20 *- Carrier Densities:
21         eDensity hDensity
22         EffectiveIntrinsicDensity IntrinsicDensity
23 *- Fields, Potentials and Charge distributions
```

```
24          ElectricField/Vector
25          Potential
26          SpaceCharge
27  *- Currents
28          Current/Vector eCurrent/Vector  hCurrent/Vector eDriftVelocity/
               Vector hDriftVelocity/Vector
29          CurrentPotential
30          eMobility hMobility
31  *- Generation/Recombination
32          SRHRecombination AugerRecombination TotalRecombination
               SurfaceRecombination RadiativeRecombination
33          eLifeTime hLifeTime
34  *- Optical Generation
35          ComplexRefractiveIndex QuantumYield
36          OpticalIntensity AbsorbedPhotonDensity OpticalGeneration
37  *- Traps
38          eTrappedCharge hTrappedCharge
39          eInterfaceTrappedCharge hInterfaceTrappedCharge
40          eGapStatesRecombination  hGapStatesRecombination
41          }
42
43
44  CurrentPlot {
45    SRH(Integrate(Semiconductor))
46    Auger(Integrate(Semiconductor))
47  }
48
49  *Define Electrodes
50  Electrode {
51  { Name="topcontact" Voltage=0.0}
52  { Name="bottomcontact" Voltage=0.0}
53  }
54
55  *Define Physics models
56  Physics (MaterialInterface="Silicon/Gas") {
57  Recombination(SurfaceSRH)
58  Traps (
```

```
59                  (hNeutral Uniform Conc= 1e11 EnergyMid= 0 EnergySig= 1
                       FromMidBandgap
60                    eXsection= 1e-14 hXsection= 1e-14)
61          )
62 }
63
64 *Define Physics models
65 Physics {
66   Recombination(   SRH   Auger   Radiative   SurfaceSRH     )
67   Mobility( DopingDependence HighFieldSat Enormal  )
68   EffectiveIntrinsicDensity(  BandGapNarrowing (delAlamo) )
69  Optics (
70     ComplexRefractiveIndex (WavelengthDep(Real Imag))
71     OpticalGeneration (
72       QuantumYield(StepFunction(EffectiveBandgap))
73       ReadFromFile(Datasetname=OpticalGeneration)
74     ) * end OpticalGeneration
75   ) * end optics
76 } * end physics
77
78 *Set Iterative method and power
79 Math{-CheckUndefinedModels}
80 Math {
81 Number_of_Threads=Maximum
82 ParallelLicense (Abort)
83 StackSize=2000000
84 Method= ILS
85 WallClock
86 CurrentPlot (IntegrationUnit = um)
87 }
88
89 *Apply electrical sweep
90 Solve{
91 Poisson
92 Transient (
93 InitialTime=0 FinalTime=0.1
94 InitialStep=0.5 MaxStep=0.5 MinStep=1e-5
95 ) { Coupled {Poisson Electron Hole} }
```

```
96 Quasistationary (
97 InitialStep=0.02 MaxStep =0.02 MinStep = 1e-6
98 Goal{ Name="bottomcontact" voltage = 0.8 }
99 Plot{ Range=(0 1) Intervals=2 }
100 ){ Coupled {Poisson Electron Hole} }
101 }
```

9.3 TCL

9.3.1 TDR check

```
1 #written by Synopsys Inc. and is creditted to them. This code helps
    determine how many geometries and states exist in the structure.
2 set f OGO.tdr
3 puts "file: $f"
4 TdrFileOpen $f
5 # loop through geometries
6 set ng [TdrFileGetNumGeometry $f]
7 puts "#geometries: $ng"
8 for {set ig 0} {$ig < $ng} {incr ig} {
9 set gname [TdrGeometryGetName $f $ig]
10 set ns [TdrGeometryGetNumState $f $ig]
11 set nr [TdrGeometryGetNumRegion $f $ig]
12 puts " geometry $ig: $gname"
13 puts " type : [TdrGeometryGetType $f $ig]"
14 puts " dimension: [TdrGeometryGetDimension $f $ig]"
15 puts " transform: [TdrGeometryGetTransform $f $ig]"
16 puts " shift : [TdrGeometryGetShift $f $ig]"
17 puts " #states : $ns"
18 # loop through states
19 for {set is 0} {$is < $ns} {incr is} {
20 set sname [TdrStateGetName $f $ig $is]
21 puts " state $is: $sname"
22 }
23 puts " #regions: $nr"
24 # loop through regions
25 for {set ir 0} {$ir < $nr} {incr ir} {
26 set rname [TdrRegionGetName $f $ig $ir]
```

```
27 puts " region $ir: $rname"
28 }
29 }
30 TdrFileClose $f
```

9.3.2 TDR to Coordinate List

```
1 # Set input and output files
2 set inp OGO.tdr
3 set outf [open "OGO_COORDINATES.txt" "w"]
4 TdrFileOpen $inp
5
6 set ig 0
7 set is 0
8 set ir 0
9
10 #Specify location in TDR
11         set nd [TdrRegionGetNumDataset $inp 0 $ir $is]
12         #Find coordinate data
13         for {set id 0} {$id < $nd} {incr id} {
14                 #find those that contain 'optical generation' quantities
15                 if {[string match OpticalGeneration [TdrDatasetGetQuantity
                       $inp $ig $ir $is $id]]} {
16                                         #extract x,y and z coordinate
17                                         set coords  [
                                               TdrDataGetAllCoordinates $inp
                                               $ig $ir $is $id]
18
19                 }
20         }
21
22 puts $outf "$coords"
23 TdrFileClose $inp
```

9.3.3 Carrier Generation Data to TDR

```
1 # set input file
2 set FIDr [open OGI.txt "r"]
3 set inp "OGI.tdr"
```

```
4
5 TdrFileOpen $inp
6
7 set ig 0
8 set is 0
9 set ir 0
10 set iv 0
11 while { [gets $FIDr NewLine] > 0 } {
12         #Get number of datasets
13         set nd [TdrRegionGetNumDataset $inp 0 $ir $is]
14         for {set id 0} {$id < $nd} {incr id} {
15                 #find those that contain 'optical generation' quantity
16                 if {[string match OpticalGeneration [TdrDatasetGetQuantity
                       $inp $ig $ir $is $id]]} {
17                         break
18                 }
19         }
20         #overwrite data quantity with Input data
21         set nv [TdrDatasetGetNumValue $inp 0 0 0 1]
22         TdrDataSetComponent $inp $ig $ir $is $id $iv 0 0 $NewLine
23         incr iv
24
25 }
26
27 TdrFileSave $inp
28 TdrFileClose $inp
29 close $FIDr
```

9.4 MATLAB

9.4.1 Coordinate List to Binary List

```
1 %set input data
2 xyz=dlmread('OGO_COORDINATES.txt');
3 g1=(((xyz(:,1))))./1e6;
4 g2=(((xyz(:,2)))))./1e6;
5 g3=xyz(:,3)./1e6;
6
```

```
7  %absorption profiles
8  load('G1.mat'); x1=x;y1=y;z1=z;G1=G;
9  load('G2.mat'); x2=x;y2=y;z2=z;G2=G;
10 load('G3.mat'); x3=x;y3=y;z3=z;G3=G;
11 load('G4.mat'); x4=x;y4=y;z4=z;G4=G;
12 load('G5.mat'); x5=x;y5=y;z5=z;G5=G;
13
14
15 parfor k =1:length(xyz)
16         %limit search space
17     if  g3(k) > -2e-6
18                         if g1(k) <0.4e-6 && g2(k) <0.4e-6
19             G=G1;x=x1;y=y1;z=z1;
20                         elseif g1(k) < 0.4e-6 && g2(k) > 0.4e-6
21             G=G2;x=x2;y=y2;z=z2;
22                         elseif g1(k) > 0.4e-6 && g2(k) > 0.4e-6
23             G=G3;x=x3;y=y3;z=z3;
24                         elseif g1(k)> 0.4e-6 && g2(k) < 0.4e-6
25             G=G4;x=x4;y=y4;z=z4;
26                         end
27     end
28     if  g3(k) < -2e-6
29         G=G5;x=x5;y=y5;z=z5;
30     end
31                 %find minimum distance
32        [mx, idx] = min(abs(x - g1(k)));
33        [my, idy] = min(abs(y - g2(k)));
34        [mz, idz] = min(abs(z - g3(k)));
35
36
37         %Extract absorption data
38        T1=G(idx,idy,idz)
39
40        t=1;
41
42         %if absorption data < 1 increase search space
43                 while T1 < 1
44     idx_min=idx-t; idx_max=idx+t;
```

```
45      idy_min=idy-t; idy_max=idy+t;
46      idz_min=idz-t; idz_max=idz+t;
47      if idx_min < 1
48          idx_min=1;
49      end
50      if idx_max > length(x)
51          idx_max=length(x);
52      end
53      if idy_min < 1
54          idy_min=1;
55      end
56      if idy_max > length(y)
57          idy_max=length(y);
58      end
59      if idz_min < 1
60          idz_min=1;
61      end
62      if idz_max > length(z)
63          idz_max=length(z);
64      end
65      Gt=G(idx_min:idx_max,idy_min:idy_max,idz_min:idz_max);
66          %Extract absorption data
67      T1=max(Gt(:))
68      t=t+1;
69  end
70          T(k)= T1./1e6;
71        end
72
73              %Write absorption data to OGI.TXT file
74  fileID = fopen('OGI.txt','w');
75  fprintf(fileID,'%1.0f\r\n',bin_list);
76  fclose(fileID);
77  dwrite('OGI.TXT',T');
```

9.4.2 Map Carrier Generation Data

```
1  %%
2  %set input data
3  lum_xyz=dlmread('OGO_COORDINATES.txt');
```

```
4
5  %find all unique coordinates
6  ux=unique(lum_xyz(:,1));
7  uy=unique(lum_xyz(:,2));
8  uz=unique(lum_xyz(:,3));
9
10 %define mesh density factor
11 Nx=1;Ny=1;Nz=1;
12
13 %list all possible combinations of x,y,z
14 [I,J,K] = ndgrid(ux(1:Nx:end),uy(1:Ny:end),uz(1:Nz:end));
15 all_xyz = [I(:),J(:),K(:)];
16
17 %create binary list
18 bin_list = ismember(all_xyz, lum_xyz, 'rows');
19
20 fileID = fopen('binary.txt','w');
21 fprintf(fileID,'%1.0f\r\n',bin_list);
22 fclose(fileID);
```